PREDICTING X-RAY SPECTRA FROM GLOBAL 3D GRMHD SIMULATIONS OF ACCRETING BLACK HOLES

by

Brooks E. Kinch

A dissertation submitted to Johns Hopkins University
in conformity with the requirements for the degree of
Doctor of Philosophy

Baltimore, Maryland
August 2019

Abstract

The work which follows focuses mainly on the development and application of a technique to make predictions of the X-ray spectra of accreting black hole systems from numerical simulations thereof. We do this, as much as possible, with a first-principles approach: we combine a global three-dimensional General Relativistic magnetohydrodynamic simulation code, a Monte Carlo geodesic-integrating radiation transport code, a deterministic radiative transfer solution, and a photoionization equilibrium code in order to capture all the relevant physics which are involved in the production and transport of the X-ray photons which make up the observed spectra of accreting black holes. This is a significant improvement over the usual methods by which such spectra are interpreted, and is a means by which to bridge the gap between the theory of black hole accretion flows and their observational study. In later chapters, we describe our efforts to introduce a more realistic, physical approach to coronal cooling, thereby improving the underlying simulations on which our spectral predictions are based. We find that, overall, our method generates spectra which are qualitatively similar to those observed, and—importantly—predicts Fe Kα emission line profiles with comparable strength and shape to real observations of this critical diagnostic feature.

Primary Reader and Advisor: Julian H. Krolik

Additional Readers: Timothy M. Heckman, N. Peter Armitage, Scott C. Noble, & Jeremy D. Schnittman

Acknowledgments

I am particularly grateful to my advisor and close collaborators—Julian Krolik, Jeremy Schnittman, Scott Noble, and Tim Kallman—for answering nigh on endless questions not just about physics and the detailed inner workings of their respective codes, but also on the "softer" but no less important parts of becoming a full-fledged scientist: paper and proposal writing, giving talks, and (of critical importance) finding employment once this is all over.

I have had the great fortune to enjoy the unconditional support of my family (especially my parents, who were surprisingly "on board" with a decade of school), Alice (my stalwart feline companion through countless late night debugging sessions), and my girlfriend/roommate/best-friend Jessica, whose contributions to the actual completion of this work are inestimable.

Finally, my fellow graduate students, who through our common travails have become the dearest friends I expect I will ever have. Anthony, Caroline, Joel, Julian, Kim, Nikhil, and Tanvi—I am truly a better person for our friendship.

Table of Contents

Abstract ii

Acknowledgments iii

List of Figures vii

1 Introduction 1

1.1 Astrophysical Black Holes 2

1.2 Key Results from General Relativity 4

1.3 The Eddington Limit 8

1.4 Classical Accretion Disk Theory 10

1.5 The Magnetorotational Instability 12

1.6 Magnetohydrodynamic Simulations 14

1.7 The State of X-ray Spectra Modeling 15

2 Predicting Fe Kα Emission Line Profiles **22**

2.1 From First Principles to Fe Kα Line Profiles 24

2.1.1 The Disk Structure and the Irradiating Flux 24

2.1.2 The Transfer Solution 30

2.2 Results 36

2.2.1 Fe Kα Emission in the Fluid Rest Frame 36

2.2.2 Fe Kα Line Profiles 41

2.3 Discussion 42

3 **Predicting the Complete X-ray Spectrum** **52**

3.1 Method . . . 54

3.1.1 Simulation Data — HARM3D . . . 55

3.1.2 Coronal Radiation Field — PANDURATA . . . 57

3.1.3 Disk Reprocessing — PTRANSX . . . 59

3.1.3.1 Defining the Problem . . . 59

3.1.3.2 The Transfer Solution . . . 61

3.1.3.3 Equilibrium-Finding Procedure . . . 62

3.1.4 The Reprocessed Spectrum . . . 66

3.1.5 PTRANSX and PANDURATA Communication . . . 70

3.1.6 Numerical Specifics . . . 71

3.2 Results . . . 73

3.2.1 Continuum . . . 73

3.2.2 Fe Kα . . . 77

3.3 Discussion . . . 83

4 **Improved Corona Cooling Function** **89**

4.1 Improving on the Target-Temperature Cooling Function . . . 90

4.2 One vs. Two Temperature Fluid . . . 92

4.3 Method . . . 93

4.3.1 Inverse Compton Power . . . 93

4.3.2 Radiation Energy Density . . . 95

4.3.3 The Compton Temperature . . . 97

4.3.4 The IC Cooling Time . . . 97

4.3.5 A Note on Units and Scaling . . . 99

4.3.6 Uncooled Material . . . 102

4.4 Comparison of Coronal Properties . . . 102

4.4.1 Cooling Rate Comparison . . . 103

4.4.2 T_e Comparison 104
4.5 Discussion 107

5 Spin Survey **112**
5.1 IC Cooling Rate 112
5.2 Post-processing: Continuum 117
5.3 Post-processing: Fe Kα 125
5.4 Discussion 131

6 Ion-Electron Coupling **135**
6.1 Method 136
6.2 Simulation Results 138
6.3 Post-Processing 144
6.4 Discussion 146

7 Conclusion **148**

Curriculum Vitae **151**

List of Figures

1.1 A schematic view of an X-ray binary. 4

1.2 ISCO radius as a function of spin. 6

1.3 Diagram of a Kerr black hole. 8

1.4 Gravitational redshift as a function of radius. 9

1.5 Dissipation as a function of radius. 16

2.1 The $\phi-$averaged gas density. 26

2.2 The $\phi-$averaged electron temperature. 27

2.3 A schematic, cross-sectional view of the black hole environment. 28

2.4 The $\phi-$averaged effective temperature. 29

2.5 The $\phi-$averaged X-ray flux incident upon the upper $\tau = 0.1$ surface. 30

2.6 A sampling of the Fe Kα surface brightness in the fluid rest frame. 37

2.7 The Fe Kα surface brightness in the fluid rest frame for the $\phi = 0$ azimuth. . 38

2.8 Fe Kα surface brightness, averaged. 39

2.9 Fe Kα power as a function of scattering optical depth. 41

2.10 Fe Kα line profile, excluding coronal Compton scattering. 43

2.11 Fe Kα line profile, including coronal Compton scattering. 43

2.12 Fe Kα equivalent widths. 44

2.13 Fe Kα line profile comparisons. 47

3.1 High-level schematic of the procedure. 55

3.2 HARM3D density slice. 58

3.3 PANDURATA electron temperature slice. 60
3.4 Monte Carlo line transfer comparison. 63
3.5 Seed photon flux. 67
3.6 Disk albedo at several radii. 69
3.7 Disk albedo at several accretion rates. 69
3.8 Spectral luminosity at several accretion rates. 75
3.9 Electron temperature distribution in the corona. 76
3.10 Photon indices as a function of observer angle. 77
3.11 Power-law fit to the predicted spectrum. 78
3.12 Fe Kα line profiles. 79
3.13 Fe Kα equivalent widths. 79
3.14 Fe Kα line flux. 80
3.15 Fe Kα surface brightness for several accretion rates. 83

4.1 Cooling rate vs. time, target-temperature and IC corona cooling functions. . 104
4.2 Cooling function comparison. 105
4.3 Cooling rate distributed in polar angle. 105
4.4 Cooling rate distributed in radius. 106
4.5 T_e comparison. 107
4.6 Comparison of T_e distribution in the corona. 108

5.1 Cooling rate vs. time for several spins. 114
5.2 Cooling rate vs. time for several spins, over a longer sample time. 115
5.3 Mass accretion rate measured at $r = 10M$, for two spins. 116
5.4 Cooling rate snapshots for several spins. 118
5.5 Cooling rate distributed in polar angle. 119
5.6 Mass distributed in polar angle. 119
5.7 Cooling rate distributed in radius. 120

5.8 T_e comparison, $a = 0$. 121

5.9 T_e comparison, $a = 0.5$. 121

5.10 T_e comparison, $a = 0.9$. 122

5.11 T_e comparison, $a = 0.99$. 122

5.12 Spectral luminosity for several spins. 124

5.13 Photon index vs. inclination angle, for several spins. 124

5.14 Electron temperature distribution in the corona, for several spins. 125

5.15 Fe Kα line profiles, for several spins. 126

5.16 Power-law fit to the predicted spectrum, for several spins. 127

5.17 Fe Kα equivalent width, for several spins. 128

5.18 Fe Kα radial surface brightness profile, for several spins. 129

5.19 Optical depth to midplane, for several spins. 130

6.1 Cooling rate comparison. 139

6.2 Electron temperature comparison. 139

6.3 Cooling rate distributed in polar angle. 140

6.4 Cooling rate distributed in radius. 140

6.5 Comparison of electron temperature distributions in the corona. 141

6.6 The ϕ-averaged density map. 142

6.7 The ϕ-averaged radiation energy density map. 143

6.8 The ratio of electron to ion temperatures. 143

6.9 T_e comparison. 144

6.10 Spectral luminosity comparison. 145

6.11 Fe Kα line profile comparison. 145

Chapter 1

Introduction

There now exists an abundance of observational data from black hole systems, both from stellar-mass black holes in our own Galaxy and from the supermassive black holes at the hearts of others, gathered from over a dozen space-based telescopes. These data include high-resolution spectra and finely-sampled light curves (brightness as a function of time). The methods for interpreting these data, however, have not evolved at the same pace as the technology to collect it—nor have they kept up with modern techniques for simulating the detailed physics of the black hole environment. Model spectra are computed based on simplified descriptions of the accretion structure; the data are then fit with these spectra to constrain values for the model's parameters. In many key ways, however, the assumptions which motivate these simple models are contradicted by the deeper theoretical understanding we have achieved through simulation.

The work which follows focuses on the prediction of theoretical spectra starting from simulations. In practice, this means solving a complex radiation transport and atomic physics problem: thermal photons originate in a dense accretion disk, but scatter through a diffuse (and very hot) corona; they are absorbed and re-emitted to produce emission line features; and they travel along curved trajectories through the deep gravity well surrounding the black hole. We have approached this problem using a combination of several numerical methods interfaced to come to a self-consistent global solution. In additon, we have developed techniques to improve the physical realism—particularly the treatment of the corona—in these simulations.

In this chapter, we review the strong evidence for the existence of astrophysical black holes, the necessary theoretical elements of General Relativity and accretion disks, the development of accretion flow simulations, and finally the state of the art of black hole X-ray spectra analysis.

In Chapter 2 we detail our first attempt at predicting emission line profiles starting from simulation data. The method is expanded considerably in Chapter 3, which allows us to make physically-underpinned, globally self-consistent predictions for the line and continuum spectra. In Chapter 4 we describe an improved, more realistic gas cooling function in the corona; in Chapter 5 we use this more physical treatment to study the effect of black hole spin on the features of the predicted spectra. Finally, Chapter 6 explores the scenario of loosely coupled ion/electron populations in the coronal plasma, and the effect thereof on our spectral predictions.

1.1 Astrophysical Black Holes

In the 1960s and 70s, black holes rapidly transitioned out of the realm of purely theoretical, curious consequences of General Relativity, and into the domain of observationally-testable astrophysics. Pioneering observations of extrasolar X-ray sources by sounding rocket experiments (Giacconi et al., 1962) and the identification of strongly-redshifted atomic emission liness (in the UV and optical) from the nuclear regions of extragalactic radio sources (Schmidt, 1963) were some of the first clues: these would turn out to be stellar-mass black holes in X-ray binaries (specifically, Cyg X-1) and supermassive black holes at the center of active galactic nuclei (AGN), respectively. By the 1990s, X-ray spectroscopy of AGN Fe Kα emission lines (Tanaka et al., 1995; Nandra et al., 1997) from missions like *ASCA* showed asymmetric redshifting so severe that explanations *other* than emission very close to black holes were implausible. With the recent detection of gravitational waves from merging black holes with *LIGO* (Abbott et al., 2016), and the direct imaging of the silhouette of the supermassive black hole in M87 (Event Horizon Telescope Collaboration et al., 2019), the evidence in support of black holes as real astrophysical objects is overwhelming.

Astrophysical black holes fall into two categories: stellar-mass black holes, the final state of stellar evolution for stars too massive to maintain support against gravitational collapse through electron or neutron degeneracy pressure (white dwarfs and neutron stars, respectively), $M > 2.16 \pm 0.17 M_\odot$ [see Rezzolla, Most, and Weih (2018)—the uncertainty in this limit derives from the significant uncertainty of the equation of state for degenerate neutronic matter]; and supermassive black holes ($M \sim 10^6$–$10^9 M_\odot$), which are believed to reside at the centers of nearly all galaxies (Kormendy and Ho, 2013). With a sufficient source of material—either a close companion star for stellar-mass black holes (forming an X-ray binary, or XRB) or plentiful interstellar gas for a supermassive black hole (forming an AGN)—actively accreting black holes can achieve astounding luminosities across the electromagnetic spectrum. Indeed, the most luminous objects known are AGN; the next-most sustained luminous objects are XRBs. For both mass scales, however, their qualitatively similar spectra are interpreted as having a common physical origin: an optically thick, geometrically thin accretion disk radiates blackbody spectra with a range of temperatures—producing a broad thermal peak; the disk is surrounded by a diffuse, much hotter corona, which radiates a power-law X-ray component at energies above the thermal peak (Liang, 1979; Haardt and Maraschi, 1991). A powerful, collimated outflow, i.e., a jet, is often observed in the radio band for both classes as well (Beall, 2015).

Figure 1.1 shows a schematic view of an X-ray binary system, with the electromagnetic band in which each constituent part radiates labeled. Though much of the underlying physics is essentially unchanged across mass scales (thanks to powerful scaling relationships), in this work we are concerned primarily with the accretion disks and coronae of stellar-mass black holes, and the X-rays they produce.

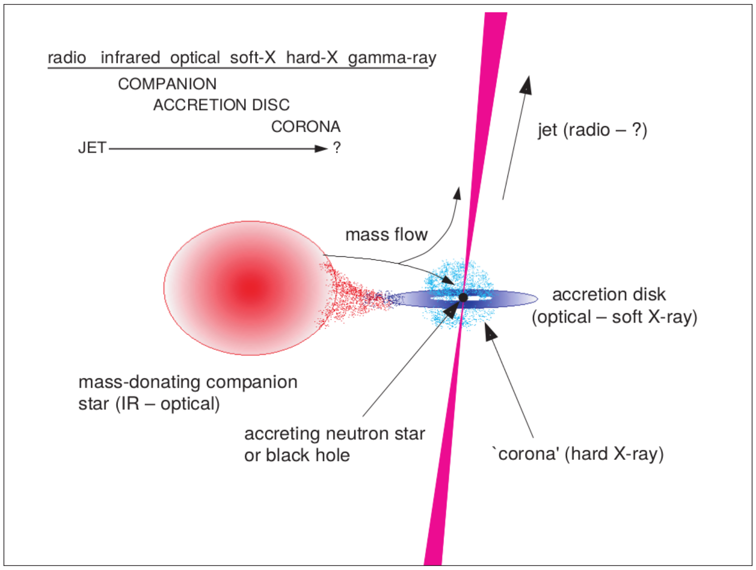

Figure 1.1: From Liedahl and Torres (2005). The anatomy of an X-ray binary system, with its constituent parts, and the electromagnetic band in which they radiate, labeled.

1.2 Key Results from General Relativity

The spacetime in the vicinity of an astrophysical black hole is described by the Kerr metric, the solution to the Einstein field equations in the vacuum outside an uncharged, spherically-symmetric, rotating body [Misner, Thorne, and Wheeler, 1973 is the definitive reference text for General Relativity theory; we (mostly) adopt their notation and sign conventions in this section]. In Boyer-Lindquist coordinates—a generalization of standard spherical coordinates—the Kerr metric line element is

$$\begin{aligned}\left(\frac{ds}{M}\right)^2 = &-\left[1-\frac{2(r/M)}{\Sigma/M^2}\right]\left(\frac{dt}{M}\right)^2 - \frac{4a_*(r/M)\sin^2\theta}{\Sigma/M^2}\left(\frac{dt}{M}\right)d\phi \\ &+\frac{\Sigma/M^2}{\Delta/M^2}\left(\frac{dr}{M}\right)^2 + \frac{\Sigma}{M^2}d\theta^2 + \left[\left(\frac{r}{M}\right)^2 + a_*^2 + \frac{2a_*^2(r/M)\sin^2\theta^2}{\Sigma/M^2}\right]\sin^2\theta d\phi^2.\end{aligned} \tag{1.1}$$

where M is the mass of the black hole (centered on the origin), $a_* = a/M = J/M^2$ is the dimensionless spin parameter, proportional to the angular momentum of the black hole, $\Delta/M^2 = (r/M)^2 - 2(r/M) + a_*^2$, and $\Sigma/M^2 = (r/M)^2 + a_*^2\cos^2\theta$. We use units for which

$G = c = 1$, and we have been careful to arrange equation 1.1 such that the distance and time elements are expressed in ratio to the black hole mass M. From the Kerr metric line element, we see that for a given value of the dimensionless spin parameter a_*, physical distances and times scale only with M; we therefore speak of both distance and time in units of "M", where $1M = r_g = GM/c^2 = (M/M_\odot) \cdot 1.48 \times 10^5$ cm or $1M = t_g = GM/c^3 = (M/M_\odot) \cdot 4.93 \times 10^{-6}$ s.

The location of the event horizon of a Kerr black hole is given by the (outer) solution of $\Delta = 0$: $r_{\mathrm{EH}}/M = 1 + \sqrt{1 - a_*^2}$. For $a = 0$, this reduces to the familiar Schwarzschild radius at $r/M = 2$; for $a_* = 1$, the event horizon retreats to $r/M = 1$. Both strong and weak forms of the cosmic censorship hypothesis—which conjecture that there exist no singularities unshrouded by event horizons (except for the Big Bang)—require $a_* < 1$.

Of particular relevance to the study of accretion flows is the radius of the innermost stable circular orbit (ISCO, referred to occasionally as the radius of marginal stability). In Newtonian gravity, there exists a possible combination of energy and angular momentum to allow for stable, equatorial test particle orbits at any radius; however, no such orbits exist about a Kerr black hole at radii interior to the ISCO. The ISCO radius, in units of M, is a one-to-one function of *only* the dimensionless black hole spin a_*—for orbits in the equatorial plane, it is

$$r_{\mathrm{ISCO}}/M = 3 + Z_2 \mp \sqrt{(3 - Z_1)(3 + z_1 + 2Z_2)}, \tag{1.2}$$

where $-$ is used for prograde test particle orbits, $+$ corresponds to retrograde orbits, and

$$Z_1 = 1 + \left(1 - a_*^2\right)^{1/3} \left[(1 + a_*)^{1/3} + (1 - a_*)^{1/3}\right], \tag{1.3}$$

$$Z_2 = \left(3a_*^2 + Z_1^2\right)^{1/3}. \tag{1.4}$$

The ISCO radius as a function of the dimensionless spin parameter is shown in Figure 1.2: for prograde orbits, the ISCO radius moves inward, from $r/M = 6$ for a non-spinning

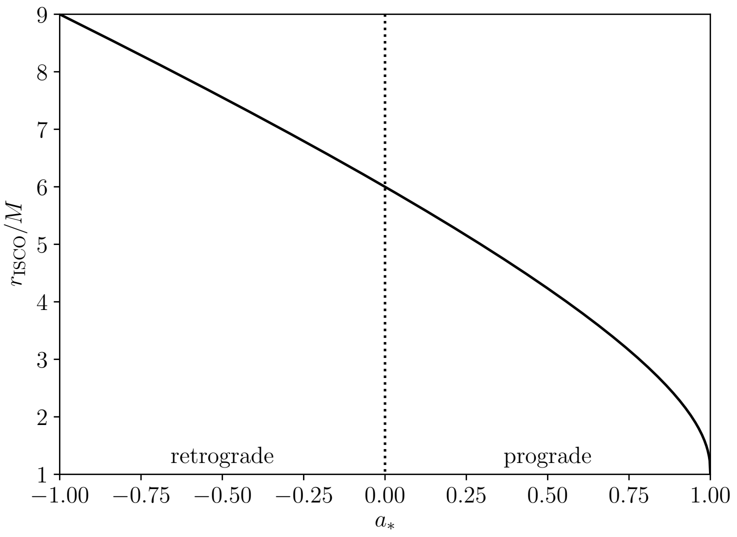

Figure 1.2: The radius (in M) of the ISCO as a function of the black hole spin parameter a_*.

black hole to nearly $r/M = 1$ for a nearly-maximally spinning black hole (coincident with the event horizon in radial *coordinate*, but they remain separate by proper distance—Boyer-Lindquist coordinates suffer from a coordinate singularity at the event horizon, see the factor multiplying the dr^2 term in equation 1.1); for retrograde orbits, the ISCO moves outward, to a maximum at $r/M = 9$. The fact that equation 1.2 is invertible will be of crucial importance in our discussion of spin-measurement techniques below. Because test particle circular orbits become unstable at the ISCO, the region between it and the event horizon is known as the "plunging region"; accreting material is usually assumed to spiral rapidly inwards (i.e., plunge) to the event horizon once it reaches the ISCO. Test particles must, but a magnetized plasma might not (see below).

Unlike the diagonal Schwarzschild metric, the Kerr metric includes an off-diagonal $dtd\phi$ term: the presence of this term coupling time and azimuth is responsible for the "frame-dragging" effect. In short, massive and massless particles alike are "dragged" to rotate in the same sense of the spinning black hole due to the spacetime curvature itself. It is easy to show that particles in the equatorial plane (for example) with *zero* angular momentum as measured by a distant observer (i.e., particles in a zero angular momentum observer, or ZAMO, frame) will rotate (in the same sense as the black hole spin) according to

$$\frac{d\phi}{dt} = \omega_{\rm drag} = \frac{1}{M}\frac{2a_*}{(r/M)\,[(r/M)^2 + a_*^2 + 2a_*^2/(r/M)]}. \tag{1.5}$$

Like all General Relativistic effects, $\omega_{\rm drag}$ increases at smaller radii (and with increasing a_*). Within the "static limit," $r_{\rm stat}/M = 1 + \sqrt{1 - a_*^2 \cos^2\theta}$, matter is *compelled* to rotate in the prograde direction; retrograde motion of any kind (even with, e.g., starship thrusters) is not possible. This region, between the static limit and the event horizon, is known as the ergosphere. Note that with $a = 0$, the static limit coincides with the event horizon, $\omega_{\rm drag}$ vanishes, and the ergosphere disappears. The ergosphere is so named (from the Greek *ergon*, work) because particle orbits within it can have *negative* conserved energy, allowing the spin energy of the black hole to be extracted—the famous Penrose process. The Blandford-Znajek process (Blandford and Znajek, 1977) also extracts spin energy, but the transference mechanism is poloidal magnetic fields from the accreting plasma [also through negative conserved energy (density), in the electromagnetic field]. It is widely believed that spin energy so extracted is the power source of relativistic jets.

The spacetime geometry we have described above is summarized in Figure 1.3, shown in cross section.

One final purely General Relativistic effect we review is gravitational redshift—a reduction in the frequency of a photon emitted near a strong gravitational source as measured by a distant observer. For a photon of frequency ν emitted in a ZAMO frame (and instantaneously at rest with respect to the r and θ coordinates, with ϕ-coordinate velocity $\omega_{\rm drag}$) in the equatorial plane to about a black hole of spin a_* at radius r/M, an observer at infinity measures the photon at frequency ν_∞ according to

$$\nu_\infty = \nu\left[\frac{(r/M)^2 + a_*^2 - 2(r/M)}{(r/M)^2 + a_*^2 + 2a_*^2/(r/M)}\right]^{1/2}. \tag{1.6}$$

Material on circular orbits (with nonzero angular momentum) will have additional frequency

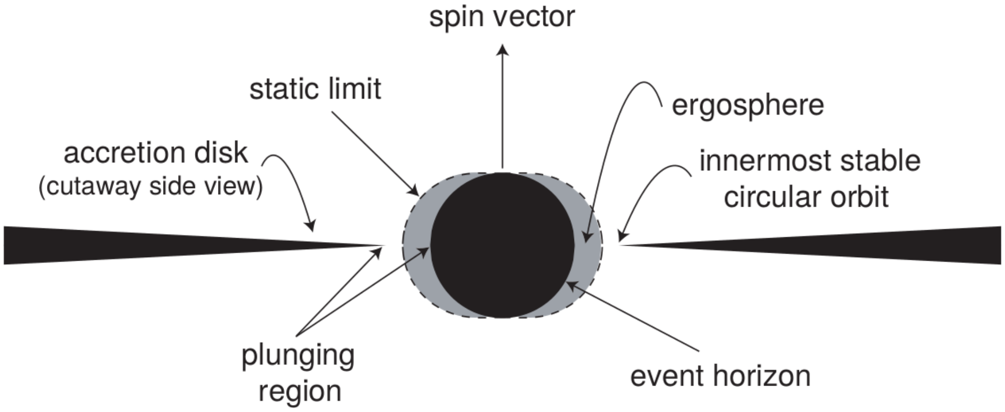

Figure 1.3: From Liedahl and Torres (2005). A cross section view of the geometry of a Kerr black hole.

shifts (red or blue) depending on its velocity relative to the observer. In Figure 1.4, we plot values of the gravitational redshift $z = \nu/\nu_\infty - 1$ as a function of radius r/M for four dimensionless spin values. The degree of redshift for photons emitted very close to the black hole is dramatic. Also plotted in Figure 1.4 are dashed lines indicating the degree of gravitational redshift (calculated in the same way) for photons emitted at the radius of the ISCO. The results we have shown form the logical basis of spin-measuring techniques: the gravitational redshift of line photons is measureable; *if* the emission cuts off at the radius of the ISCO, then a measured redshift can be translated into a measured $r_{\rm ISCO}/M$, which can then be translated into a measured value for the dimensionless spin parameter a_* (though in practice boosting due to orbital material moving at non-negligible fractions of c is taken into account as well, and can be used to constrain inclination). We will return to this key assumption repeatedly throughout the following chapters.

1.3 The Eddington Limit

Before we review the elements of accretion *disk* theory, consider first a spherically-symmetric accretion flow onto a compact object of mass M [so-called Bondi accretion (Bondi, 1952)] which radiates, isotropically, at luminosity L. The gas pressure must be sufficiently low that the only relevant pressure is the *outward* radiation pressure—which acts on electrons, but we

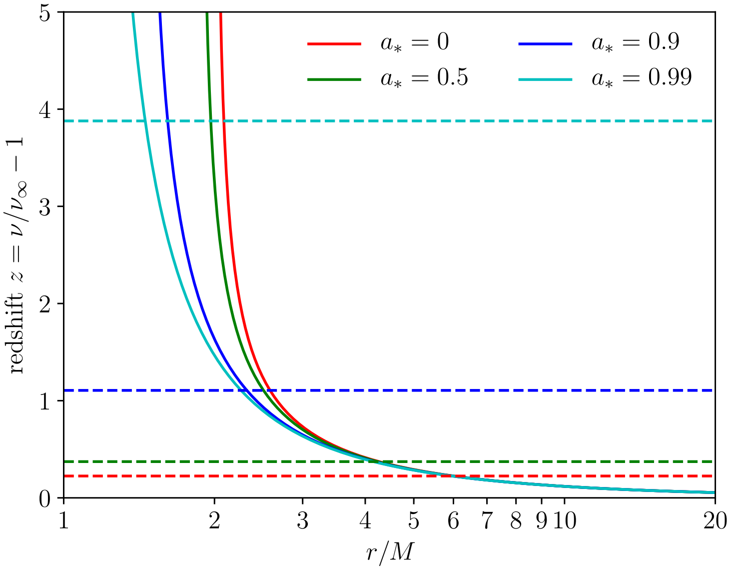

Figure 1.4: The gravitational redshift as a function of radius r/M, for four dimensionless spin values a_*, calculated for an emitter in a ZAMO frame instantaneously at rest with respect to the r and θ coordinates. The dashed lines indicate the value of z for photons emitted at $r_{\rm ISCO}$ for each spin value. The curves approach infinity at the corresponding event horizon radius for each spin.

assume further that the accreting material is totally-ionized hydrogen, so that the electrons "drag" the protons along (through Coulomb attraction). The only relevant *inward* force is gravity. Both the radiative flux and the force due to gravity obey inverse square laws, and so for any mass M there is a luminosity—the Eddington luminosity $L_{\rm Edd}$—beyond which the radiation pressure will overwhelm gravity (at any radius) and suppress accretion. In this highly-idealized scenario,

$$L_{\rm Edd} = \frac{4\pi G M m_p c}{\sigma_T} = 1.26 \times 10^{38} \left(\frac{M}{M_\odot}\right) \text{ erg s}^{-1}. \tag{1.7}$$

In addition, we define the radiative efficiency η such that, if the matter accretes at rate $\dot{M}$ (mass per unit time), the luminosity is given by $L = \eta \dot{M} c^2$. Thus for a given value of η we can define the corresponding Eddington accretion rate,

$$\dot{M}_{\rm Edd} = \frac{L_{\rm Edd}}{\eta c^2} = \frac{4\pi G M m_p}{\eta c \sigma_T} = 2.33 \times 10^{18} \left(\frac{M}{M_\odot}\right) \text{ g s}^{-1}, \tag{1.8}$$

where we have used $\eta = 0.06$ (we discuss choices of η below). While Bondi accretion is unlikely to be an accurate description of the accretion flow geometry for any observationally-relevant black hole, the above two limits are nevertheless useful overall characteristic scales. Because $L_{\rm Edd}$ and $M_{\rm Edd}$ scale linearly with the central black hole mass, we can express the luminosity or accretion rate in a mass-independent fashion (just as we did for distance and time in the previous section), in terms of fractions of $L_{\rm Edd}$ or $\dot{M}_{\rm Edd}$.

1.4 Classical Accretion Disk Theory

Classical, analytic accretion disk theory rests on the following assumptions [for a more detailed treatment, see Krolik (1999b) or Frank, King, and Raine (2002)]:

1. The system is axisymmetric and time-steady.

2. The gas radiates *promptly*—energy dissipated at a point in space is radiated away as photons at the same point in space. This assumption is often referred to as the gas being "radiatively efficient," and it is tantamount to requiring the cooling time to be much shorter than the inflow time. Because radiation is a much more effective means of losing energy than it is of losing angular momentum, efficiently radiating gas will settle on orbits of minimum energy, i.e., circular orbits. It is further assumed that fluid elements are, indeed, on very nearly circular orbits, with only a small inward radial velocity.

3. A conserved radial angular momentum current (which is independent of radius due to the assumption of time-steadiness) must be specified. This is done by specifying a boundary condition. The most popular choice is to set the internal stress to zero at and interior to some inner radius $r_{\rm in}$—and the choice for such a radius is almost always the ISCO.

Simply from conservation laws and these assumptions, it is easy to show that, for a

Newtonian disk, the effective temperature of the disk surface as a function of radius is

$$T_{\rm eff}(r) = \left\{ \frac{3GM\dot{M}}{8\pi\sigma_{\rm SB}r^3} \left[1 - \left(\frac{r_{\rm in}}{r} \right)^{1/2} \right] \right\}^{1/4} . \tag{1.9}$$

The factor in square braces conveys the boundary condition information. For a fixed $\dot{m} = \dot{M}/\dot{M}_{\rm Edd}$, at fixed radius (in units of gravitational radii), the characteristic disk temperature scales weakly with black hole mass: $T \propto M^{-1/4}$. Stellar-mass black hole disks are therefore expected to be hotter than AGN disks—it is for this reason we have first targeted our method to the former, as it is easier to determine a photoionization equilibrium for hotter and thus more strongly ionized gas. Integrating over the whole disk surface, $L_{\rm disk} = GM\dot{M}/2r_{\rm in}$; that is, the accreting material radiates its gravitational binding energy (as measured from the inner disk terminus). From this last expression it is clear that, under the assumptions of classical accretion disk theory, the radiative efficiency η is simply $1/c^2$ times the binding energy per unit mass at the inner boundary of the disk.

Finally, if the disk's vertical structure is in a gas-dominated hydrostatic equilibrium (i.e., the vertical pressure gradient balances the vertical component of gravity), and is sufficiently optically thin that there is not significant vertical temperature variation, it can be shown that the disk aspect ratio, H/r, is on the order of $c_s/v_{\rm orb}$ the ratio of the sound speed ($c_s \sim \sqrt{p/\rho}$) to the local Keplerian orbital velocity ($v_{\rm orb} = \sqrt{GM/r}$). Thus if the disk is geometrically thin, $H/r \ll 1$, the flow is considerably supersonic, $v_{\rm orb} \gg c_s$.

To solve for the detailed structure of the disk, or to calculate time-dependent behavior, however, a fourth assumption is required: the mechanism of angular momentum transport must be specified. The key insight of Shakura and Sunyaev (1973) was to assume—in a bold application of dimensional analysis—that the azimuthally-averaged, vertically- and time-integrated stress is proportional to the similarly averaged and integrated pressure. These so-called α-disk models, after their label for the constant of proportionality, have enjoyed significant, sustained popularity in many applications, including X-ray spectral modeling.

The relativistic generalization of time-steady, classical accretion disk theory was done by

Novikov and Thorne (1973)—they formally identify the inner edge of the accretion disk as the radius of the ISCO, and compute relativistically-corrected values for the classical disk theory radiative efficiency, $\eta_{\rm NT}$, as a function of the dimensionless spin parameter a_*. As spin increases, the ISCO moves closer to the black hole, raising the ISCO-measured binding energy and therefore $\eta_{\rm NT}$—as an example, for spins $a_* = 0$, 0.5, 0.9, and 0.99, $\eta_{\rm NT} = 0.0572$, 0.0821, 0.1558, and 0.2640. The NT radiative efficiency is a useful benchmark to which we refer throughout this work.

1.5 The Magnetorotational Instability

It was recognized fairly early (Pringle, 1981) that common hydrodynamic processes like normal kinematic viscosity are far too inefficient to serve as the mechanisms of angular momentum redistribution in real accretion disks—their observed luminosities, and therefore accretion rates, were simply too large. Observations require $\alpha \sim 1$, and the associated mean free path for such a large kinematic viscosity is on order the disk scale height; if this were the case, the fluid must be so collisionless that it hardly qualifies as a fluid. The actual mechanism—the magnetorotational instability (MRI)—was discovered in the early 1990s (Balbus and Hawley, 1991): it is a powerful and rapidly growing instability, the nonlinear evolution of which results in stirring large amplitude magnetohydrodynamic (MHD) turbulence, which amplifies the magnetic field until $B^2/8\pi \sim 0.01$–0.1 the gas pressure; orbital shear then correlates the B_r and B_ϕ components so that the magnetic stress $B_r B_\phi/4\pi$ is nonzero, and facilitates the outward transport of angular momentum required for accretion. Importantly, the instability conditions are trivially satisfied in an astrophysical accretion disk. These are:

1. The fluid is a nearly perfectly conducting fluid, i.e., the fluid is in the MHD limit. All real accretion disks are sufficiently hot (inferred from their spectra) that the vast majority of their constituent atoms, H and He, will be completely ionized.

2. The fluid undergoes differential rotation such that the orbital velocity decreases with decreasing radius. For Keplerian rotation about a compact object this is indeed the case.
3. There exists some initial—but arbitrarily weak—magnetic field.

The MRI is sufficiently critical to understanding the physics of real accretion disks that it is worth recounting an intuitive explanation (the "spring" analogy). Two elements of a perfectly conducting fluid threaded by a magnetic field line behave as though they are connected by a spring [a consequence of so-called "flux-freezing" in MHD (Alfvén, 1942); for an astrophysically-relevant review of MHD, see Spruit (2013)]: relative displacement between these two fluid elements results in an attractive force between them proportional to the displacement. If the fluid elements are on nearly Keplerian orbits about, say, a black hole—but at slightly different radii—then the inner element will orbit at a slightly faster velocity, but possess less angular momentum; likewise, the outer fluid element will orbit with a slightly slower velocity, but possess greater angular momentum. The differential rotation results in a displacement, and therefore an attractive force between the two elements. The inner element, which is slightly ahead, experiences a force opposite its velocity, and therefore a negative torque. The outer element, which is slightly behind, experiences a force parallel to its velocity, and therefore a positive torque. The net result is an *exchange* of angular momentum from the inner element to the outer element. This is the physical mechanism by which angular momentum is transported *outward* in accretion disks. However, the outer element—having gained angular momentum—moves yet further outward, increasing the displacement, the magnetic tension, and the magnitude of the resulting torques. Thus the magnetorotational *instability.*

The initial numerical studies of the MRI were confined to small patches of disk (Hawley and Balbus, 1991; Hawley, Gammie, and Balbus, 1995; Stone et al., 1996). Nevertheless, these "shearing box" simulations found that the MRI grows rapidly (saturating after only a few tens of orbits), induces large scale turbulence that does not decay with time, is in fact largely independent of seed magnetic field topology or strength, and effectively redistributes angular momentum, leading to estimates of the "effective α" $\sim 10^{-3}$–10^{-2}, nearly sufficient to explain the high accretion rates of observed accretion flows.

1.6 Magnetohydrodynamic Simulations

Global simulations (not limited to a small patch of disk) followed shortly after the initial shearing box studies (Armitage, 1998; Hawley, 2000; Hawley and Krolik, 2001), from which even larger effective α were measured, ~ 0.1, as large-scale fields generated by the extended accretion flow enhance the local angular momentum transport. These simulations, however, were not relativistic. Rather, they were either Newtonian or "pseudo-Newtonian," a scheme in which some of the dynamics near a true Schwarzschild black hole are emulated by choice of a modified potential (Paczyńsky and Wiita, 1980).

Fully General Relativistic MHD (GRMHD) codes were later developed, including HARM (Gammie, McKinney, and Tóth, 2003), of which HARM3D (Noble, Krolik, and Hawley, 2009)—the three-dimensional global GRMHD code we use in this work—is an offshoot. As we discuss in more detail in Chapter 4, the current cutting-edge of modern simulation work is the attempt to incorporate radiative transport into 3D GRMHD codes. Global 3D GRMHD simulations are fabulously costly to perform—they require thousands of CPUs to run for thousands of hours each just to study a small stretch in the evolution of an accretion flow. Codes which incorporate radiation are even more expensive. This is not surprising—after all, these are coupled nonlinear partial differential equations which must be solved in three plus one dimensions (or more with radiative transfer) at sufficient resolution in time and space to resolve even the fastest growing mode of the MRI. It is exactly this expense that motivates the main thrusts of our work—*post*-processing of the simulation data in order to generate spectra, or an approximate calculation of a more realistic corona cooling function—as the considerable additional physics which must be incorporated for these endeavors cannot be fully treated in the course of these simulations—at least not with current (or any reasonable expectation of near future) computing power.

Finally, we briefly discuss two results which are of particular observational significance, and which are representative of the gulf between classical accretion disk theory and simulated MHD accretion flows. 1) The strong magnetic fields generated by the MRI rise above the disk due to magnetic bouyancy (Miller and Stone, 2000); the energy carried by the magnetic field is dissipated in the low density gas at high scale heights, leading to an extremely hot corona. Analytic accretion disk theory makes no prediction of coronae, yet they must exist in order to produce the hard X-ray power-laws observed—however, they appear naturally in MHD simulations. 2) Magnetic fields can effectively transport angular momentum—and therefore allow for dissipation—within the plunging region $r < r_{\rm ISCO}$. This is explored analytically in Krolik (1999a), Gammie (1999), and Agol and Krolik (2000), and shown explicitly in the HARM3D simulations of Noble, Krolik, and Hawley (2009). Figure 1.5 shows the time-averaged HARM3D radiative flux as a function of radius, compared to that predicted by a standard NT disk, and the predictions of Agol and Krolik (2000). In sharp contrast to the assumptions of analytic accretion disk theory, MHD disks appear quite capable of dissipating energy interior to the ISCO.

1.7 The State of X-ray Spectra Modeling

The observation and analysis of X-ray spectra from stellar-mass black holes and AGN is a thriving and vibrant sub-field of astronomy, the analytic workhorse of which is the software package XSPEC (Arnaud, 1996), which facilitates the fitting of sundry model spectra (in arbitrary linear and composite combination) to real X-ray spectral data. All specific models referred to in this section are available in XSPEC.

Typically, black hole spectra are fit with a multicolor blackbody [DISKBB (Mitsuda et al., 1984), i.e., the spectra produced by the temperature profile of 1.9], plus a power-law or (broken power-law) component beyond the thermal peak (typically with an exponential cutoff at very high energies), plus an Fe Kα emission line [e.g., RELLINE (Dauser et al.,

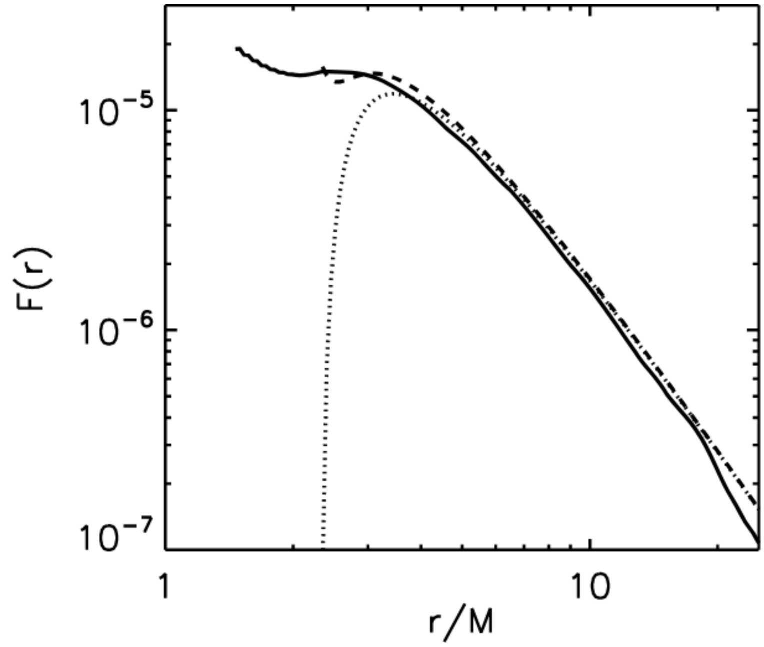

Figure 1.5: From Noble, Krolik, and Hawley (2009). The time-, $\phi-$, and vertically-averaged disk flux as a function of radius from a 3D GRMHD simulation (solid line), compared to a classical NT disk (dotted line) and the predictions of Agol and Krolik (2000) (dashed line).

2013)]. See Reynolds (2013) and Miller and Miller (2015) for recent, comprehensive reviews of these techniques.

The Fe line profile is determined by assuming its emission obeys a radial power-law with an abrupt inner cutoff at the ISCO radius. More sophisticated approaches [e.g., REFLIONX (Ross and Fabian, 2005), XILLVER (García and Kallman, 2010; García, Kallman, and Mushotzky, 2011; García et al., 2013) and RELXILL (García et al., 2014)] compute the reprocessed spectrum by performing radiative transfer and photoionization calculations in semi-infinite plane-parallel slabs of the disk—but these models require assumptions for the spectral shape and strength of the irradiating flux, the density and internal temperature of the disk, how they vary with radius, etc., introducing many free parameters to be constrained by data.

At present *all* methods rely in some way upon a parameterized description of the black hole environment: an idealized corona—often a point source suspended at some supposed height on the z-axis (a "lamppost" model)—emits a power-law spectrum illuminating a semi-infinite disk, with its inner edge precisely at the ISCO. Translating fits using these models into knowledge of the system's underlying *physical* properties depends on the tenuous link between the reality of black hole accretion and the simple model which motivates these assumptions.

Consider the role of the ISCO: as the ISCO radius is a one-to-one function of black hole spin, identifying the inner disk edge as the ISCO allows it to enter as proxy for the spin in model-fitting. Physically, however, the inner disk emission cutoff is *not* a function of the spin alone—it is a complicated function of the disk's surface density and ionization state (Reynolds and Begelman, 1997; Krolik and Hawley, 2002; Beckwith, Hawley, and Krolik, 2008; Kinch et al., 2016; Kinch et al., 2019). Spin-measuring techniques (whether they derive their estimate from the thermal continuum or the Fe line profile) without exception rely on the identification of the ISCO as the inner disk cutoff. Throughout this work, we re-examine the validity of this assumption in the context of our increasingly physical treatments of the accretion flow structure.

More than two dozen stellar-mass and supermassive black hole spins have been reported by multiple groups (Reynolds, 2014), typically using a combination of continuum- and line-fitting techniques. In recent years, the RELXILL models of García et al. (2014) have become the predominant tool used to measure black hole spin. While RELXILL is certainly the most advanced treatment of disk reprocessing readily available to observers, its application tends to infer substantially supersolar (2–10 times) Fe abundances (García et al., 2018)—whether these are physical [which seems unlikely, though physical explanations have been offered (Reynolds et al., 2012)], or an artifact of the model assumptions, is not well understood. In addition, in order to achieve sufficient Fe Kα production, RELXILL must assume disk densities 2–3 orders of magnitude larger than any reasonable disk model suggests. We return to the "supersolar Fe abundance" problem in Chapters 2 and 3, and offer one explanation for how a possible bias could arise from the usual model assumptions.

References

Giacconi, Riccardo, Herbert Gursky, Frank R. Paolini, and Bruno B. Rossi (1962). "Evidence for x Rays From Sources Outside the Solar System". In: *Phys. Rev. Lett.* 9.11, pp. 439–443. DOI: `10.1103/PhysRevLett.9.439`.

Schmidt, M. (1963). "3C 273 : A Star-Like Object with Large Red-Shift". In: *Nature* 197.4872, p. 1040. DOI: `10.1038/1971040a0`.

Tanaka, Y., K. Nandra, A. C. Fabian, H. Inoue, C. Otani, T. Dotani, K. Hayashida, K. Iwasawa, T. Kii, H. Kunieda, F. Makino, and M. Matsuoka (1995). "Gravitationally redshifted emission implying an accretion disk and massive black hole in the active galaxy MCG-6-30-15". In: *Nature* 375, pp. 659–661. DOI: `10.1038/375659a0`.

Nandra, K., I. M. George, R. F. Mushotzky, T. J. Turner, and T. Yaqoob (1997). "ASCA Observations of Seyfert 1 Galaxies. II. Relativistic Iron Kα Emission". In: *ApJ* 477.2, pp. 602–622. DOI: `10.1086/303721`. arXiv: `astro-ph/9606169 [astro-ph]`.

Abbott, B. P. et al. (2016). "Observation of Gravitational Waves from a Binary Black Hole Merger". In: *Phys. Rev. Lett.* 116 (6), p. 061102. DOI: `10.1103/PhysRevLett.116.061102`. URL: `https://link.aps.org/doi/10.1103/PhysRevLett.116.061102`.

Event Horizon Telescope Collaboration, Kazunori Akiyama, Antxon Alberdi, Walter Alef, Keiichi Asada, Rebecca Azulay, Anne-Kathrin Baczko, David Ball, Mislav Baloković, John Barrett, and et al. (2019). "First M87 Event Horizon Telescope Results. I. The Shadow of the Supermassive Black Hole". In: *ApJL* 875.1, L1, p. L1. DOI: `10.3847/2041-8213/ab0ec7`. arXiv: `1906.11238 [astro-ph.GA]`.

Rezzolla, L., E. R. Most, and L. R. Weih (2018). "Using Gravitational-wave Observations and Quasi-universal Relations to Constrain the Maximum Mass of Neutron Stars". In: *ApJL* 852, L25, p. L25. DOI: `10.3847/2041-8213/aaa401`. arXiv: `1711.00314 [astro-ph.HE]`.

Kormendy, J. and L. C. Ho (2013). "Coevolution (Or Not) of Supermassive Black Holes and Host Galaxies". In: *ARA&A* 51, pp. 511–653. DOI: `10.1146/annurev-astro-082708-101811`. arXiv: `1304.7762`.

Liang, E. P. T. (1979). "On the hard X-ray emission mechanism of active galactic nuclei sources". In: *ApJL* 231, pp. L111–L114. DOI: `10.1086/183015`.

Haardt, F. and L. Maraschi (1991). "A two-phase model for the X-ray emission from Seyfert galaxies". In: *ApJL* 380, pp. L51–L54. DOI: `10.1086/186171`.

Beall, J. H. (2015). "A Review of Astrophysical Jets". In: *XI Multifrequency Behaviour of High Energy Cosmic Sources Workshop (MULTIF15)*, p. 58.

Liedahl, D. A. and D. F. Torres (2005). "Atomic X-ray spectroscopy of accreting black holes". In: *Canadian Journal of Physics* 83, pp. 1179–1242. DOI: `10.1139/p05-062`. arXiv: `astro-ph/0510093 [astro-ph]`.

Misner, Charles W., Kip S. Thorne, and John A. Wheeler (1973). *Gravitation.*

Blandford, R. D. and R. L. Znajek (1977). "Electromagnetic extraction of energy from Kerr black holes". In: *MNRAS* 179, pp. 433–456.

Bondi, H. (1952). "On spherically symmetrical accretion". In: *MNRAS* 112, p. 195. DOI: `10.1093/mnras/112.2.195`.

Krolik, Julian H. (1999b). *Active galactic nuclei : from the central black hole to the galactic environment.*

Frank, Juhan, Andrew King, and Derek J. Raine (2002). *Accretion Power in Astrophysics: Third Edition.*

Shakura, N. I. and R. A. Sunyaev (1973). "Black holes in binary systems. Observational appearance." In: *A&A* 24, pp. 337–355.

Novikov, I. D. and K. S. Thorne (1973). "Astrophysics of black holes." In: *Black Holes (Les Astres Occlus).* Ed. by C. Dewitt and B. S. Dewitt, pp. 343–450.

Pringle, J. E. (1981). "Accretion discs in astrophysics". In: *ARA&A* 19, pp. 137–162. DOI: `10.1146/annurev.aa.19.090181.001033`.

Balbus, Steven A. and John F. Hawley (1991). "A Powerful Local Shear Instability in Weakly Magnetized Disks. I. Linear Analysis". In: *ApJ* 376, p. 214. DOI: `10.1086/170270`.

Alfvén, H. (1942). "Existence of Electromagnetic-Hydrodynamic Waves". In: *Nature* 150.3805, pp. 405–406. DOI: `10.1038/150405d0`.

Spruit, H. C. (2013). "Essential Magnetohydrodynamics for Astrophysics". In: *arXiv e-prints*, arXiv:1301.5572, arXiv:1301.5572. arXiv: `1301.5572 [astro-ph.IM]`.

Hawley, John F. and Steven A. Balbus (1991). "A Powerful Local Shear Instability in Weakly Magnetized Disks. II. Nonlinear Evolution". In: *ApJ* 376, p. 223. DOI: `10.1086/170271`.

Hawley, John F., Charles F. Gammie, and Steven A. Balbus (1995). "Local Three-dimensional Magnetohydrodynamic Simulations of Accretion Disks". In: *ApJ* 440, p. 742. DOI: `10.1086/175311`.

Stone, James M., John F. Hawley, Charles F. Gammie, and Steven A. Balbus (1996). "Three-dimensional Magnetohydrodynamical Simulations of Vertically Stratified Accretion Disks". In: *ApJ* 463, p. 656. DOI: `10.1086/177280`.

Armitage, Philip J. (1998). "Turbulence and Angular Momentum Transport in a Global Accretion Disk Simulation". In: *ApJL* 501.2, pp. L189–L192. DOI: `10.1086/311463`. arXiv: `astro-ph/9805133 [astro-ph]`.

Hawley, John F. (2000). "Global Magnetohydrodynamical Simulations of Accretion Tori". In: *ApJ* 528.1, pp. 462–479. DOI: `10.1086/308180`. arXiv: `astro-ph/9907385 [astro-ph]`.

Hawley, John F. and Julian H. Krolik (2001). "Global MHD Simulation of the Inner Accretion Disk in a Pseudo-Newtonian Potential". In: *ApJ* 548.1, pp. 348–367. DOI: `10.1086/318678`. arXiv: `astro-ph/0006456 [astro-ph]`.

Paczyńsky, B. and P. J. Wiita (1980). "Thick accretion disks and supercritical luminosities." In: *A&A* 500, pp. 203–211.

Gammie, Charles F., Jonathan C. McKinney, and Gábor Tóth (2003). “HARM: A Numerical Scheme for General Relativistic Magnetohydrodynamics”. In: *ApJ* 589.1, pp. 444–457. DOI: `10.1086/374594`. arXiv: `astro-ph/0301509 [astro-ph]`.

Noble, S. C., J. H. Krolik, and J. F. Hawley (2009). “Direct Calculation of the Radiative Efficiency of an Accretion Disk Around a Black Hole”. In: *ApJ* 692, pp. 411–421. DOI: `10.1088/0004-637X/692/1/411`. arXiv: `0808.3140`.

Miller, Kristen A. and James M. Stone (2000). “The Formation and Structure of a Strongly Magnetized Corona above a Weakly Magnetized Accretion Disk”. In: *ApJ* 534.1, pp. 398–419. DOI: `10.1086/308736`. arXiv: `astro-ph/9912135 [astro-ph]`.

Krolik, J. H. (1999a). “Magnetized Accretion inside the Marginally Stable Orbit around a Black Hole”. In: *ApJL* 515.2, pp. L73–L76. DOI: `10.1086/311979`. arXiv: `astro-ph/9902267 [astro-ph]`.

Gammie, Charles F. (1999). “Efficiency of Magnetized Thin Accretion Disks in the Kerr Metric”. In: *ApJL* 522.1, pp. L57–L60. DOI: `10.1086/312207`. arXiv: `astro-ph/9906223 [astro-ph]`.

Agol, Eric and Julian H. Krolik (2000). “Magnetic Stress at the Marginally Stable Orbit: Altered Disk Structure, Radiation, and Black Hole Spin Evolution”. In: *ApJ* 528.1, pp. 161–170. DOI: `10.1086/308177`. arXiv: `astro-ph/9908049 [astro-ph]`.

Arnaud, K. A. (1996). “XSPEC: The First Ten Years”. In: *Astronomical Data Analysis Software and Systems V*. Ed. by G. H. Jacoby and J. Barnes. Vol. 101. Astronomical Society of the Pacific Conference Series, p. 17.

Mitsuda, K., H. Inoue, K. Koyama, K. Makishima, M. Matsuoka, Y. Ogawara, K. Suzuki, Y. Tanaka, N. Shibazaki, and T. Hirano (1984). “Energy spectra of low-mass binary X-ray sources observed from TENMA”. In: *PASJ* 36, pp. 741–759.

Dauser, T., J. Garcia, J. Wilms, M. Böck, L. W. Brenneman, M. Falanga, K. Fukumura, and C. S. Reynolds (2013). “Irradiation of an accretion disc by a jet: general properties and implications for spin measurements of black holes”. In: *MNRAS* 430, pp. 1694–1708. DOI: `10.1093/mnras/sts710`. arXiv: `1301.4922 [astro-ph.HE]`.

Reynolds, C. S. (2013). “The spin of supermassive black holes”. In: *Classical and Quantum Gravity* 30.24, 244004, p. 244004. DOI: `10.1088/0264-9381/30/24/244004`. arXiv: `1307.3246 [astro-ph.HE]`.

Miller, M. C. and J. M. Miller (2015). “The masses and spins of neutron stars and stellar-mass black holes”. In: *Phys. Rep.* 548, pp. 1–34. DOI: `10.1016/j.physrep.2014.09.003`. arXiv: `1408.4145 [astro-ph.HE]`.

Ross, R. R. and A. C. Fabian (2005). “A comprehensive range of X-ray ionized-reflection models”. In: *MNRAS* 358, pp. 211–216. DOI: `10.1111/j.1365-2966.2005.08797.x`. eprint: `astro-ph/0501116`.

García, J. and T. R. Kallman (2010). “X-ray Reflected Spectra from Accretion Disk Models. I. Constant Density Atmospheres”. In: *ApJ* 718, pp. 695–706. DOI: `10.1088/0004-637X/718/2/695`. arXiv: `1006.0485 [astro-ph.HE]`.

García, J., T. R. Kallman, and R. F. Mushotzky (2011). "X-ray Reflected Spectra from Accretion Disk Models. II. Diagnostic Tools for X-ray Observations". In: *ApJ* 731, 131, p. 131. DOI: `10.1088/0004-637X/731/2/131`. arXiv: `1101.1115 [astro-ph.HE]`.

García, J., T. Dauser, C. S. Reynolds, T. R. Kallman, J. E. McClintock, J. Wilms, and W. Eikmann (2013). "X-Ray Reflected Spectra from Accretion Disk Models. III. A Complete Grid of Ionized Reflection Calculations". In: *ApJ* 768, 146, p. 146. DOI: `10.1088/0004-637X/768/2/146`. arXiv: `1303.2112 [astro-ph.HE]`.

García, J., T. Dauser, A. Lohfink, T. R. Kallman, J. F. Steiner, J. E. McClintock, L. Brenneman, J. Wilms, W. Eikmann, C. S. Reynolds, and F. Tombesi (2014). "Improved Reflection Models of Black Hole Accretion Disks: Treating the Angular Distribution of X-Rays". In: *ApJ* 782, 76, p. 76. DOI: `10.1088/0004-637X/782/2/76`. arXiv: `1312.3231 [astro-ph.HE]`.

Reynolds, C. S. and M. C. Begelman (1997). "Iron Fluorescence from within the Innermost Stable Orbit of Black Hole Accretion Disks". In: *ApJ* 488, pp. 109–118. eprint: `astro-ph/9705136`.

Krolik, J. H. and J. F. Hawley (2002). "Where Is the Inner Edge of an Accretion Disk around a Black Hole?" In: *ApJ* 573, pp. 754–763. DOI: `10.1086/340760`. eprint: `astro-ph/0203289`.

Beckwith, K., J. F. Hawley, and J. H. Krolik (2008). "Where is the radiation edge in magnetized black hole accretion discs?" In: *MNRAS* 390, pp. 21–38. DOI: `10.1111/j.1365-2966.2008.13710.x`. arXiv: `0801.2974`.

Kinch, B. E., J. D. Schnittman, T. R. Kallman, and J. H. Krolik (2016). "Fe Kα Profiles from Simulations of Accreting Black Holes". In: *ApJ* 826, 52, p. 52. DOI: `10.3847/0004-637X/826/1/52`. arXiv: `1604.01126 [astro-ph.HE]`.

Kinch, Brooks E., Jeremy D. Schnittman, Timothy R. Kallman, and Julian H. Krolik (2019). "Predicting the X-Ray Spectra of Stellar-mass Black Holes from Simulations". In: *ApJ* 873.1, 71, p. 71. DOI: `10.3847/1538-4357/ab05d5`.

Reynolds, Christopher S. (2014). "Measuring Black Hole Spin Using X-Ray Reflection Spectroscopy". In: *Space Sci. Rev.* 183.1-4, pp. 277–294. DOI: `10.1007/s11214-013-0006-6`. arXiv: `1302.3260 [astro-ph.HE]`.

García, J. A., T. R. Kallman, M. Bautista, C. Mendoza, J. Deprince, P. Palmeri, and P. Quinet (2018). "The Problem of the High Iron Abundance in Accretion Disks around Black Holes". In: *Astronomical Society of the Pacific Conference Series*. Vol. 515. Astronomical Society of the Pacific Conference Series, p. 282. arXiv: `1805.00581 [astro-ph.HE]`.

Reynolds, Christopher S., Laura W. Brenneman, Anne M. Lohfink, Margaret L. Trippe, Jon M. Miller, Andrew C. Fabian, and Michael A. Nowak (2012). "A Monte Carlo Markov Chain Based Investigation of Black Hole Spin in the Active Galaxy NGC 3783". In: *ApJ* 755.2, 88, p. 88. DOI: `10.1088/0004-637X/755/2/88`. arXiv: `1204.5747 [astro-ph.HE]`.

Chapter 2

Predicting Fe Kα Emission Line Profiles

This chapter was originally published as “Fe Kα Profiles from Simulations of Accreting Black Holes” in *The Astrophysical Journal*, volume 826, in July 2016.

The immediate environment of black holes offers a unique laboratory for high energy astrophysics. Accretion onto black holes is among the most efficient astrophysical processes for the transformation of potential energy into electromagnetic radiation—it is the mechanism responsible for their prodigious luminosity. In addition, black holes provide an opportunity to explore the strong-field regime ($GM/Rc^2 \sim 1$, where M and R are the mass and characteristic scale of the gravitational source, respectively) of General Relativity. The Fe Kα line can reveal valuable information about this regime. Due to the relatively high abundance of iron in the Universe and its efficient production of photons by fluorescence and recombination, a strong emission line can be created so long as a strong hard X-ray source is available. In addition, a relativistically broad line profile is an immediate signal of an origin deep in a gravitational potential well. Relativistically broadened Fe Kα lines have been observed in both supermassive active galactic nuclei (AGNs) (Tanaka et al., 1995; Nandra et al., 2007; Brenneman and Reynolds, 2009), stellar-mass galactic black holes (Miller et al., 2004; Reis et al., 2008; Reis et al., 2009), and galactic neutron stars (Cackett et al., 2010).

Detailed observations of this line therefore offer a direct channel to dynamics in the strong-field regime of General Relativistic gravity. In principle, its flux, energy profile, and variability properties could constrain many aspects of accretion dynamics, disk coronae, and possibly General Relativity itself [e.g., Fe Kα reverberation-mapping can lead to scale estimates: Kara et al. (2015) and references therein]. The shape of the Kα profile has already been used as a tool with which to measure black hole spin [see Reynolds (2013) and Miller and Miller (2015) for reviews], and several dozen individual measurements have been reported. However, interpretation of such data to date has in general relied upon "phenomenological" models. For example, spin parameter inferences often rely on assumed functional forms of the Fe Kα surface brightness, typically decreasing power-laws in the radial coordinate with some inner radius cutoff [see Reynolds and Nowak (2003) for a review]. At best, these assumptions introduce additional parameters, but it is also possible that the chosen functional forms do not resemble the actual surface brightness profile. Many models (which we discuss below) *do*, in fact, perform radiative transfer and photoionization calculations; these form the class of disk reprocessing codes, like that which we discuss below. These more sophisticated models nonetheless must still make arbitrary assumptions about important physical quantities such as the spatial-dependence of the X-ray flux striking the disk and the internal density structure of the matter within the disk.

These difficulties are well-illustrated by the common assumption that the inner cutoff of Fe Kα emission falls precisely at the radius of the innermost stable circular orbit (ISCO). As the radius of the ISCO is a one-to-one function of the central black hole spin, the radius of disk truncation enters into parametric models as a proxy for the spin. But does the disk—and, presumably, the Fe Kα emission—*in fact* truncate right at the radius of the ISCO (Reynolds and Begelman, 1997; Krolik and Hawley, 2002)? Matter which has passed through the ISCO must still travel to the event horizon, so the density is necessarily nonzero there—and perhaps the Fe Kα surface brightness is as well. Moreover, as the inward radial acceleration begins outside the ISCO (Krolik, Hawley, and Hirose, 2005), the fall in surface density also starts there; the cutoff in Fe Kα surface brightness might then likewise be found outside the ISCO. Thus, in order to make the Fe Kα line a *quantitative* diagnostic, it is essential to understand better the physical processes controlling its emission.

To this end, we have built numerical machinery to predict Fe Kα emission in a way that is as close to first principles and as free from arbitrary assumptions and parameters as possible. We show how it is possible to go directly from the data generated by a General Relativistic magnetohydrodynamic accretion simulation to observed Fe Kα line profiles using *only* well-understood physics. Below we describe the method, and present an example case: a $10M_\odot$ Schwarzschild black hole accreting at 1% of the Eddington rate.

2.1 From First Principles to Fe Kα Line Profiles

The simple model of accretion onto a black hole consists of an optically thick, geometrically thin disk, above and below which is a diffuse, hot corona (Liang, 1979; Haardt and Maraschi, 1991). Thermal photons emitted from the disk surface are boosted to high energies via inverse Compton scattering with mildly relativistic electrons in the corona. Some of these upscattered photons re-impinge on the disk surface, and those with sufficient energy—above the Fe K-edge at approximately 7.0 keV—eject inner shell electrons from iron atoms. As higher energy electrons fall to the now vacant lower energy levels, fluorescent photons of energy ranging from 6.4 keV to 7.0 keV, depending on iron ionization state, are emitted, forming the characteristic and prominent Fe Kα emission line frequently observed in black hole X-ray spectra. The shape and strength of the iron line is a function of how the Fe Kα emission varies over the disk surface, which in turn depends on the disk's thickness and vertical density profile, its temperature structure, the shape and intensity of the irradiating flux, and the iron abundance.

2.1.1 The Disk Structure and the Irradiating Flux

Our calculation begins with the General Relativistic three-dimensional magnetohydrodynamic (GRMHD) code HARM3D (Noble, Krolik, and Hawley, 2009). HARM3D is an intrinsically conservative GRMHD code which yields dynamic, three-dimensional information about the fluid density, four-velocity, magnetic pressure, gas pressure, and cooling at every point throughout the computational domain. To ensure the production of a geometrically thin disk—in the sense that its aspect ratio, $H_{\rm dens}/r$ (where $H_{\rm dens}$ is the density-weighted scale height), remains small—HARM3D solves a modified stress-energy conservation equation: in gravitationally-bound gas above a target temperature T_*, excess heat is radiated away on an orbital timescale. The target temperature T_* is chosen so as to achieve a target aspect ratio. Thus, at this point, we require only a target aspect ratio and the dimensionless spin parameter. For what follows, we consider one representative snapshot of a high-resolution simulation with $H_{\rm dens} = 0.06$, $a/M = 0$ (Noble et al., 2011), and at time $t = 12500M$, when the disk is nearly in a steady-state, i.e., inflow equilibrium.

The next step is to scale the simulation results from dimensionless code units to physical (i.e., cgs) units, a procedure summarized in Schnittman, Krolik, and Noble (2013). This requires the further specification of a central black hole mass M, which sets the natural length and time scales (because we define $G = c = 1$, both time and space are measured in units of the black hole mass M; $1M = 4.9(M/M_\odot) \times 10^{-6}$ s $= 1.5(M/M_\odot) \times 10^5$ cm), and the accretion rate $\dot{M}$, which sets the scale for the gas density, cooling rate, and magnetic pressure.

We then construct the photosphere surfaces, which separate the disk from the upper and lower coronae, by integrating the optical depth $d\tau = \kappa\rho(r, \theta, \phi)\sqrt{g_{\theta\theta}}d\theta$, where κ is the Thomson scattering opacity, at constant (r, ϕ) from the poles at $\theta = 0, \pi$ toward the $x - y$ plane. The upper and lower photospheres are those surfaces, $\Theta_{\rm top}(r, \phi)$ and $\Theta_{\rm bot}(r, \phi)$, respectively, for which the integrated optical depth reaches unity; the midplane, $\Theta_{\rm mid}(r, \phi)$, is that surface for which the integrated optical depths from both poles are equal—it is typically close to $\pi/2$, but varies in space and time.

Surfaces of constant optical depth can also be constructed for other values of τ—of particular relevance to our transfer solution is the $\tau = 0.1$ surface. We consider the region between the $\tau = 0.1$ and $\tau = 1$ surfaces to be a "boundary layer" between the disk and

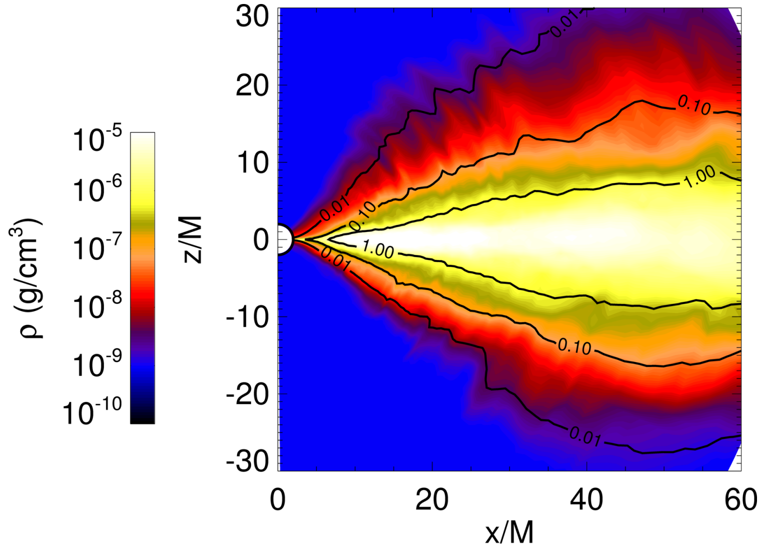

Figure 2.1: The $\phi-$averaged gas density drawn from HARM3D at $t = 12500M$, scaled to $10M_\odot$ and $\dot{m} = 0.01$ as described in the text, with several surfaces of constant optical depth overlaid.

corona (see below). A schematic illustrating how these surfaces relate to one another and to the geometry of a Schwarzschild black hole is presented in Figure 2.3. Figures 2.1 and 2.2 show $\phi-$averaged density and temperature maps, respectively, for the snapshot of the simulation we consider here, with several surfaces of constant optical depth overlaid. The density snapshot illustrates the sharp vertical density gradient associated with the disk's small scale height. It also shows the location of the photospheric ($\tau = 1$) surface; even after azimuthal-averaging, there is still significant irregularity in this surface, the result of the large amplitude turbulence within the disk. The temperature snapshot demonstrates how poor an approximation it is to think of the corona as a single zone: the temperature ranges from ~ 1 MeV in the nearly hollow cone along the polar axis to only a few keV just outside the disk photosphere.

In order to determine the shape and intensity of the hard X-ray flux incident upon each point of the disk surface, we employ PANDURATA, a Monte Carlo relativistic radiation transport code (Schnittman and Krolik, 2013). PANDURATA launches thermal seed photons from the photosphere (the $\tau = 1$ surfaces, see Figure 2.3) and follows their trajectories

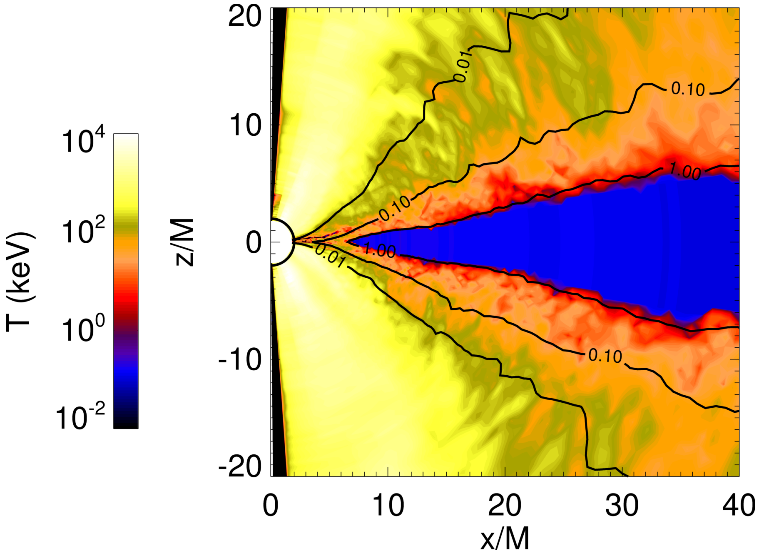

Figure 2.2: The $\phi-$averaged electron temperature computed by PANDURATA as described in the text, with several surfaces of constant optical depth overlaid.

through the curved spacetime around the black hole. These seed photons have a hardened blackbody energy distribution at a temperature consistent with the local cooling within the disk body as determined by HARM3D. That is, $T_{\rm eff}$ at the photospheres $\Theta_{\rm top}$ and $\Theta_{\rm bot}$ at a given (r, ϕ) is set by assuming that the energy dissipated between them is radiated thermally at each photosphere equally (Schnittman, Krolik, and Noble, 2013)—i.e., $\int_{\Theta_{\rm bot}}^{\Theta_{\rm top}} \mathcal{L} d\theta \sqrt{g_{\theta\theta}} = 2\sigma T_{\rm eff}^4$. The $\phi-$averaged effective temperature at the photosphere, as a function of radius, is shown in Figure 2.4. For most of the disk, the effective temperature declines slowly with radius, $\propto r^{-1/3}$, steepening to $\propto r^{-3/4}$ at large radii. Some of these thermal seed photons escape to infinity (making up part of the observed spectrum), while some are lost to the black hole; others re-impinge on the disk surface, having been upscattered by relativistic electrons in the corona.

In PANDURATA, as photons traverse the corona, they have a chance to Compton scatter according to the opacity along their route. When a photon does scatter, the electron's velocity in the local fluid frame is chosen according to a relativistic thermal velocity distribution corresponding to the electron temperature at that point. The photon's new direction is chosen from the Compton scattering partial cross section, and its new energy is then computed

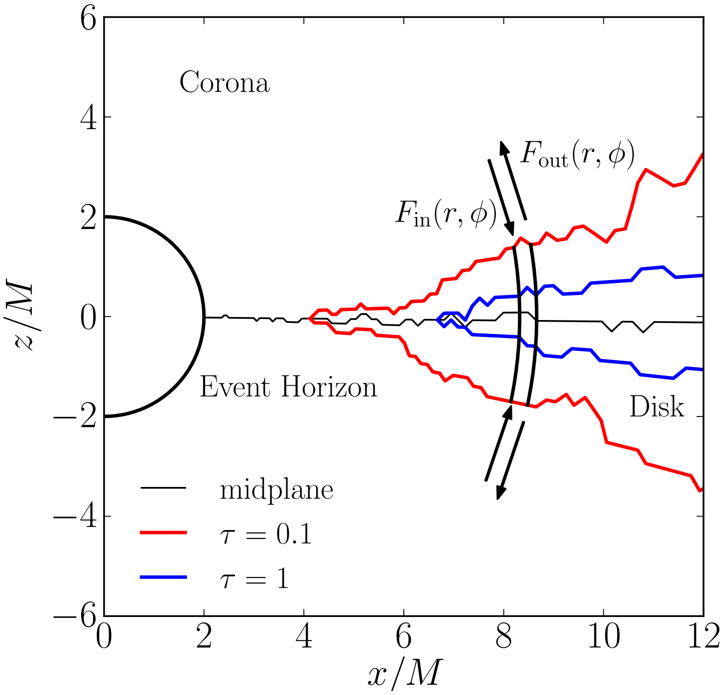

Figure 2.3: A schematic, cross-sectional view of the black hole environment. For a Schwarzschild black hole, the event horizon is at $r = 2M$, and the ISCO (not labeled here) is at $6M$ in the equatorial plane. The red and blue lines indicate the $\tau = 0.1$ and $\tau = 1$ surfaces of constant optical depth; the thin black line indicates the midplane. The region outside the event horizon and the disk is the corona; the region between the $\tau = 0.1$ and $\tau = 1$ surfaces is a "boundary layer" between the corona and disk. The pair of solid black lines connecting the upper and lower $\tau = 0.1$ surfaces represent one of the finite columns in which we perform our transfer and photoionization solution. The arrow labeled $F_{\mathrm{in}}(r,\phi)$ (and its counterpart for the lower surface) indicates the (energy-dependent) flux incident upon the disk at that (r,ϕ), computed by PANDURATA as described in the text. The arrow labeled $F_{\mathrm{out}}(r,\phi)$ indicates the reprocessed emission (e.g., Fe Kα photons) computed by PTRANSX.

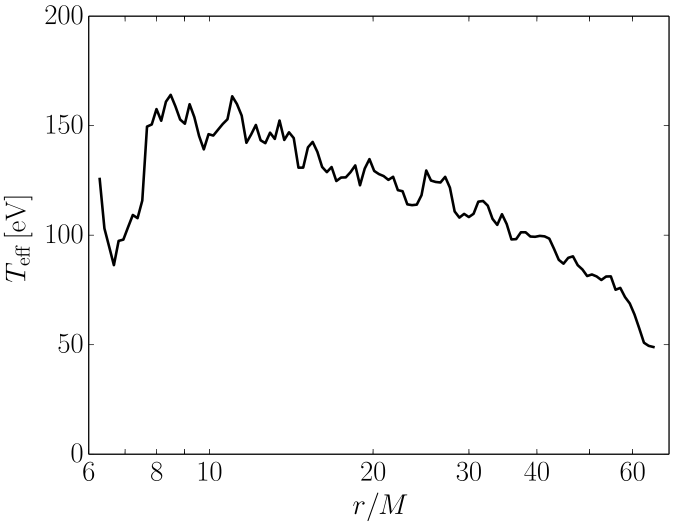

Figure 2.4: The $\phi-$averaged effective temperature at the disk photosphere (the $\tau = 1$ surface).

using standard relativistic dynamics. The new photon 4-momentum is then transformed back into the global coordinate frame. Eventually, a sufficient number of such events have occurred throughout the corona to permit evaluation of the inverse Compton (IC) power [the dominant emission mechanism in the corona (Schnittman, Krolik, and Noble, 2013)] at each coronal cell by directly comparing the incoming and outgoing photon energies. This value for the IC power at each coronal cell is then compared to the cooling rate found there by HARM3D, and the electron temperature (see Figure 2.2) is adjusted so that the former better matches the latter—and so on, until ultimately a self-consistent picture of the coronal radiation field emerges, including the hard X-ray component incident upon both $\tau = 0.1$ surfaces. This flux is shown, at several radii, in Figure 2.5, compared to the spectrum as seen by a distant observer over the same range. The incident flux is well described by a power-law in energy with index ranging from -0.8 to -1.8, steepening at larger radii. The flux as seen by the distant observer is also a power-law in energy, with index -1.4, nearly independent of inclination. Thus, at small radii, the incident spectrum is somewhat harder than observed, while at larger radii ($r \gtrsim 15M$) it is somewhat softer than observed [cf. Fürst

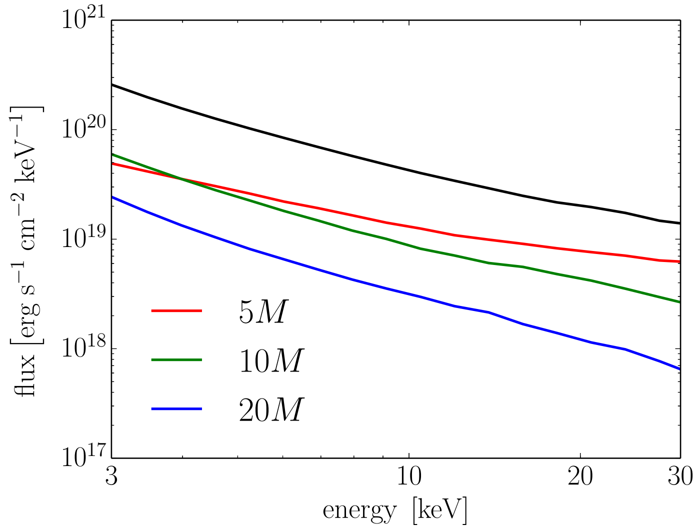

Figure 2.5: The $\phi-$averaged X-ray flux incident upon the upper $\tau = 0.1$ surface as a function of energy at three sample radii, compared to the flux in the same range as seen by a distant observer at $i = 45°$ (in black). The overall scale for the black curve is arbitrary, and it is placed above the other three to facilitate comparison.

et al. (2015)]. See Schnittman, Krolik, and Noble (2013) for more details on the observed continuum spectra.

Thus, having specified only the mass M, spin a, accretion rate $\dot{M}$, a list of elemental abundances, and a fiducial aspect ratio to ensure a geometrically thin disk, we construct a disk with a known density structure and a known flux irradiating its surface.

2.1.2 The Transfer Solution

As briefly mentioned in section 2.1.1, we divide the simulation region into three portions: the disk proper, the corona, and a boundary layer connecting the disk proper and the corona. Because the physical circumstances in each of these three regions are different, we need to employ different methods in each. In the corona, essentially every atom (even the heavy elements) is fully-stripped, and thermodynamics is thoroughly dominated by MHD-driven dissipative heating and inverse Compton cooling; there a code like PANDURATA is clearly the appropriate description for both radiation transfer and temperature balance. On the other hand, in the disk proper, where much of the Fe Kα emission is made, some elements (principally Fe) retain a few electrons, while MHD heating is supplemented by photoionization heating, and inverse Compton cooling becomes unimportant relative to a variety of atomic cooling processes. What is needed there is a photoionization solution whose continuum transfer scheme includes scattering; we find this with a new code we have constructed, which we call PTRANSX. The boundary layer is the region where coronal physics gradually gives way to disk physics. In this region, we need to employ *both* methods.

Although the boundary layer, by definition, does not have well-defined edges, we find it convenient to place its outer edge at $\tau = 0.1$ and its inner edge at $\tau = 1$. So long as the volume in which the photoionization solution is carried out contains the vast majority of fluorescing Fe atoms, the choice of which *specific* surface of constant optical depth we choose for the boundary layer's outer edge is not important—choosing $\tau = 0.05$, for example, would yield similar results, but at the cost of extending PTRANSX's calculation into the region better suited to PANDURATA. Conversely, there is some flexibility in setting the inner edge as well, but the primary consideration is to include all regions in which the electron temperature is high enough to upscatter photons significantly.

Within the boundary layer as we have defined it, Fe is the only element not fully-stripped. Consequently, only photons whose energy is just above the Fe K-edge are subject to absorptive opacity. We verify this assertion *post hoc*: over a wide range in photon energy and radius, we find that the absorption optical depth across the boundary layer is small except for energies just above the Fe K-edge at radii $\simeq$ 10–15M. This energy range is, of course, important for Fe Kα emission, so we treat its transfer accurately with PTRANSX; its narrowness, however, means that approximations to its transfer in PANDURATA have very little effect on the broadband continuum spectrum. For these reasons, we use PANDURATA to provide a first approximation to continuum transfer and electron temperature in the boundary layer. However, we also need to compute a PTRANSX equilibrium in this region for two reasons: because it can contribute significantly to Fe Kα emission (see Figure 2.9 below), and because there can be places where the photoionization heating due to Fe K-edge absorption raises the temperature above the PANDURATA-derived value. To achieve as reliable a result as possible, we therefore begin the treatment of this region with PANDURATA, but then follow up with PTRANSX.

PTRANSX is built upon the subroutines of the photoionization code XSTAR (Kallman and Bautista, 2001) that calculate the local temperature, ionization, emissivity, and opacity. XSTAR's built-in transfer scheme is insufficient for our purposes both because it does not include scattering, which is an important effect in determining the effective Fe Kα yield (see below), and because it does not allow for a slab illuminated on *both* sides, which—at small radii where the disk's total optical depth falls below order unity—has important consequences for the transfer solution. Instead, our continuum transfer solution employs Feautrier's method [see Mihalas (1978) and Mihalas (1985) for a description of the method and numerical algorithm used here] applied to finite plane-parallel slabs, each of which is the region between the upper and lower $\tau = 0.1$ surfaces (see Figure 2.3) at fixed (r, ϕ). That is, we take for the density structure in one slab the (curved) column of cells from one snapshot of the GRMHD simulation with the same (r, ϕ) but with θ increasing from its value at the upper $\tau = 0.1$ surface to its value at the lower $\tau = 0.1$ surface (as in Figure 2.3).

Because PTRANSX solves the continuum transfer problem for the boundary layer and the disk together, its radiation boundary conditions are taken from the PANDURATA solution evaluated on the upper and lower $\tau = 0.1$ surfaces, assuming isotropy of the incident radiation in the respective half-spaces. The transfer solutions in each (r, ϕ) slab are independent, and we justify this approximation by noting that the ionization parameter near the disk surface varies relatively slowly in space except for a region between $12M$–$14M$ in radius; this annulus, however, accounts for only a few percent of the total Fe Kα emission. In addition, we set all elemental abundances, including iron, to their solar values—that is, we set $A_{\mathrm{Fe}} = 7.50$ (Grevesse, Noels, and Sauval, 1996).

At each point within the disk proper and the boundary layer, we define a floor temperature. In the disk proper, it is $T_{\rm floor} = T_{\rm eff}\tau^{1/4}$ (Mihalas, 1978). Above and below the photospheres (that is, in the boundary layer), we scale the floor temperature as $T_{\rm floor} = T_1\tau^{-3/4}$ (Schnittman, Krolik, and Noble, 2013), where T_1 is the temperature found by PANDURATA just outside the photosphere. If the temperature corresponding to photoionization equilibrium (as computed by XSTAR) exceeds the floor temperature at any point, we use the photoionization equilibrium temperature; otherwise, we use the floor temperature. We make these choices because in the thermal balance performed by PANDURATA, only MHD dissipation and Compton processes are included, whereas PTRANSX includes all the atomic heating and cooling processes as well as Compton energy exchange, excluding only MHD dissipation; thus, the larger of the two temperatures should generally be the better approximation. This scheme is valid, of course, only if a disk photosphere exists for which we might specify a value for $T_{\rm eff}$. At small radii for which no photosphere exists—i.e., where the disk is optically thin, so defining an effective temperature by assuming radiation-gas thermal equilibrium is not physically reasonable—we simply adopt the temperature corresponding to photoionization equilibrium, with no floor. While the floor temperature is invoked within the disk body for nearly every slab at $r \gtrsim 10M$, removing the floor temperature entirely affects the Fe Kα yield by about only 10% (at least in this particular case).

We discretize each slab into cells such that the Thomson scattering optical depth, defined at the boundary of each cell, increases logarithmically from its value at the upper surface to its maximum value at the midplane, and likewise for the lower surface to the midplane. Further, we discretize μ, the cosine of the angle with respect to the local plane normal (i.e., the $\hat{\theta}$ unit vector), into evenly-spaced bins between -1 and 1, and the energy into logarithmically spaced bins between 1 eV and 500 keV; additional, evenly-spaced energy bins are added to the 6.3–7.0 keV region in order to resolve Fe Kα emission. For the analysis we consider below: 128 optical depth cells are spaced such that $\Delta\tau/\tau \simeq 0.01$–$0.09$, nearer to the lower value except for (r, ϕ) slabs at least several M exterior to the ISCO; we employ 16 angle groups; and 1000 energy bins are spaced such that $\Delta E/E \simeq 0.013$, with 700 additional bins in the 6.3–7.0 keV range. Numerical experimentation shows that the relevant results of our calculations are not appreciably affected by increasing the resolution beyond the values quoted above (for our purposes, in fact, far fewer angle groups are needed). Finally, we assume isotropic and coherent scattering.

We determine a self-consistent internal radiation field in the following way. Initially, we assume the gas to be completely ionized, so that there is zero true absorption. The scattering opacity at each point is known, given the density and corresponding electron number density. We then solve the equation of radiation transfer for the specific intensity as a function of angle, energy, and position. This procedure yields a value for the energy-dependent mean intensity at each point, which, along with the elemental abundances, density, and temperature floor, is supplied to the XSTAR subroutines. These then return local values for the energy-dependent continuum absorption and continuum emissivity (including thermal bremsstrahlung, radiative recombination, and two-photon decays of metastable levels), line emissivity (both continuum and line emission are treated as isotropic), the free electron fraction, and photoionization equilibrium temperature (so long as it exceeds the floor, if supplied). From these values, we update the source function and opacities—and then re-solve the equation of radiation transfer, the mean intensity from which is again input for XSTAR. We iterate until our quantity of interest—the Fe Kα emission—has converged to within 1%; this typically requires ~ 10 iterations. In this fashion we arrive at a self-consistent radiation field, ionization balance, and temperature throughout the slab.

The computation of Fe Kα emission is more detailed. The local emissivity due to a very large number of bound-bound transitions is computed by XSTAR as part of the iterative solution described above. In the normal course of the solution, the line emissivities are binned with the continuum emissivities when computing the source function at each point—the outgoing flux determined this way includes both continuum and line contributions. After the convergence criterion is met, the Feautrier method is employed once again, but with the source function including *only* continuum emission. In the 6.3–7.0 keV range, line emissivity greatly exceeds continuum emissivity virtually everywhere in the disk; the outgoing continuum in this range is due to the reflected (or transmitted, at small radii) incident flux. All other quantities—e.g., the continuum scattering and absorption opacities—are those determined self-consistently with the *full* radiation field. This final step yields the outgoing continuum flux, which is then subtracted from the outgoing total flux to arrive at the line emission part only, with no continuum-fitting necessary. We ignore the resonant absorption of Fe Kα lines on the basis that their escape probabilities—computed by XSTAR [see the XSTAR documentation (Kallman and Bautista, 2001) and references therein]—are all very near to unity for the parameters considered here. The escape probability calculation requires knowledge of the local turbulent velocity of the gas, which we take, fiducially, as 5% the Keplerian orbital velocity (a figure consistent with the disk's aspect ratio). However, the statement that the escape probabilities for line photons in the vicinity of the Fe Kα line are nearly unity remains true over a wide range of turbulent velocities relative to the orbital velocity. Since the opacity for resonant absorption is small and such events are rare, we also safely ignore Auger destruction (Ross, Fabian, and Brandt, 1996; Kallman et al., 2004).

The end result of this calculation is that, starting from a small number of assumptions and working from first principles, we arrive at a self-consistent model of the line emission over the disk surface. In what follows, we restrict our attention to the Fe Kα emission. As the energy of the Kα emission varies with Fe ionization state, from 6.41 keV in neutral Fe to 6.97 keV in H-like Fe (Krolik and Kallman, 1987), and because there are small but not completely negligible contributions from other heavy elements in this range, what we refer to as *the* Fe Kα flux is the sum of all emitted line photon fluxes in the range 6.3–7.0 keV.

There are fundamental differences between what we present here and previous disk reprocessing codes. First, we use plane-parallel slabs of *finite* thickness which are illuminated by the corona on both sides, whereas it is usually assumed that the disk is *semi-infinite* [cf. REFLION (Ross and Fabian, 2005), the XILLVER code of García and Kallman (2010), García, Kallman, and Mushotzky (2011), and García et al. (2013), and its extension RELXILL (García et al., 2014)]. This is an important distinction, because the total optical depth of the disk drops to $\lesssim 1$ in its inner region, where the radiative diffusion approximation, which typically supplies the lower boundary condition for transfer calculations [e.g., a blackbody, with the radial temperature-dependence of Shakura and Sunyaev (1973), placed at some large optical depth beneath the disk surface], is not valid. In contrast, our upper and lower boundary conditions—the flux incident upon the upper and lower $\tau = 0.1$ surfaces—remain physical even when the disk becomes optically thin. Second, both the density structure of our plane-parallel slabs and the flux irradiating their surfaces are computed using realistic dynamic models instead of assumed on the basis of simple and often arbitrary analytic relations. Since inhomogeneities in the density structure can have important effects on Fe Kα production (Ballantyne, Turner, and Blaes, 2004), drawing it from an MHD simulation represents a particularly significant improvement.

Using the ray-tracing code PANDURATA, the Fe Kα photons are transported from the disk surface to an observer at infinity. This geodesic transport includes all special and General Relativistic effects, Compton scattering off coronal electrons, as well as returning radiation [photons that are deflected by the black hole's gravity and then scatter off the disk; see (Schnittman and Krolik, 2009)].

2.2 Results

2.2.1 Fe Kα Emission in the Fluid Rest Frame

Our Fe Kα surface brightness predictions are summarized in three figures. Figure 2.6 shows the Fe Kα surface brightness in the fluid rest frame for one quadrant of the accretion disk at a sampling of 394 (r, ϕ) points [8 evenly spaced azimuthal zones, each with 48–51 logarithmically ($\Delta r/r = 0.06$) spaced radial zones; the number of radial zones per azimuth varies depending on density variations at small radii (see Figure 2.6)] for one snapshot in time of our $10 M_{\odot}$, Schwarzschild, 1% Eddington case, assuming solar Fe abundance. The solid red

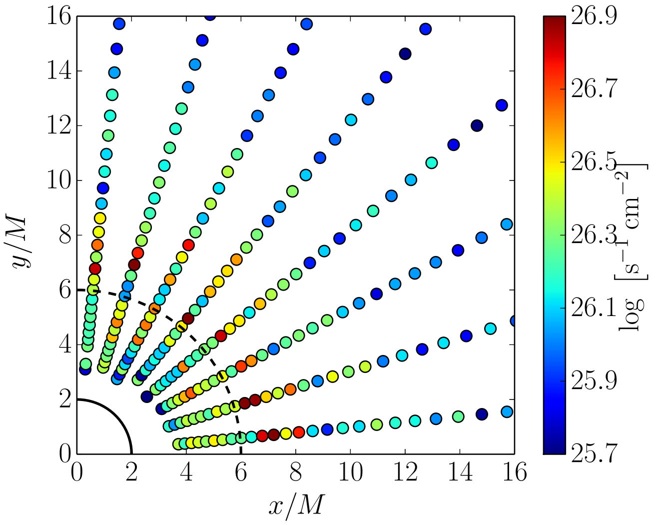

Figure 2.6: A sampling of the Fe Kα surface brightness in the fluid rest frame, of the upper disk surface for one quadrant of the accretion disk about a $10M_\odot$ Schwarzschild black hole, with an accretion rate of 1% the Eddington value. Not all (r, ϕ) points are shown in this view. The inner solid black line represents the location of the event horizon and the outer dashed black line represents the radius of the ISCO. The reverse view—looking up toward the midplane—is, on this scale, nearly indistinguishable.

line in Figure 2.7 presents the Fe Kα surface brightness for the $\phi = 0$ azimuthal slice of the same data (after the application of a smoothing kernel). The most salient feature of Figure 2.7 is the rough power-law in radius the Fe Kα emission appears to obey exterior to a maximum occurring at $\simeq 7M$, $\simeq 1M$ outside the ISCO. This behavior is more apparent in the ϕ-averaged picture of Figure 2.8, where we note that the the power-law portion of the ϕ-averaged Fe Kα surface brightness varies with radius with index -2. The steeper than $\propto r^{-2}$ decline from 7 to $8M$ seen in Figures 2.7 and 2.8 is due to two effects. First, as the disk becomes optically thick, some Kα photons are absorbed in the disk body before they escape. This also explains why the Fe Kα surface brightness of the upper and lower surfaces (the red and blue curves of Figure 2.7) vary together before $\simeq 8M$, but are independent at larger radii. In addition, the atomic fluorescence yield of Fe is dependent upon ionization state (see below), and the higher ionization found near $7M$ has an effectively higher atomic fluorescence yield than the less-ionized Fe at larger radii.

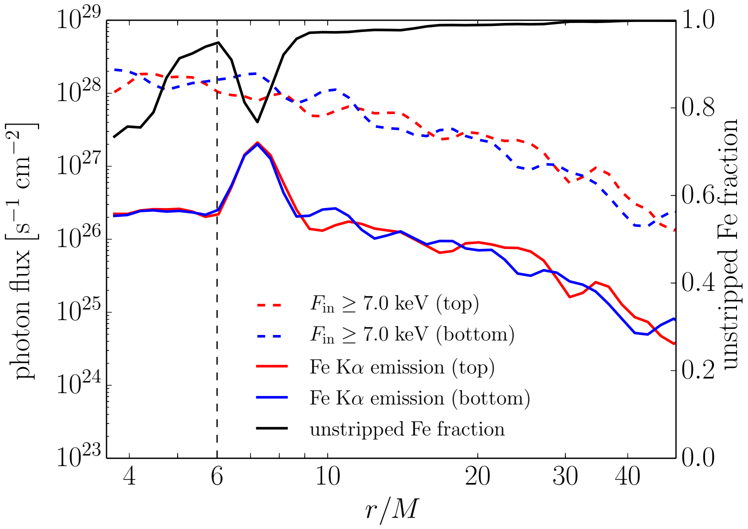

Figure 2.7: The red and blue solid lines are the Fe Kα surface brightness in the fluid rest frame for the $\phi = 0$ azimuth as a function of radius, for the upper and lower disk surfaces, respectively. The dashed red and blue lines are the photon flux incident upon the upper and lower disk surfaces, respectively, integrated above 7.0 keV. These four lines correspond to the left axis. The black line is the fraction of unstripped Fe atoms in the disk at $\phi = 0$ as a function of radius, corresponding to the right axis. The vertical dashed line indicates the ISCO. To facilitate interpretation, all curves have had a Gaussian smoothing kernel applied, with standard deviation equal to the radial cell spacing.

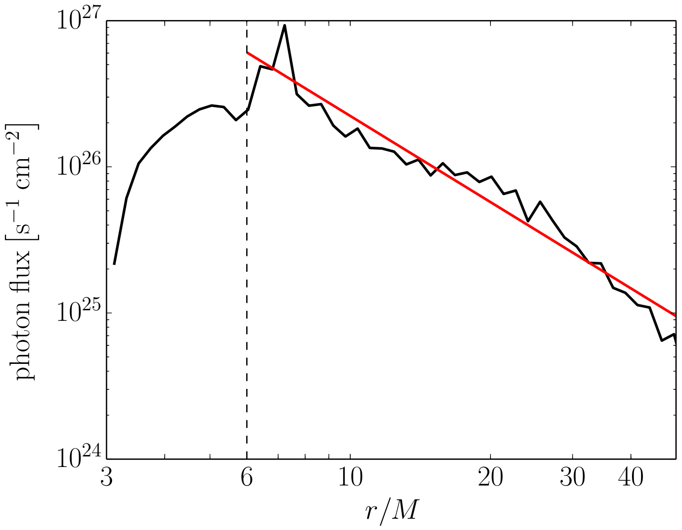

Figure 2.8: The black line is the Fe Kα surface brightness, averaged over the top and bottom of the disk and over azimuth. No smoothing kernel has been applied. The red line is a power-law fit to the region beyond $r \simeq 7M$. The fitted power-law index is -2. As in Figure 2.7, the dashed line indicates the radius of the ISCO.

To understand why the decline in Fe Kα surface brightness at small radii occurs, consider the black line in Figure 2.7, representing the fraction of Fe atoms in the disk at that radius and azimuth retaining at least one electron. At smaller radii, the disk's surface density decreases, and the ionization parameter increases; within about $10M$, the fraction of unstripped Fe begins to decrease. Though recombination onto bare Fe nuclei still provides a fluorescence mechanism in the highly ionized gas, the recombination rate is proportional to the unstripped Fe fraction, and so Fe Kα emission through recombination decreases at small radii as well. More importantly, the disk's column density decreases at small radii—there are simply fewer Fe atoms to undergo fluorescence.

Figure 2.7 also shows the photon flux incident upon the disk surface, integrated above 7.0 keV. The K-edge—the photon energy required to induce Kα fluorescence—varies with Fe ionization state, from approximately 7.1 keV for neutral Fe to 9.3 keV for H-like Fe (Kallman et al., 2004). The fluorescence yield—the fraction of absorbed K-edge photons resulting in the production of a Kα photon—varies with ionization state as well (Krolik and Kallman, 1987), but is typically ~ 0.5. It is at first surprising, then, that while the Fe Kα surface brightness in Figure 2.7 roughly follows the flux of incident photons above the K-edge—at least exterior to the peak at about $7M$—the former is approximately two orders of magnitude smaller than the latter, smaller than the factor of 0.5 we might expect from the fluorescence yield. Figure 2.9 provides a physical explanation. Due to the disk's high degree of ionization, Thomson scattering occurs throughout its volume, but appreciable Fe Kα production can occur only in those regions in which there is a sufficient population of unstripped Fe atoms. However, on much of the disk's surface, the incident flux is so large that a significant number of unstripped Fe atoms can exist only at optical depths where the flux has been substantially reduced by reflection. For the particular (r, ϕ) slab considered in Figure 2.9, we see that after one optical depth, beyond which the fraction of unstripped Fe reaches unity, approximately 40% of the photons incident upon the disk with energy above the K-edge have been absorbed or scattered out. This first optical depth accounts for slightly less than half of the total Fe Kα photons produced in (the half shown of) this slab, but for a greater portion of the Kα *emission*, since Kα photons produced at points deeper must diffuse through an optically thick disk body before escaping. Thus, the reflective outer layers of the accretion disk act to suppress Kα production, depressing the *effective* fluorescent yield relative to the *atomic* fluorescent yield. Nayakshin, Kazanas, and Kallman (2000) and García and Kallman (2010) note a similar "hot skin" effect, where the first optical depth or so of their irradiated slabs are at a much higher temperature and ionization than the underlying material. For the high ionization parameter cases of García and Kallman (2010), they report a marked decrease in the reprocessed Fe Kα equivalent width, generally consistent with our "depressed effective yield" interpretation.

Figure 2.9 also provides the justification for our choice to forego a redistribution function which accurately describes Compton scattering of Fe Kα lines in lieu of our simpler scheme. From Figure 2.9—which is qualitatively similar for any (r, ϕ) point exterior to $\simeq 7M$—we see that the median Fe Kα photon is produced at an optical depth ~ 1 below the disk surface,

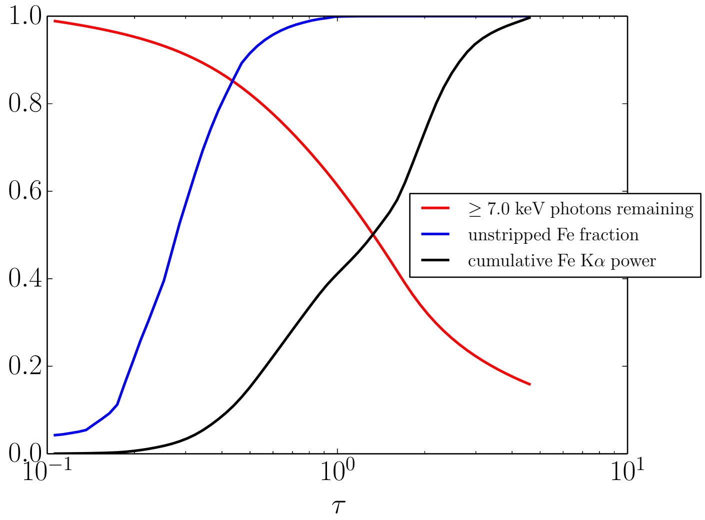

Figure 2.9: Cumulative Fe Kα (relative to the total Fe Kα power in one half of a disk slab), unstripped Fe fraction, and fraction of incident flux (above 7.0 keV) remaining as a function of scattering optical depth at $\phi = 0$, $r = 10M$. The lines terminate at the midplane for this azimuth and radius.

and therefore experiences on average one Compton scattering event as it escapes. Typically, $kT \sim 5$ keV in this region, so for Fe Kα photons with energy 6.3–7.0 keV, the broadening due to Compton scattering, $\sim 2\%$, is small. It should be noted that the effects of Compton heating and cooling are included in XSTAR's determination of the temperature, though the radiation field computed by PTRANSX does not reflect this.

2.2.2 Fe Kα Line Profiles

Figure 2.10 shows the shape of the Fe Kα lines as measured by a distant observer at several inclinations, including all special and General Relativistic effects, but without electron scattering of line photons in the corona; Figure 2.11 shows the line profiles with this effect included. The line profiles in both Figures 2.10 and 2.11 possess features similar to those from actual observations: the emission line is strongly and asymmetrically broadened, and at non-zero inclinations takes on a “double-horned” quality [compare, e.g., to the observational results discussed in Miller (2007)]. As might be expected, Compton scattering in the hot corona tends to redistribute line photons to higher energies. Such scatters are relatively few for photons initially directed upward from the disk, but they are much more numerous for photons that might otherwise go to observers closer to the disk plane. The result is to alter only slightly the line profiles seen by observers viewing the disk face-on, but to diminish the equivalent width of and broaden the line that observers with a more edge-on view might see [see Wilkins and Gallo (2015)].

The equivalent width of the Fe Kα line (as would be measured by a distant observer, and including coronal Compton scattering) as a function of inclination angle is presented in Figure 2.12. The equivalent widths we find, in the range 60–180 eV, are in agreement both with typical observational values [see Reynolds and Nowak (2003)] and previous disk reprocessing codes (namely REFLION, XILLVER, and RELXILL, as discussed above). It is important to note that the specific equivalent widths we report are for solar Fe abundance, though we expect the equivalent width to vary roughly linearly with Fe abundance. The dip centered at $i = 90°$—viewing the disk edge-on—is due to obscuration of the disk surface by the disk itself as well as losses due to Compton scattering in the corona. Due to gravitational lensing, even edge-on observers receive some of the line emission from the disk, and so the equivalent width does not go to zero at $i = 90°$.

2.3 Discussion

Figures 2.10, 2.11, and 2.12 represent the results achieved by our method. As we have stressed throughout the development above, our prediction of observed Fe Kα lines requires as input only a small number of physical parameters: the black hole mass and spin, the accretion rate, the iron abundance, and the observer inclination. Significantly, none of these parameters stands in for an unknown physical process. The most important aspect of Figure 2.11 is that it represents a quantitative *prediction* for how we expect the Fe Kα line profile to appear from a $10M_\odot$ Schwarzschild black hole accreting at 1% the Eddington value, predicated on fundamental physics. We combine global MHD simulations performed in full

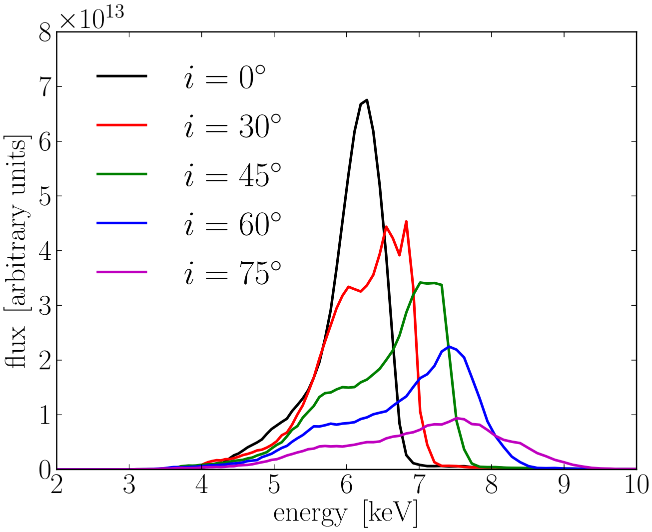

Figure 2.10: The Fe Kα line profile as would be seen by a distant observer, at several inclinations i (where 0° is viewing the disk face-on), excluding electron scattering of the line photons as they travel through the corona.

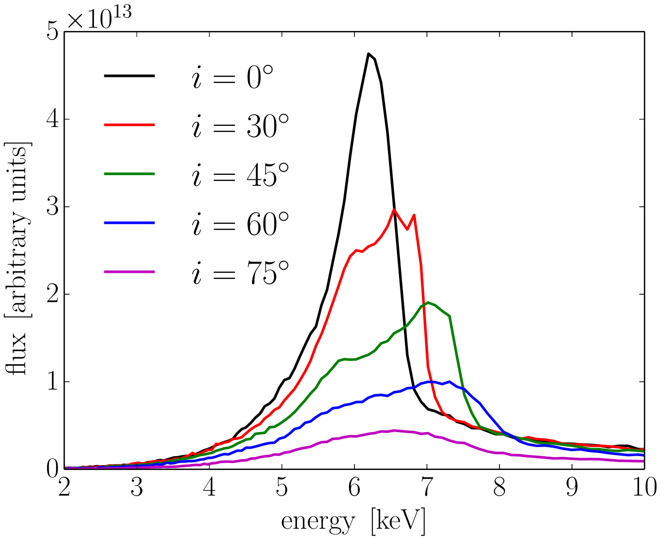

Figure 2.11: The Fe Kα line profile as would be seen by a distant observer at several inclinations, but including the effects of electron scattering of the line photons in the hot corona.

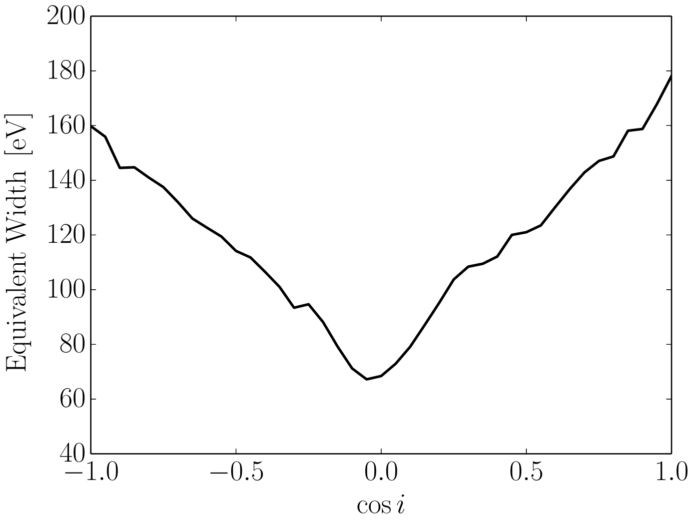

Figure 2.12: The equivalent width of the Fe Kα line as a function of observer inclination angle, including the effects of Compton scattering of the line photons through the corona.

GR, a Monte Carlo radiation transfer code to determine the electron temperature throughout the corona and the hard X-ray flux irradiating each point on the disk surface, and the disk reprocessing code we describe above to construct maps of the Fe Kα emission over the disk surface. The final results—Fe Kα line profiles—are observables founded upon the physics which describe accreting black hole systems. The most significant gap remaining in the physics is the equation of state used by the MHD code. The state-of-the-art for simulations of bright, but sub-Eddington, accretion onto black holes assumes a local optically thin cooling function designed to radiate quickly nearly all the heat dissipated, maintaining a disk scale height as a function of radius determined *a priori*. For the simulation used here, this scale height profile is close to what might be expected from conventional analytic accretion disk theory (Shakura and Sunyaev, 1973) assuming a radiation-dominated disk with $\dot{m} \simeq 0.2$. Schnittman, Krolik, and Noble (2013) present a more detailed account of the relation between analytic accretion disk theory and the terms of our simulation. As simulation codes coupling radiation transfer to MHD (Jiang, Stone, and Davis, 2014; Sądowski et al., 2014) become more efficient and eliminate restrictive approximations, it will be possible to close this gap.

Model fits to data typically assume that the Fe Kα surface brightness is axisymmetric and follows a power-law in radius with a cutoff at the ISCO. From Figure 2.8, it is clear that, for this particular example, our more careful approach validates this model to some extent: at least for the one point in the black hole parameter space we have considered, the radial variation in Fe Kα emission turns out to be roughly power-law. The fundamental difference is that the power-law index we find, -2, the location of the maximum, $r \simeq 7M$, and the very fact that the behavior is power-law at all, arise in a natural way from the calculation: they are neither fits to observations nor put in "by hand."

The power-law we find is, in fact, shallower than those typically used in phenomenological models, but this is a direct consequence of our *extended* coronal geometry. For radii greater than that of the peak surface brightness, the Fe Kα emission should vary like the incident hard X-ray flux—as in Figure 2.7. It is easily shown (in flat space) that if the corona is treated as a point source at some height z above the center of a disk of constant aspect ratio, the variation of the flux with the cylindrical radial coordinate r is either proportional to r^{-3} for the case when $z \ll r$, or independent of r in the case when $z \gg r$. Fully relativistic ray-tracing calculations of "lamppost" geometries, like those of Wilkins and Fabian (2012) and Dauser et al. (2013), typically find steep power-laws in the inner disk regions, where $z \gg r$, leveling off to r^{-3} at large radii, where $z \ll r$. When they investigate more extended, but still arbitrarily chosen, hard X-ray emissivity distributions (Wilkins and Fabian, 2012), the Kα emissivity in the region covered by the extended hard X-ray source roughly mirrors the coronal emissivity. Our *physically-derived* result that the Kα emissivity is $\propto r^{-2}$ is therefore a consequence of the similarly extended coronal emission that follows directly from the underlying MHD simulation. It is, however, important to note that the emissivity profile may change as a function of accretion rate, black hole spin, or black hole mass. Magnetic field topology may also be important, as the driver behind different coronal and jet properties (Beckwith, Hawley, and Krolik, 2008).

Of particular importance to the use of observed Fe Kα line profiles to infer black hole spin is the fact that we find the line emission peaks approximately $1M$ *outside* the ISCO. We have, of course, not performed a sufficiently detailed exploration of the black hole parameter space to determine whether this is a systematic effect—indeed, it is possible that for a different set of parameters, the peak may be found *inside* the ISCO. This latter alternative might, for example, be expected when the accretion rate (and thus disk surface density) is higher (Schnittman, Krolik, and Noble, 2013). In addition, in generating the line profiles of Figures 2.10 and 2.11, we keep track of three separate energy channels within the 6.3–7.0 keV range; higher ionization states of Fe produce Kα photons at greater energies, and this potentially several-hundred eV difference can have significant effects on the predicted line profile. As an illustration, we show in Figure 2.13 the Fe Kα line profiles seen by a distant observer using the power-law fit extended back to the ISCO from Figure 2.8, assuming all Fe Kα emission occurs at 6.4 keV (as is often done), compared to those generated by our method, i.e., from Figure 2.10. By moving the location of the interior cutoff inwards by M, removing physically important features—like the brief yet steep decline in flux from 7 to $8M$ discussed in the previous section—which are *not* captured by a pure power-law, and assuming all Kα photons are produced by near neutral Fe, the line profile is reddened and altered in shape. When comparing to observed spectra, this shift can be expected to have particularly important consequences for constraining the system's inclination, for example.

With further exploration of the parameter space, we will learn how variations in mass, spin, accretion rate, and Fe abundance manifest themselves in the strength and shape of the Fe Kα line profile. Ultimately, we envision the construction of a grid of model profiles spanning the parameter space, forming the foundation for an extension to XSPEC (Arnaud, 1996) which will take as input an X-ray spectrum of a stellar-mass black hole or AGN from an observatory such as *Chandra*, *XMM-Newton*, *Suzaku*, or *NuSTAR*, and will output the best-fit values of the intrinsic parameters, derived from physically-based, rather than phenomenological, models.

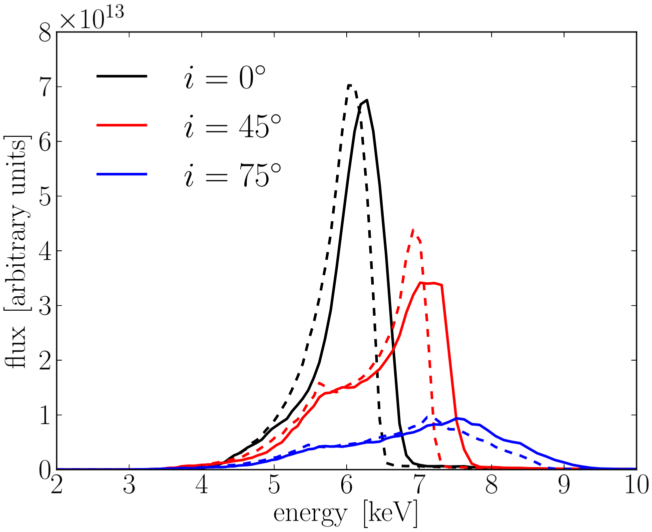

Figure 2.13: The Fe Kα line profile as would be seen by a distant observer at several inclinations: those in dashed lines were computed from the power-law fit extended back to the ISCO (assuming 6.4 keV Fe Kα photons), e.g., the red line in Figure 2.8, while those in solid lines are reproduced from Figure 2.10 for comparison; for both solid and dashed lines, color indicates inclination.

References

Tanaka, Y., K. Nandra, A. C. Fabian, H. Inoue, C. Otani, T. Dotani, K. Hayashida, K. Iwasawa, T. Kii, H. Kunieda, F. Makino, and M. Matsuoka (1995). "Gravitationally redshifted emission implying an accretion disk and massive black hole in the active galaxy MCG-6-30-15". In: *Nature* 375, pp. 659–661. DOI: `10.1038/375659a0`.

Nandra, K., P. M. O'Neill, I. M. George, and J. N. Reeves (2007). "An XMM-Newton survey of broad iron lines in Seyfert galaxies". In: *MNRAS* 382, pp. 194–228. DOI: `10.1111/j.1365-2966.2007.12331.x`. arXiv: `0708.1305`.

Brenneman, L. W. and C. S. Reynolds (2009). "Relativistic Broadening of Iron Emission Lines in a Sample of Active Galactic Nuclei". In: *ApJ* 702, pp. 1367–1386. DOI: `10.1088/0004-637X/702/2/1367`. arXiv: `0907.3850 [astro-ph.HE]`.

Miller, J. M., A. C. Fabian, C. S. Reynolds, M. A. Nowak, J. Homan, M. J. Freyberg, M. Ehle, T. Belloni, R. Wijnands, M. van der Klis, P. A. Charles, and W. H. G. Lewin (2004). "Evidence of Black Hole Spin in GX 339-4: XMM-Newton/EPIC-pn and RXTE Spectroscopy of the Very High State". In: *ApJL* 606, pp. L131–L134. DOI: `10.1086/421263`. eprint: `astro-ph/0312033`.

Reis, R. C., A. C. Fabian, R. R. Ross, G. Miniutti, J. M. Miller, and C. Reynolds (2008). "A systematic look at the very high and low/hard state of GX339-4: constraining the black hole spin with a new reflection model". In: *MNRAS* 387, pp. 1489–1498. DOI: `10.1111/j.1365-2966.2008.13358.x`. arXiv: `0804.0238`.

Reis, R. C., A. C. Fabian, R. R. Ross, and J. M. Miller (2009). "Determining the spin of two stellar-mass black holes from disc reflection signatures". In: *MNRAS* 395, pp. 1257–1264. DOI: `10.1111/j.1365-2966.2009.14622.x`.

Cackett, E. M., J. M. Miller, D. R. Ballantyne, D. Barret, S. Bhattacharyya, M. Boutelier, M. C. Miller, T. E. Strohmayer, and R. Wijnands (2010). "Relativistic Lines and Reflection from the Inner Accretion Disks Around Neutron Stars". In: *ApJ* 720, pp. 205–225. DOI: `10.1088/0004-637X/720/1/205`. arXiv: `0908.1098 [astro-ph.HE]`.

Kara, E., A. Zoghbi, A. Marinucci, D. J. Walton, A. C. Fabian, G. Risaliti, S. E. Boggs, F. E. Christensen, F. Fuerst, C. J. Hailey, F. A. Harrison, G. Matt, M. L. Parker, C. S. Reynolds, D. Stern, and W. W. Zhang (2015). "Iron K and Compton hump reverberation in SWIFT J2127.4+5654 and NGC 1365 revealed by NuSTAR and XMM-Newton". In: *MNRAS* 446, pp. 737–749. DOI: `10.1093/mnras/stu2136`. arXiv: `1410.3357 [astro-ph.HE]`.

Reynolds, C. S. (2013). “The spin of supermassive black holes”. In: *Classical and Quantum Gravity* 30.24, 244004, p. 244004. DOI: `10.1088/0264-9381/30/24/244004`. arXiv: `1307.3246 [astro-ph.HE]`.

Miller, M. C. and J. M. Miller (2015). “The masses and spins of neutron stars and stellar-mass black holes”. In: *Phys. Rep.* 548, pp. 1–34. DOI: `10.1016/j.physrep.2014.09.003`. arXiv: `1408.4145 [astro-ph.HE]`.

Reynolds, C. S. and M. A. Nowak (2003). “Fluorescent iron lines as a probe of astrophysical black hole systems”. In: *Phys. Rep.* 377, pp. 389–466. DOI: `10.1016/S0370-1573(02)00584-7`. eprint: `astro-ph/0212065`.

Reynolds, C. S. and M. C. Begelman (1997). “Iron Fluorescence from within the Innermost Stable Orbit of Black Hole Accretion Disks”. In: *ApJ* 488, pp. 109–118. eprint: `astro-ph/9705136`.

Krolik, J. H. and J. F. Hawley (2002). “Where Is the Inner Edge of an Accretion Disk around a Black Hole?” In: *ApJ* 573, pp. 754–763. DOI: `10.1086/340760`. eprint: `astro-ph/0203289`.

Krolik, J. H., J. F. Hawley, and S. Hirose (2005). “Magnetically Driven Accretion Flows in the Kerr Metric. IV. Dynamical Properties of the Inner Disk”. In: *ApJ* 622, pp. 1008–1023. DOI: `10.1086/427932`. eprint: `astro-ph/0409231`.

Liang, E. P. T. (1979). “On the hard X-ray emission mechanism of active galactic nuclei sources”. In: *ApJL* 231, pp. L111–L114. DOI: `10.1086/183015`.

Haardt, F. and L. Maraschi (1991). “A two-phase model for the X-ray emission from Seyfert galaxies”. In: *ApJL* 380, pp. L51–L54. DOI: `10.1086/186171`.

Noble, S. C., J. H. Krolik, and J. F. Hawley (2009). “Direct Calculation of the Radiative Efficiency of an Accretion Disk Around a Black Hole”. In: *ApJ* 692, pp. 411–421. DOI: `10.1088/0004-637X/692/1/411`. arXiv: `0808.3140`.

Noble, S. C., J. H. Krolik, J. D. Schnittman, and J. F. Hawley (2011). “Radiative Efficiency and Thermal Spectrum of Accretion onto Schwarzschild Black Holes”. In: *ApJ* 743, 115, p. 115. DOI: `10.1088/0004-637X/743/2/115`. arXiv: `1105.2825 [astro-ph.HE]`.

Schnittman, J. D., J. H. Krolik, and S. C. Noble (2013). “X-Ray Spectra from Magnetohydrodynamic Simulations of Accreting Black Holes”. In: *ApJ* 769, 156, p. 156. DOI: `10.1088/0004-637X/769/2/156`. arXiv: `1207.2693 [astro-ph.HE]`.

Schnittman, J. D. and J. H. Krolik (2013). “A Monte Carlo Code for Relativistic Radiation Transport around Kerr Black Holes”. In: *ApJ* 777, 11, p. 11. DOI: `10.1088/0004-637X/777/1/11`. arXiv: `1302.3214 [astro-ph.HE]`.

Fürst, F., M. A. Nowak, J. A. Tomsick, J. M. Miller, S. Corbel, M. Bachetti, S. E. Boggs, F. E. Christensen, W. W. Craig, A. C. Fabian, P. Gandhi, V. Grinberg, C. J. Hailey, F. A. Harrison, E. Kara, J. A. Kennea, K. K. Madsen, K. Pottschmidt, D. Stern, D. J. Walton, J. Wilms, and W. W. Zhang (2015). “The Complex Accretion Geometry of GX 339-4 as Seen by NuSTAR and Swift”. In: *ApJ* 808, 122, p. 122. DOI: `10.1088/0004-637X/808/2/122`. arXiv: `1506.01381 [astro-ph.HE]`.

Kallman, T. and M. Bautista (2001). “Photoionization and High-Density Gas”. In: *ApJS* 133, pp. 221–253. DOI: `10.1086/319184`.

Mihalas, D. (1978). *Stellar atmospheres, 2nd edition.* San Francisco, W. H. Freeman and Co.

Mihalas, D. (1985). “The computation of radiation transport using Feautrier variables. I - Static media”. In: *Journal of Computational Physics* 57, pp. 1–25. DOI: `10.1016/0021-9991(85)90050-6`.

Grevesse, N., A. Noels, and A. J. Sauval (1996). “Standard Abundances”. In: *Cosmic Abundances.* Ed. by S. S. Holt and G. Sonneborn. Vol. 99. Astronomical Society of the Pacific Conference Series, p. 117.

Ross, R. R., A. C. Fabian, and W. N. Brandt (1996). “X-ray reflection in Galactic black hold candidates: smeared edge profiles and resonant Auger destruction”. In: *MNRAS* 278, pp. 1082–1086. DOI: `10.1093/mnras/278.4.1082`. eprint: `astro-ph/9510022`.

Kallman, T. R., P. Palmeri, M. A. Bautista, C. Mendoza, and J. H. Krolik (2004). “Photoionization Modeling and the K Lines of Iron”. In: *ApJS* 155, pp. 675–701. DOI: `10.1086/424039`. eprint: `astro-ph/0405210`.

Krolik, J. H. and T. R. Kallman (1987). “Fe K features as probes of the nuclear reflection region in Seyfert galaxies”. In: *ApJL* 320, pp. L5–L8. DOI: `10.1086/184966`.

Ross, R. R. and A. C. Fabian (2005). “A comprehensive range of X-ray ionized-reflection models”. In: *MNRAS* 358, pp. 211–216. DOI: `10.1111/j.1365-2966.2005.08797.x`. eprint: `astro-ph/0501116`.

García, J. and T. R. Kallman (2010). “X-ray Reflected Spectra from Accretion Disk Models. I. Constant Density Atmospheres”. In: *ApJ* 718, pp. 695–706. DOI: `10.1088/0004-637X/718/2/695`. arXiv: `1006.0485 [astro-ph.HE]`.

García, J., T. R. Kallman, and R. F. Mushotzky (2011). “X-ray Reflected Spectra from Accretion Disk Models. II. Diagnostic Tools for X-ray Observations”. In: *ApJ* 731, 131, p. 131. DOI: `10.1088/0004-637X/731/2/131`. arXiv: `1101.1115 [astro-ph.HE]`.

García, J., T. Dauser, C. S. Reynolds, T. R. Kallman, J. E. McClintock, J. Wilms, and W. Eikmann (2013). “X-Ray Reflected Spectra from Accretion Disk Models. III. A Complete Grid of Ionized Reflection Calculations”. In: *ApJ* 768, 146, p. 146. DOI: `10.1088/0004-637X/768/2/146`. arXiv: `1303.2112 [astro-ph.HE]`.

García, J., T. Dauser, A. Lohfink, T. R. Kallman, J. F. Steiner, J. E. McClintock, L. Brenneman, J. Wilms, W. Eikmann, C. S. Reynolds, and F. Tombesi (2014). “Improved Reflection Models of Black Hole Accretion Disks: Treating the Angular Distribution of X-Rays”. In: *ApJ* 782, 76, p. 76. DOI: `10.1088/0004-637X/782/2/76`. arXiv: `1312.3231 [astro-ph.HE]`.

Shakura, N. I. and R. A. Sunyaev (1973). “Black holes in binary systems. Observational appearance.” In: *A&A* 24, pp. 337–355.

Ballantyne, D. R., N. J. Turner, and O. M. Blaes (2004). “X-Ray Reflection from Inhomogeneous Accretion Disks. I. Toy Models and Photon Bubbles”. In: *ApJ* 603, pp. 436–448. DOI: `10.1086/381495`. eprint: `astro-ph/0311390`.

Schnittman, J. D. and J. H. Krolik (2009). “X-ray Polarization from Accreting Black Holes: The Thermal State”. In: *ApJ* 701, pp. 1175–1187. DOI: `10.1088/0004-637X/701/2/1175`. arXiv: `0902.3982 [astro-ph.HE]`.

Nayakshin, S., D. Kazanas, and T. R. Kallman (2000). "Thermal Instability and Photoionized X-Ray Reflection in Accretion Disks". In: *ApJ* 537, pp. 833–852. DOI: `10.1086/309054`. eprint: `astro-ph/9909359`.

Miller, J. M. (2007). "Relativistic X-Ray Lines from the Inner Accretion Disks Around Black Holes". In: *ARA&A* 45, pp. 441–479. DOI: `10.1146/annurev.astro.45.051806.110555`. arXiv: `0705.0540`.

Wilkins, D. R. and L. C. Gallo (2015). "The Comptonization of accretion disc X-ray emission: consequences for X-ray reflection and the geometry of AGN coronae". In: *MNRAS* 448, pp. 703–712. DOI: `10.1093/mnras/stu2524`. arXiv: `1412.0015 [astro-ph.HE]`.

Jiang, Y.-F., J. M. Stone, and S. W. Davis (2014). "An Algorithm for Radiation Magnetohydrodynamics Based on Solving the Time-dependent Transfer Equation". In: *ApJS* 213, 7, p. 7. DOI: `10.1088/0067-0049/213/1/7`. arXiv: `1403.6126 [astro-ph.IM]`.

Sądowski, A., R. Narayan, J. C. McKinney, and A. Tchekhovskoy (2014). "Numerical simulations of super-critical black hole accretion flows in general relativity". In: *MNRAS* 439, pp. 503–520. DOI: `10.1093/mnras/stt2479`. arXiv: `1311.5900 [astro-ph.HE]`.

Wilkins, D. R. and A. C. Fabian (2012). "Understanding X-ray reflection emissivity profiles in AGN: locating the X-ray source". In: *MNRAS* 424, pp. 1284–1296. DOI: `10.1111/j.1365-2966.2012.21308.x`. arXiv: `1205.3179 [astro-ph.HE]`.

Dauser, T., J. Garcia, J. Wilms, M. Böck, L. W. Brenneman, M. Falanga, K. Fukumura, and C. S. Reynolds (2013). "Irradiation of an accretion disc by a jet: general properties and implications for spin measurements of black holes". In: *MNRAS* 430, pp. 1694–1708. DOI: `10.1093/mnras/sts710`. arXiv: `1301.4922 [astro-ph.HE]`.

Beckwith, K., J. F. Hawley, and J. H. Krolik (2008). "The Influence of Magnetic Field Geometry on the Evolution of Black Hole Accretion Flows: Similar Disks, Drastically Different Jets". In: *ApJ* 678, pp. 1180–1199. DOI: `10.1086/533492`. arXiv: `0709.3833`.

Arnaud, K. A. (1996). "XSPEC: The First Ten Years". In: *Astronomical Data Analysis Software and Systems V*. Ed. by G. H. Jacoby and J. Barnes. Vol. 101. Astronomical Society of the Pacific Conference Series, p. 17.

Chapter 3

Predicting the Complete X-ray Spectrum

This chapter was originally published as "Predicting the X-ray Spectra of Stellar-mass Black Holes from Simulations" in *The Astrophysical Journal*, volume 873, in March 2019.

Both active galactic nuclei and stellar-mass black hole binaries produce X-ray spectra with line and continuum features which convey information about the environment and spacetime geometry from which they originate. Relativistically-broadened Fe Kα fluorescence lines are one of the key indicators that these systems do in fact contain black holes (Tanaka et al., 1995), and the thermal plus power-law continuum indicates the presence of disk and corona, respectively (Liang, 1979; Haardt and Maraschi, 1991). Indeed, studying the governing physics of accretion processes is tied to our ability to connect the underlying theory to observations. The quantitative information inferrable from any spectrum is, however, limited by the templates to which the observation is compared.

To this end, we have developed a technique with which model spectra are computed directly from simulation data by applying the relevant physical principles while invoking almost no assumptions. The numerical machinery we describe here is an extension of that introduced in Kinch et al. (2016), where we applied our method only to the prediction of Fe Kα line profiles; below, we greatly expand the predictive scope of our method by treating the X-ray emission lines *and* the continuum in a self-consistent, energy-conserving fashion. In addition, we explore the effects of varying the nominal accretion rate on the predicted spectrum.

A variety of methods are currently in use for modeling the spectra of black hole systems. Some are purely phenomenological—the continuum is fit with a multicolor disk blackbody [e.g., DISKBB (Mitsuda et al., 1984)] plus a (typically broken) power-law at high energy, and the Fe Kα emission from the disk surface is assumed to vary as a decreasing power-law (or sometimes broken power-law) in radius with a hard cutoff at the innermost stable circular orbit (ISCO) and another at some outer radius [e.g., RELLINE (Dauser et al., 2013); see Reynolds and Nowak, 2003 for a discussion of these methods]. More sophisticated techniques model the continuum with a single-zone Comptonization region and the disk reprocessed component (the Fe Kα line, the K-edge, and the Compton bump) by performing detailed radiative transfer and photoionization calculations within a sample section of the disk [e.g., the codes REFLIONX (Ross and Fabian, 2005), XILLVER (García and Kallman, 2010; García, Kallman, and Mushotzky, 2011; García et al., 2013), and RELXILL (García et al., 2014)]. At present *all* methods rely in some way upon a parameterized description of the black hole environment: at best, an idealized corona (often a "lamppost" point source or a single homogeneous region) emits a power-law spectrum (perhaps with a thermal cutoff) which illuminates a semi-infinite, blackbody-radiating disk, and this disk has a knife-edge cutoff precisely at the ISCO. When using such a model to, for example, extract spin measurements from spectral data (Reynolds, 2013; Miller and Miller, 2015), the accuracy of the measurement is limited by the accuracy of the assumed accretion flow geometry and associated coronal flux.

By starting with 3D GRMHD simulation data, we greatly reduce the number of assumptions needed to describe the accretion flow geometry. We therefore also reduce the number of free parameters needed to specify a resulting observable spectrum. We do not, for example, require a sharp cutoff in Fe Kα emission at the ISCO, nor do we specify the coronal geometry (lamppost or otherwise) *a priori*; the density and temperature structure of the disk are not assumed in advance either. Instead, these are computed directly from the underlying physics, with the sole significant assumption being the equation of state employed by the simulation; as simulations improve, e.g., by the use of more realistic equations of state, our apparatus can easily be applied to their output as well. The resulting prediction of our method, the full inclination-dependent observable spectrum, is a function of a very small number of parameters, each physically meaningful: the black hole mass and spin, the nominal accretion rate, and the elemental abundances.

3.1 Method

Our procedure has three main components. First, an accreting black hole system is simulated using HARM3D (Noble, Krolik, and Hawley, 2009). We take a three-dimensional snapshot of the fluid density, four-velocity, and dissipation (cooling) rate at a time when the simulation has achieved approximate inflow equilibrium (out to $r \sim 20M$). Using a thermal seed photon injection rate computed by integrating the local dissipation rate within the disk's photosphere, the Monte Carlo radiation transport code PANDURATA (Schnittman and Krolik, 2013) determines the radiation field consistent with the simulation data and thermal balance in the corona (Schnittman, Krolik, and Noble, 2013). With HARM3D's description of the disk structure and PANDURATA's calculation of the disk incident flux, PTRANSX computes the disk's reprocessed *outgoing* flux, requiring photoionization equilibrium and energy conservation everywhere within the disk (Kinch et al., 2016). This step yields a new guess for both the energy-dependent seed photon flux emerging from the disk surface and the spatial- and energy-dependent disk albedo—input for the next PANDURATA run. We cycle between PANDURATA (in the corona) and PTRANSX (in the disk) until a consistent picture of the *global* radiation field develops. This cycling is a significant improvement to the original PANDURATA method. To avoid confusion between the iterative procedures within each step and the outermost iterations between PANDURATA and PTRANSX, we refer to the latter as "passes." With one final round of relativistic ray-tracing, both reprocessed disk and coronal

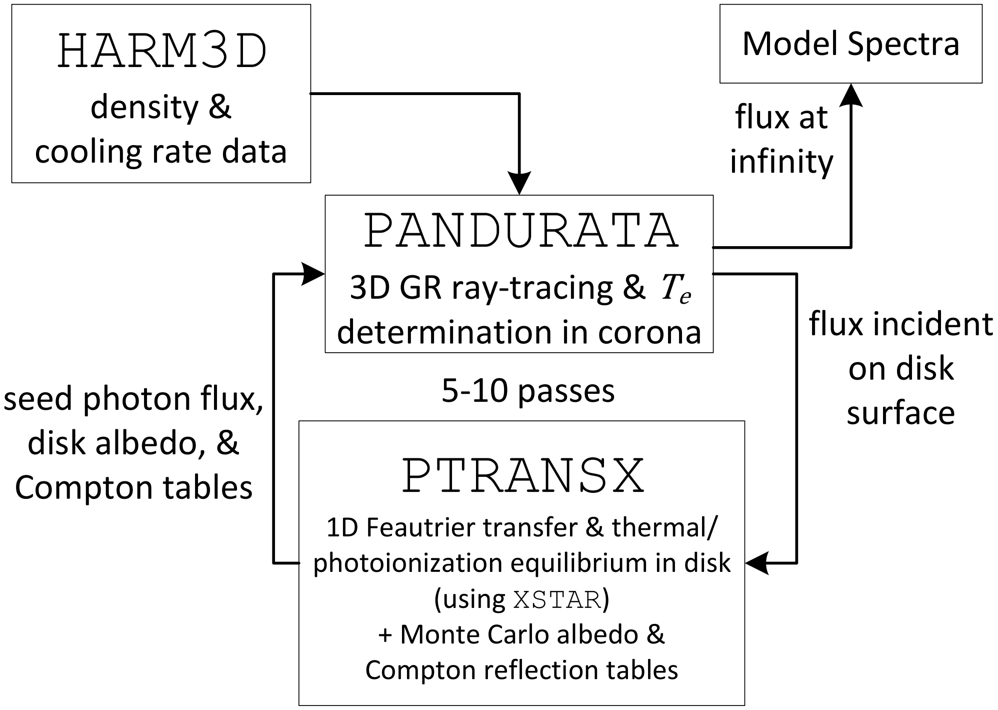

Figure 3.1: A schematic overview of the general procedure.

emission are transported to a distant observer in order to construct the complete predicted spectrum. The overall scheme is summarized in Figure 3.1.

3.1.1 Simulation Data — HARM3D

The density (ρ or n_e) and cooling rate ($\mathcal{L}$) data are from one snapshot of a HARM3D simulation, taken at a time when the disk is in a statistically steady state. HARM3D is a three-dimensional, intrinsically conservative General Relativistic Magnetohydrodynamic (GRMHD) code, with a cooling function designed to produce a geometrically thin disk. HARM3D solves a modified stress-energy conservation equation: in gravitationally-bound gas above a target temperature T_*, the excess heat is radiated away on an orbital timescale; T_* is chosen so as to achieve a target aspect ratio (Noble, Krolik, and Hawley, 2009). The specific simulation we use, "ThinHR" (Noble et al., 2011), has an aspect ratio $H_{\rm dens}/r = 0.06$ (where $H_{\rm dens}$ is the density-weighted scale height), and is still one of the best-resolved GRMHD disk simulations ever carried out (Hawley et al., 2013).

Translating the simulation data from "code units" to physical (cgs) units requires specification of the central black hole mass M, which sets the length and time scales ($1M = (M/M_\odot) \cdot 1.5 \times 10^5$ cm $= (M/M_\odot) \cdot 4.9 \times 10^{-6}$ s), and the accretion rate (in Eddington units) $\dot{m}$, which sets the scale for the density and cooling rate through (Schnittman, Krolik, and Noble, 2013):

$$\rho_{\rm cgs} = \rho_{\rm code} \frac{4\pi c^2}{\kappa G M} \frac{\dot{m}/\eta}{\dot{M}_{\rm code}}, \tag{3.1}$$

$$\mathcal{L}_{\rm cgs} = \mathcal{L}_{\rm code} \frac{4\pi c^7}{\kappa G^2 M^2} \frac{\dot{m}/\eta}{\dot{M}_{\rm code}}, \tag{3.2}$$

where $\kappa = 0.4$ cm^2 g^{-1} is the electron scattering opacity and $\eta = 0.061$ (> 0.057, the Novikov and Thorne (1973) value) is the radiative efficiency found in that simulation (Noble et al., 2011). Below, we consider a $10 M_\odot$ central black hole at four accretion rates, $\dot{m} = 0.01$, 0.03, 0.1, and 0.3.

With a known density structure (and a known spacetime geometry), surfaces of constant optical depth can be defined by integrating the electron scattering opacity along arcs of constant (r, ϕ), starting from the poles and continuing until the desired optical depth is reached. With the disk lying in the $x - y$ plane, the collection of points $\Theta(r, \phi)$ which satisfy

$$\int_0^{\Theta(r,\phi)} \sigma_T n_e \sqrt{g_{\theta\theta}} d\theta = \tau \text{ or } \int_{\Theta(r,\phi)}^{\pi} \sigma_T n_e \sqrt{g_{\theta\theta}} d\theta = \tau \tag{3.3}$$

(where θ is the polar angle) defines the (upper and lower) surfaces of constant optical depth for the given value of τ. The natural choice of surfaces with which to divide the disk body from the corona are the $\tau = 1$ surfaces, which we call the disk photospheres and label $\Theta_{\rm top}$ and $\Theta_{\rm bot}$. At any given (r, ϕ), the region between these surfaces—if they exist—is the disk body; everywhere else is the corona. Which τ value to use for dividing the disk and corona is somewhat arbitrary. For our purposes, a division is needed such that the only significant cooling process in the corona is inverse Compton (IC) scattering, while all atomic processes (such as Fe Kα production) occur within the disk. Because the maximum local ratio of free-free power to net IC power we compute *post hoc* in the corona is $\lesssim 4\%$ (just outside $\tau = 1$), and we find significant Fe Kα production limited typically to $\tau > 1.5$, the $\tau = 1$ surface is a satisfactory choice for the photosphere. Figure 3.2 shows a cross section of HARM3D density and cooling data, scaled to $10M_\odot$ and $\dot{m} = 0.01$, with several surfaces of constant optical depth overlaid.

3.1.2 Coronal Radiation Field — PANDURATA

For the initial pass, we assume that the total cooling at one (r, ϕ) arc within the disk body is radiated thermally at its photospheres. That is, at any (r, ϕ) for which the $\tau = 1$ surfaces exist, the flux outward at both $\Theta_{\rm top}$ and $\Theta_{\rm bot}$ is described as a hardened blackbody with effective temperature

$$\int_{\Theta_{\rm top}}^{\Theta_{\rm bot}} \mathcal{L}\sqrt{g_{\theta\theta}}\,d\theta = 2\sigma T_{\rm eff}^4. \tag{3.4}$$

These thermal seed photons are ray-traced through the corona by the Monte Carlo radiation transport and local temperature balance code PANDURATA. For all subsequent passes, PANDURATA uses PTRANSX's output seed photon spectra instead of the hardened blackbody. PANDURATA takes as input the density and cooling maps from HARM3D, as well as the seed photon emission at the disk photosphere, and outputs: (1) an electron temperature map of the corona; (2) the spectrum as seen by distant observers; and (3) the spectral shape and strength of the flux incident upon the (upper and lower) disk photospheres at each (r, ϕ).

The operation of PANDURATA's original version is described in detail, including series of tests to demonstrate the algorithm's validity, in Schnittman and Krolik (2013). In brief, the code simulates the trajectories and scattering of seed photons in the corona while solving for the electron temperature at each point in the corona by setting the net inverse Compton power equal to HARM3D's local cooling rate. Several modifications to PANDURATA were made for its use in this project. First, photon packet scattering off of single electrons was

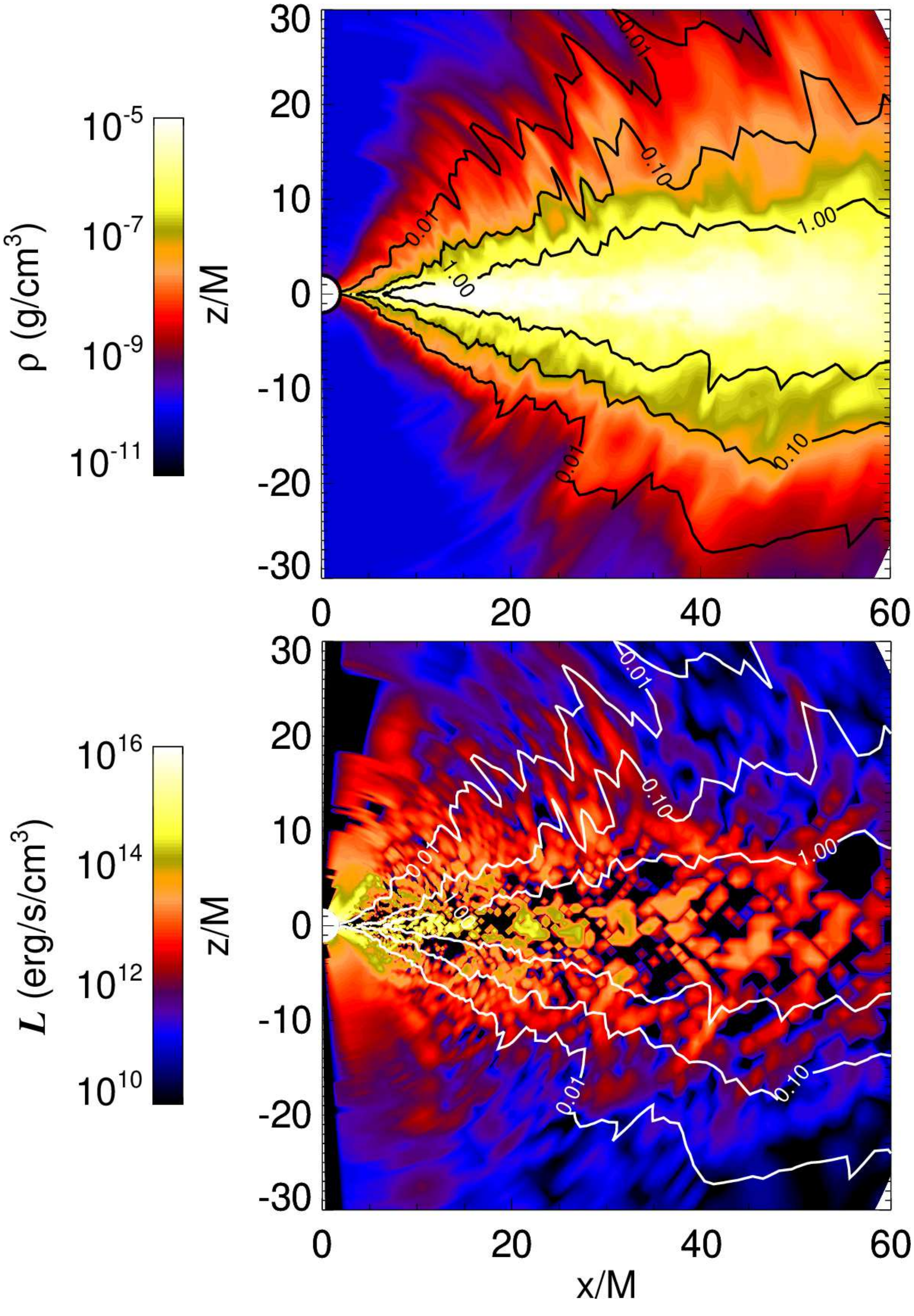

Figure 3.2: The $x - z$ slice of the HARM3D simulation data, scaled to $M = 10M_\odot$, $\dot{m} = 0.01$, with three surfaces of constant optical depth overlaid. Note the great difference (and rapid change) in density between the disk body and the corona (upper panel). The lower panel shows the local instantaneous cooling rate—not all fluid elements are radiatively cooling at each time step [see Schnittman, Krolik, and Noble (2013) for a more extensive discussion of the cooling function]. There is significant cooling in the corona, even where the density is very low.

replaced by an *ensemble* approach—when a photon packet scatters in the corona, the photon packet's spectrum is redistributed according to an angle-averaged energy redistribution function described below (see section 3.1.3.2); its new direction, however, is determined as if it were a single photon scattering off a single electron whose particular velocity was selected from the Maxwell-Jüttner distribution. Second, the coronal volume is divided into sectors—a coarser grouping, compared to the underlying simulation grid, of ~ 100 contiguous grid-cells each—with the interior of each sector treated as having a single temperature; net IC power is assessed for the sector as a whole, and a sector's temperature is adjusted by way of a Newton-Raphson method until its net IC power equals its total internal cooling rate. These two changes to PANDURATA [compared to its description in Schnittman and Krolik (2013)] allow faster determination of the coronal temperature map, now necessary since PANDURATA must re-determine the temperature map each pass. We have verified that modified PANDURATA produces the same output spectrum as unmodified PANDURATA. The final modification, however, is more substantive: photon packets which strike the disk surface are subject to absorption and Compton recoil according to albedo and redistribution tables computed with PTRANSX output, using a procedure described in section 3.1.4. An example cross section of an electron temperature map so computed is shown in Figure 3.3.

The end result is a complete description of the electron temperature and radiation field everywhere in the corona—including the flux irradiating the disk surface—that is consistent with the density and cooling structure of the GRMHD simulation as well as the temperature and ionization structure of the disk body.

3.1.3 Disk Reprocessing — PTRANSX

3.1.3.1 Defining the Problem

At each (r, ϕ), the region between $\Theta_{\rm top}$ and $\Theta_{\rm bot}$ constitutes a column of the disk body. Its vertical density and cooling rate profiles are known from the HARM3D simulation data, and

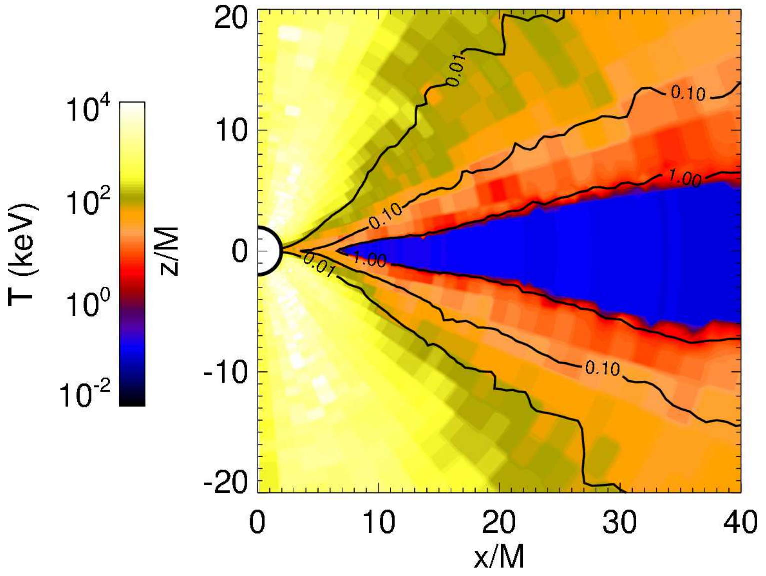

Figure 3.3: The electron temperature map produced by PANDURATA for the same slice of data shown in Figure 3.2 ($M = 10M_\odot$, $\dot{m} = 0.01$). Note that within the disk body (between the $\tau = 1$ surfaces) the electron temperature is shown as the constant value $T_{\rm eff}$; PANDURATA does not determine the electron temperature within the disk body. The visible "blockiness" is due to our division of the coronal volume into sectors.

the fluxes incident upon its upper and lower surfaces are computed by PANDURATA. In addition, some choice of elemental abundances is required. The chief assumption is that such a column can be treated as a finite, plane-parallel slab independent from its neighbors. The problem is to find, for each slab, a description of the radiation field and ionization balance at all vertical points that is energy-conserving, in photoionization equilibrium, consistent with the boundary conditions and structure provided, and which includes as many of the relevant physical processes as possible. Photoionization equilibrium is a reasonable assumption: for the densities and temperatures typical of the accretion disks we consider, the recombination timescale is short, $\sim 10^{-7}$ s (for highly-ionized Fe), compared to the disk's dynamical timescale, $\sim 10^{-3}$ s. We accomplish this with an extended version of the code PTRANSX introduced in Kinch et al. (2016); this version includes several major improvements, particularly in the treatment of Compton scattering but in other areas as well. Its operation is described below.

3.1.3.2 The Transfer Solution

We solve the radiative transfer equation in plane-parallel geometry, including all relevant atomic processes and Compton scattering:

$$\mu \frac{dI_{\mu\varepsilon}}{dz} = -\alpha_\varepsilon I_{\mu\varepsilon} + j_\varepsilon - n_e \sigma_\varepsilon I_{\mu\varepsilon} + n_e \int_{-1}^{1} \int_{0}^{\infty} d\mu' d\varepsilon' \sigma_{\varepsilon'} R(\mu', \varepsilon'; \mu, \varepsilon) I_{\mu'\varepsilon'}. \tag{3.5}$$

We employ the Feautrier method (Mihalas, 1978), which requires only that the redistribution function R has forward-backward symmetry, i.e., that $R(\mu', \varepsilon'; \mu, \varepsilon)$ is unchanged under

$$\Delta\theta = \cos^{-1}\left[\mu'\mu + \sqrt{\left(1-\mu'^2\right)\left(1-\mu^2\right)}\right] \to \Delta\theta \pm \pi. \tag{3.6}$$

R is a measure of the probability that photons with angle-energy (μ', ε') will scatter to angle-energy (μ, ε). With a specification of boundary conditions—$I_{\mu\varepsilon}$ *inward* at the upper and lower surfaces (the incident intensity from PANDURATA)—we solve a discretized version of the above transfer equation *directly* via a forward-backward recursive sweep (Mihalas, 1985).

Our treatment of Compton scattering is expressed by our choice of R. Though we have gone to great lengths to describe Compton scattering as accurately as possible, we are required by the Feautrier method to make the following approximation:

$$R(\mu', \varepsilon'; \mu, \varepsilon) = \frac{1 + \left[\mu'\mu + \sqrt{\left(1-\mu'^2\right)\left(1-\mu^2\right)}\right]^2}{2} \mathcal{R}(\varepsilon', \varepsilon). \tag{3.7}$$

We replace the angular dependence of a more accurate redistribution function with the dipole phase function of Thomson scattering, which has the required forward-backward symmetry. The Klein-Nishina cross section *does not* have this symmetry—forward scattering is preferred to backward scattering, and significantly so at energies approaching and beyond $m_e c^2$. For the energies we are most concerned with ($\lesssim$ 50 keV), however, that preference is modest. $\mathcal{R}$ is the angle-average of the full Compton redistribution function (itself a function of the local electron temperature) computed directly with an independent Monte Carlo calculation using relativistic dynamics, the Klein-Nishina cross section, and the Maxwell-Jüttner velocity distribution. The same $\mathcal{R}$ is used in the ensemble scattering calculation of PANDURATA described above.

In order to demonstrate the correctness of our transfer solution in general, and of our treatment of Compton scattering in particular, we compare sample results between a PTRANSX solution and those from a completely independent Monte Carlo transfer code. A straightforward Monte Carlo implementation was supplied with the vertical structure for the density, temperature, emissivity, and absorption opacity from a PTRANSX slab—though, for ease of comparison, we consider here *only* the Fe Kα line emissivity. The independent Monte Carlo code does *not* use the angle-averaged Compton redistribution function described above; rather, it treats Compton scattering directly and with the appropriate angular dependence. Nevertheless, as Figure 3.4 indicates, the seed photon flux so computed agrees with the PTRANSX result exceedingly well. Note that the slight over-prediction of upscattering relative to the Monte Carlo approach is due to the logarithmically-spaced energy grid in PTRANSX. Even for a flat probability distribution, it is more likely for a photon to scatter to bin $i + 1$ rather than bin $i - 1$ if the bin width increases logarithmically. Increasing the number of grid-points alleviates the problem, though the discrepancy as it stands is well below the intrinsic error of any real X-ray detector.

3.1.3.3 Equilibrium-Finding Procedure

We make use of subroutines of the photoionization code XSTAR (Kallman and Bautista, 2001) in order to compute the local ionization balance—and consequent emissivity and absorption opacity—of gas at a fixed temperature and density, immersed in a known radiation field, in photoionization equilibrium.

At each (r, ϕ) sampled, the disk body is divided into some number of vertical cells (typically a few dozen, see section 3.1.6 below). For the i^{th} cell, the net energy balance y_i is defined as the difference between the net energy flux *out* of the cell and the total cooling

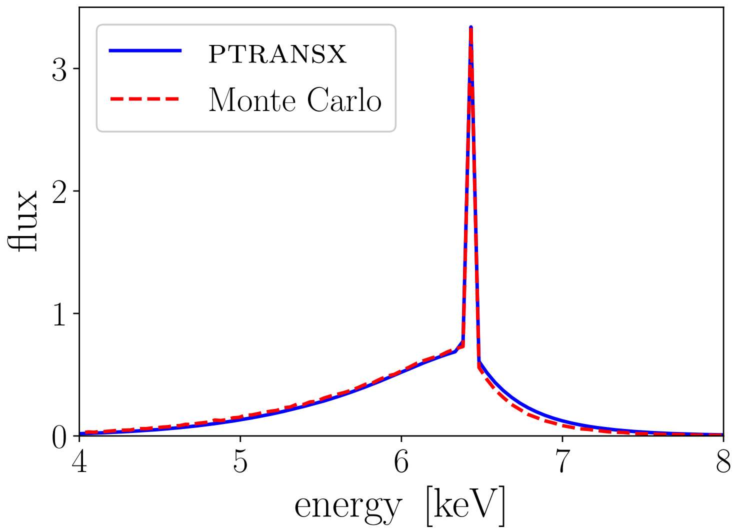

Figure 3.4: Comparison of example seed photon spectra (Fe Kα only) computed using both PTRANSX and an independent Monte Carlo code. The profiles are normalized to unity.

within that cell. That is:

$$y_i = \int_0^\infty d\varepsilon \left(F_{i,\varepsilon}^{\rm top} - F_{i,\varepsilon}^{\rm bot} \right) - \mathcal{L}_i (\Delta z)_i. \tag{3.8}$$

The collection of these values for all cells in the given vertical column forms the vector $\mathbf{y}$; in total energy balance, $\mathbf{y} = \mathbf{0}$. The vector $\mathbf{y}$ is directly computable from a complete description of the radiation field, the result of solving the transfer equation. All heating and cooling processes which are represented in either the emissivity, the absorption opacity, or the redistribution function—that is, bremsstrahlung, all atomic processes (photoionization, recombination, and line emission) and (inverse) Compton scattering—have their effects on the energy balance included in the expression for $\mathbf{y}$. Knowledge of $I_{\mu\varepsilon}$ in each cell constitutes a full description of the radiation field; similar to $\mathbf{y}$, we call such a collection $\mathbf{I}$. Similarly, the collection of energy-dependent absorption opacities and emissivities, $(\alpha_\varepsilon, j_\varepsilon)$, in all cells is denoted $\mathbf{S}$. Finally, the cell-by-cell list of temperatures is $\mathbf{T}$.

The first step in the procedure is to zero out all emission and absorption and perform a transfer solution with only *Thomson* scattering. This yields a guess at the radiation field in each cell. For each cell independently, we supply to the relevant XSTAR subroutines the radiation field, density, temperature, and elemental abundances; XSTAR returns the photoionization equilibrium values for the ionization balance, emissivity (line and continuum), and absorption opacity. We do not use XSTAR's built-in transfer apparatus. As described in the previous chapter, we ignore the resonant absorption of line photons on the basis of a *post hoc* analysis of their escape probabilities, computed by XSTAR—due to the extremely high local turbulent velocity of the disk gas, these are all very near to unity. For this first iteration, we use XSTAR's ability to find a local energy-conserving temperature while performing its photoionization equilibrium calculation. In addition to the heating and cooling rates XSTAR considers [see Kallman and Bautista (2001) for details], we also supply the HARM3D simulation local cooling rate as an exogenous heating term. In subsequent iterations, we supply a local temperature according to the procedure described next. We now have a first guess at the absorption opacity, emissivity, and temperature in every cell. A second transfer solution performed with this $\mathbf{S}_0$ and $\mathbf{T}_0$ yields $\mathbf{I}_0$ and the corresponding $\mathbf{y}_0$.

We imagine our transfer/XSTAR scheme as a vector function: XSTAR requires $\mathbf{I}$ and $\mathbf{T}$ to determine the photoionization equilibrium $\mathbf{S}$, which via our transfer solution produces (a new) $\mathbf{I}$ and thus $\mathbf{y}$. That is, $F(\mathbf{I}, \mathbf{T}) = \mathbf{y}$. We seek a procedure by which, for a given $\mathbf{I}$, we can find the energy-conserving temperature structure $\mathbf{T}^*$, such that $F(\mathbf{I}, \mathbf{T}^*) = \mathbf{0}$.

To do so, we employ the multidimensional Newton-Raphson algorithm. Starting with $\mathbf{T}_0$ and a corresponding $\mathbf{y}_0$, we perform a finite difference estimation of a Jacobian of the form

$$J_{ij} = \frac{\partial y_i}{\partial T_j}. \tag{3.9}$$

The new guess at the energy-conserving temperature is

$$\mathbf{T} = \mathbf{T}_0 - \mathrm{J}^{-1}\mathbf{y}_0. \tag{3.10}$$

From this new temperature structure we determine the new $\mathbf{S}$ with XSTAR, and with that perform a transfer solution to find the new $\mathbf{y}$. We repeat the procedure until all elements of

$\mathbf{y}$ are sufficiently close to zero, i.e., for all i, the two terms on the right-hand side of equation 3.8 differ by less than 1%. Thus we find $\mathbf{T}^*$. As a practical matter, it occasionally happens that elements in the new temperature vector are not reasonable (for example, negative temperatures); this typically occurs in situations where there are relatively sharp changes in density or cooling rate. In these cases, we require an additional step before the next iteration: these "problem" cells are isolated and their individual y roots found by varying only *their own* T using the secant or bisection methods; these new T values replace their nonsensical counterparts in $\mathbf{T}$, and iteration resumes. Following Nayakshin, Kazanas, and Kallman (2000), we estimate that, for the disk temperatures we find in this paper, the maximum Thomson depth over which heat conduction dominates is $\sim 10^{-4}$; because this is much smaller than our cell sizes, it is safe to ignore heat conduction even for sharp cell-to-cell changes in the cooling rate.

It is important to stress that at no step of the procedure described above is the radiation field supplied to XSTAR altered. After the energy-conserving temperature structure $\mathbf{T}^*$ is found, and the absorption opacities and emissivities everywhere re-computed with it, one last transfer solution gives us a new and by construction energy-conserving radiation field. In fact, the full procedure can be thought of as a function which takes some radiation field $\mathbf{I}$ as input and returns a new radiation field $\mathbf{I}^*$—this new radiation field is energy-conserving, but the gas is in photoionization equilibrium with the *previous* radiation field $\mathbf{I}$. Naturally, then, we just repeat the entire process until $\mathbf{I}^* = \mathbf{I}$. Thus we accomplish our goal: we have a complete description of a radiation field for which energy is conserved everywhere and with which the gas is at all points in photoionization equilibrium.

In cases where the disk body is many Thomson depths in thickness, it becomes impractical (mainly due to memory constraints) to treat it as a single finite slab extending from one photosphere to the other. Rather, we are forced to set an interior boundary condition some number of Thomson depths inward from the photosphere (we choose 10, see section 3.1.6 for details); the natural choice is to assume a blackbody flux *into* the computation volume from the otherwise excluded disk interior. This is similar to the interior boundary condition used by García and Kallman (2010) [i.e., the radiative diffusion approximation (Rybicki and Lightman, 1986)], but we do not set the disk temperature in advance according to Shakura and Sunyaev (1973). Like the temperature within the computation volume, this boundary temperature is not assumed *a priori*. Rather, it is found in the exact same way as part of the same formalism. At the inner boundary, we define an additional element of $\mathbf{T}$, $T^{\rm bound}$, and an additional element of $\mathbf{y}$,

$$y^{\rm bound} = \pm \int_0^\infty d\varepsilon F_\varepsilon^{\rm bound} - \frac{1}{2}\left(\text{total } \mathcal{L} \text{ in disk interior}\right), \tag{3.11}$$

with the upper sign corresponding to the upper disk layers and the lower sign to the lower disk. Defined so, $y^{\rm bound} = 0$ (at both upper and lower interior boundaries) indicates that the net flux into the computation volume is equal to the total cooling rate *excluded* by the computation volume—like all elements of $\mathbf{y} = \mathbf{0}$, it is a statement of energy conservation. With some reasonable starting guess for $T^{\rm bound}$ (e.g., $2\sigma T^4 =$ total $\mathcal{L}$ in disk interior), our multidimensional Newton-Raphson method will find the energy-conserving interior boundary temperature as part of its overall solution.

3.1.4 The Reprocessed Spectrum

Next we compute from the output of PTRANSX a *new* seed photon spectrum at all (r, ϕ) points on the disk surface. This is done simply by performing one last radiative transfer solution but with the incident intensity set to zero—the seed photon spectrum includes only those photons *emitted* by the gas in the disk, not those which are reflected by it (see section 3.1.5 below). In Figure 3.5 we compare the initially assumed hardened blackbody seed photon spectrum at one point on the disk surface to the PTRANSX output seed photon spectrum. The PTRANSX spectrum is broader, higher at all energies, has a prominent H-like Fe Kα emission feature at 7 keV, and a small K-edge absorption dip near 9 keV. Though the PTRANSX spectrum is slightly harder, there is still virtually zero emission above 10

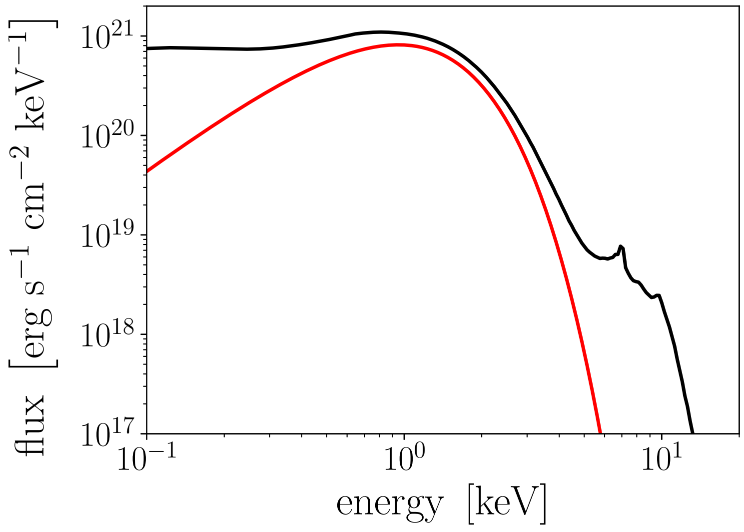

Figure 3.5: Comparison between the initial assumed seed photon spectrum (red curve) and the converged PTRANSX output spectrum (black curve), at $r = 10M$, $\phi = 0$, for $\dot{m} = 0.03$.

keV. This pattern generally holds (though with a variable dominant Fe ionization state) for all accretion rates we consider, and at all radii except for where the disk's total Thomson thickness is $\lesssim 1$—there the PTRANSX seed photon spectrum is just optically thin free-free emission. For the example point shown, the integrated power of the PTRANSX seed photons is $\sim 50\%$ greater than that of the hardened blackbody—this is because the PTRANSX seed photons must carry additional energy from Compton and photoionization heating of the disk due to its irradiation by the corona. PANDURATA then ray-traces these new seed photon packets from the disk surface with a limb-darkened angular distribution consistent with PTRANSX's transfer solution. In the initial PANDURATA solution, however, photon packets which strike the disk surface are simply reflected; for this second pass, the absorption and energy redistribution of photons impinging the disk surface is informed by the PTRANSX output.

When a photon packet with energy-dependent intensity I_ε intersects the disk surface, it is transformed into a reflected photon packet with intensity $I_\varepsilon^{\rm refl}$ according to

$$I_\varepsilon^{\rm refl}/\varepsilon = \int_0^\infty d\varepsilon' f\left(\varepsilon'\right) G\left(\varepsilon, \varepsilon'\right) I_{\varepsilon'}/\varepsilon'. \tag{3.12}$$

The albedo f is the fraction of incident photons at a specific energy which are reflected, i.e., not absorbed by the disk, regardless of their final, outgoing energy. G is a normalized description of the redistribution of photons from energy ε' at incidence to energy ε upon reflection. Both f and G are functions of position on the disk surface and of the photon packet's incident angle with respect to the local disk normal. These functions are tabulated using a separate, auxiliary Monte Carlo transport code. This additional code injects large numbers of photons at each energy and incident angle from the PTRANSX grids, for each point on the disk surface, using the PTRANSX output opacity and temperature structure; it records for each energy and angle the fraction which are reflected (the albedo f) and the energy-distribution of the reflected photons (G in equation 3.12). The Compton scattering calculation therein is performed according to standard relativistic dynamics.

From this same Monte Carlo code, we have found that the distribution in angle of the outgoing photons is a very nearly linear function of μ with respect to the local disk normal [i.e., limb-darkening, but not exactly the pure scattering atmosphere expression of Chandrasekhar (1960)]; we therefore select the initial trajectory of the reflected photon packets according to this distribution. Small portions of the disk are only marginally optically thick, and in these regions there can be a significant *transmitted* fraction. Ideally, the transmitted fraction would spawn a new photon packet in addition to the reflected packet. This is, however, not computationally feasible at this time, so instead we include the transmitted fraction in the reflected photon packet. To the extent that the upper and lower halves of the computation volume are similar, this will ultimately produce the same result. For the cases considered here, transmission through the disk is negligible for $\gtrsim 99\%$ of the disk area. Figure 3.6 shows the energy-dependent albedo at several radii for $\dot{m} = 0.03$; Figure 3.7 shows the albedo at $r = 10M$ for the four sample accretion rates. The most dramatic feature in both is, not surprisingly, the highly-ionized Fe K-edge at 8–10 keV: its depth increases at larger radii (as cooler, less-ionized gas has a higher fraction of unstripped Fe atoms available for absorption) and with decreasing $\dot{m}$ (for the same reason; see equations 3.1 and 3.2).

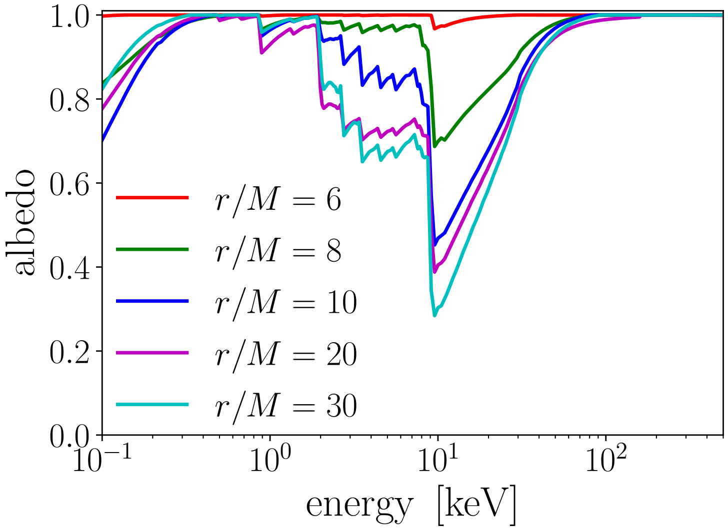

Figure 3.6: The energy-dependent albedo (including transmitted fraction) at the disk surface at several radii (all $\phi = 0$) for $\dot{m} = 0.03$.

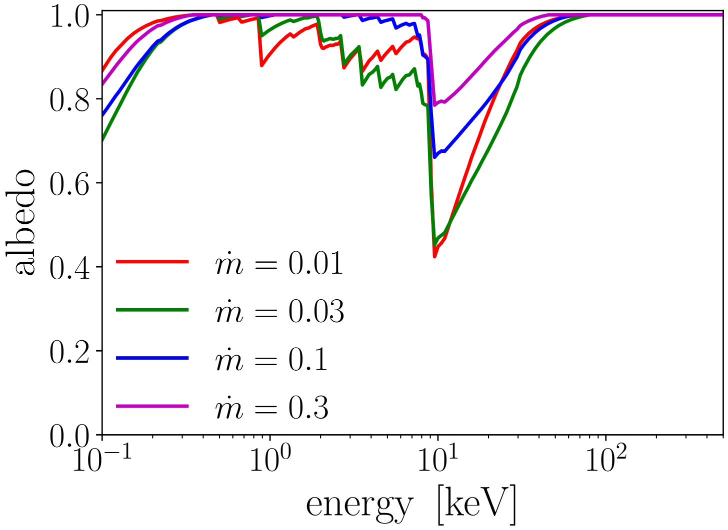

Figure 3.7: The energy-dependent albedo (including transmitted fraction) at the disk surface at $r = 10M$, $\phi = 0$, for several values of $\dot{m}$.

3.1.5 PTRANSX and PANDURATA Communication

The revised seed photon packets are the reprocessed emission from the disk, including atomic emission features like the Fe K lines. As PANDURATA transports them through the corona, they experience inverse Compton scattering in addition to all special and general relativistic effects. When they scatter off the disk surface, absorption features like the Fe K-edge are imprinted. A different spectrum of seed photons than that originally assumed affects the efficiency of the IC cooling process in the corona—so we run PANDURATA again, with disk albedo and Compton recoil tables in hand from the last PTRANSX run, and thus determine a new coronal temperature map and radiation field. This PANDURATA run yields a new irradiating flux, and so we run PTRANSX again to obtain new seed photon spectra and albedo tables. The cycle repeats until the X-ray spectrum as seen by the distant observer changes by less than 1% from one pass to the next.

Our method separates *emission* from the disk and *absorption/reflection* by the disk into sequential steps: Fe Kα line photons, for example, are emitted as part of the seed photon flux for a point on the disk surface consistent with the incident flux at that point found from the previous PANDURATA run; likewise, photon packets which strike the disk as they are ray-traced through the corona are subject to absorption according to the disk's opacity found in the preceding PTRANSX run. The same is true for the overall energy balance—the power in the seed photon flux accounts for both the disk's internal dissipation *and* Compton and photoionization heating of the disk's gas consistent with the incident flux from, again, the previous PANDURATA run. By cycling between the two codes until the global radiation field (including the disk incident flux) no longer changes, we ensure *global* energy balance and the self-consistency of our non-simultaneous treatment of absorption and emission.

The final run of PANDURATA yields the desired product: a spectrum as seen by a distant observer—a *prediction*, arrived at through consideration of the relevant physical principles, for what we expect to observe from an accreting stellar-mass black hole, specifying only the *physical* parameters of mass, spin, accretion rate, and elemental abundances.

3.1.6 Numerical Specifics

In describing our technique, we have been intentionally vague concerning any numerical values. While our general approach is applicable to a large volume of the stellar-mass (and even AGN) black hole parameter space, the specific resolutions, samplings, etc., that we use in a real calculation must be tailored to the kind of problem we want to solve—we must balance the desired accuracy and completeness of our prediction with realistic computational constraints. In practice, this requires numerical experimentation: resolutions and samplings start off coarse and are repeatedly refined until the final results (presented in the next section) no longer appear to change.

Here we consider four cases, at $\dot{M}/\dot{M}_{\rm Edd} = \dot{m} = 0.01,\ 0.03,\ 0.1,$ and 0.3; per equations 3.1 and 3.2 in section 3.1.1, the choice of $\dot{m}$ translates HARM3D data snapshots into physical (cgs) values for the density and cooling rate. For each, the central black hole mass is $10M_\odot$, the spin is zero, and the abundances are solar [Grevesse, Noels, and Sauval (1996) values]. When running PANDURATA, the coronal volume is divided into $\sim 24,000$ sectors (the exact number varies with the location of the disk photosphere, and therefore decreases with increasing accretion rate) of $\Delta\theta = \pi/36$ and $\Delta\phi = \pi/32$ radians each, with a logarithmically increasing radial extent such that $\Delta r/r = 0.062$, starting at the event horizon, $r = 2M$. For the snapshots we used, smaller sectors than these do not result in an appreciable change to the shape or strength of the X-ray flux incident upon the disk surface or seen by the distant observer—doubling the number of sectors results in less than a 1% change to the observable spectrum in the 1–30 keV range. The majority of these sectors lie wholly in the corona, but those which overlap with the disk have only their coronal part included in PANDURATA's calculation. When running PTRANSX, we sample $\sim$ 300–500 (r, ϕ) points per case (with more for the higher accretion rate cases as the inner edge of the disk photosphere extends further inward). These are chosen uniformly in azimuth (at 8 ϕ angles) and logarithmically in r such that $\Delta r/r = 0.062$. For each (r, ϕ) slab, the vertical cells are spaced semi-logarithmically in Thomson depth τ, such that the increase in Thomson depth *into* the disk over one cell is $\Delta\tau/\tau = 0.25$, but with $\Delta\tau$ limited to a maximum of 0.4; the grid is laid out so that the cells follow this semi-logarithmic spacing *into* the disk starting from both upper and lower photospheres, meeting at the midplane. Slabs with a total Thomson depth of 20 or greater are cleaved into an upper and lower computation volume as described above, with the interior boundary always placed at a Thomson depth of 10 as measured from the relevant photosphere. The number of vertical cells used varies from 6 at the extreme inner edge of the disk to 50 at its thickest extent before the approximation just described is employed; the "cleaved" slabs are separated into upper and lower volumes of 27 cells each. Neither finer spacing in optical depth nor a deeper interior boundary result in an appreciable change to the output seed photon spectrum.

The angle with respect to $\hat{z}$, the cosine of which is the μ in our transfer equation, is discretized such that 16 bins uniformly spaced in μ cover the range -1 to 1. This is more than sufficient to capture the angular dependence of the radiation field, which is nearly isotropic for most of the disk body. Our energy grid is more complex. For the purposes of determining the temperature structure and photoionization balance via multidimensional Newton-Raphson, we span the range from 1 eV to 10^8 eV with a coarse 161-point grid whose energy resolution is $\Delta\varepsilon/\varepsilon = 0.122$. The computational cost of the transfer solution scales poorly with the number of energy bins (cubically) and our multidimensional Newton-Raphson scheme requires the transfer solution to be performed *many* times—typically 20–80 iterations per slab, depending on its thickness and ionization parameter. Yet because the bulk of the power in the radiation field is in the continuum, and the broadband continuum can be well-represented on such a coarse grid, increasing the energy resolution further results in little change in the equilibrium temperature structure. Thus the approach we take is to use a coarse grid to find the equilibrium temperature structure, then re-bin to a finer 801-point grid ($\Delta\varepsilon/\varepsilon = 0.0233$) on which we perform *one* last transfer solution at a resolution high enough so that line features are clearly distinguishable; we use this same procedure (and identical energy grids) with PANDURATA as well.

We take 1% as sufficient for all convergence tests. That is, "energy conservation" (for both PTRANSX and PANDURATA) means (energy in) = (energy out) is satisfied in all cells/sectors (and globally) to within at most 1%. The majority are better converged by the time this is achieved—typically, $\sim 90\%$ of cells/sectors conserve energy within 0.1%. For determining if $\mathbf{I}^* = \mathbf{I}$, we compute the first several energy moments of the mean photon intensity in the range 1–30 keV (the region of the outgoing spectrum we are most concerned with) at each cell; when the greatest fractional difference between any of these values and its counterpart in the previous iteration has dropped below 1%, we consider the radiation field to have converged. Finally, the cycling between PTRANSX and PANDURATA ceases when the greatest difference between the spectrum as seen by a distant observer (at any inclination or energy in the range 1–30 keV) from one iteration to the next differs by, again, at most 1%—this takes, for the cases we discuss in this paper, between 5–10 passes.

3.2 Results

3.2.1 Continuum

The key results of our calculation are predicted X-ray spectra as seen by a distant observer. Figure 3.8 shows the broadband spectral luminosity for the four accretion rate cases we consider. Because the dynamical timescale for stellar-mass black holes is many times smaller than the integration time for any reasonable observation of them, we present all distant observer spectra as azimuthally-averaged. Particularly for the $\dot{m} \geq 0.03$ cases, these broadband spectra reproduce the forms inferred by phenomenological fitting of real black hole X-ray binary data in the steep power-law state (Remillard and McClintock, 2006): there is a quasi-thermal bump at 1–3 keV that is extended to high energy as a steep power-law that hardens slightly above ~ 10 keV. The photon index Γ computed over the 5–30 keV band ranges from 2.7 for $\dot{m} = 0.01$ to 4.5 for $\dot{m} = 0.3$, comparable to the observed values for black hole binaries in the thermal and steep power-law states, $\Gamma = 2.1$–4.8 (McClintock and Remillard, 2006).

The thermal bump is not too surprising, and its existence and temperature follow from having a dense, optically thick disk body with a sub-Eddington accretion rate around a $\sim 10 M_{\odot}$ black hole. On the other hand, the prediction of a steep power-law component, due to the IC upscattering of thermal seed photons in a hot corona, represents a triumph for the theory of MHD accretion disks. No coronal emission at all is predicted by the models of Shakura and Sunyaev (1973) and Novikov and Thorne (1973). We find here that a purely physical calculation, starting from a GRMHD simulation of black hole accretion, gives rise *naturally* to the approximate spectral shape observed for black hole binaries in the steep power-law state, with no phenomenological descriptions of the accretion geometry (of disk or corona) or parameter-tweaking required. This result was first shown by Schnittman, Krolik, and Noble (2013), also using PANDURATA analysis of HARM3D simulations. With our more careful treatment of the seed photon spectrum and the inclusion of disk absorption enabled by coupling to PTRANSX, we predict slightly softer spectra than those reported in Schnittman, Krolik, and Noble (2013). Curiously, using simulations nominally similar to ours (GRMHD thin disk simulations with prescribed cooling functions) and a post-processing procedure calculating the Comptonization of initially thermal photons, Narayan et al. (2016) were unable to find any high-energy extension of the thermal component.

The spectra in Figure 3.8 have power-law tails which extend to very high energies. In Figure 3.9, we show (for $\dot{m} = 0.03$) the distribution of IC power generation in the corona as a function of the electron temperature. The photons which make up the observable spectrum were upscattered by electrons with a wide range of temperature, 1–1000 keV, but the distribution is distinctly bimodal with peaks at 10–30 keV and 400–800 keV. While the majority of the cooling is due to electrons with temperatures less than 100 keV, approximately 20% of the coronal power is radiated from electrons with temperatures in excess of 400 keV. The other three accretion rate cases also have similarly bimodal distributions. It is evident from this figure that a single-temperature Comptonization model of the corona cannot adequately describe our results. Similarly, a single Compton y-parameter does not adequately describe

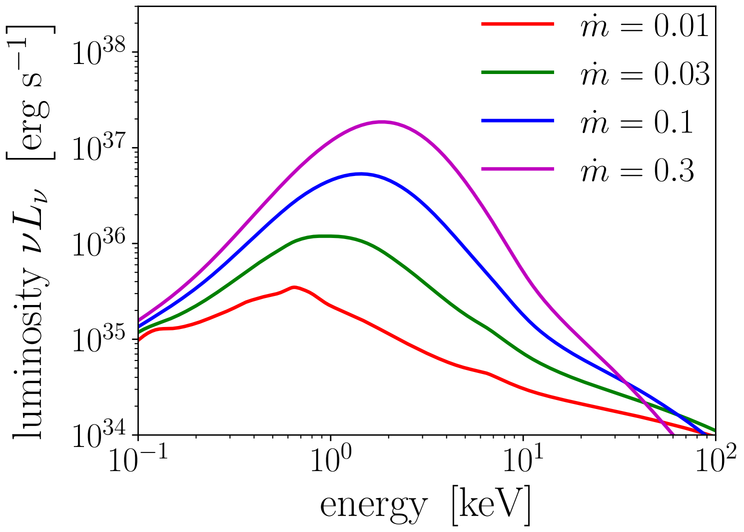

Figure 3.8: The spectral luminosity at four accretion rates, each with a central black hole mass of $10 M_\odot$ and $a = 0$. Note that the spectra soften as the accretion rate increases. Although not easily visible in this representation, the equivalent width of the Fe Kα feature diminishes with increasing $\dot{m}$.

coronal scattering. A thermal 1 keV seed photon which escapes to the distant observer will typically undergo 3–7 scatters. If it scatters through electrons at $T_e = 20$ keV (roughly the location of the first peak in Figure 3.9), then $y \approx 0.7$; however, if it scatters through electrons at $T_e = 500$ keV (roughly the location of the second, smaller peak), $y \approx 70$. From Figure 3.3 (which, while shown for $\dot{m} = 0.01$, is qualitatively similar to the $\dot{m} = 0.03$ case), we see that there is a clear polar angle-dependency to the coronal temperature—hotter regions are those more inclined relative to the midplane. We see from this figure as well that a single-temperature description is unsatisfactory: a thermal disk photon will likely pass through several layers of gas with very different temperatures, scattering in any or all of them.

We do not see clear evidence for Compton bumps in the spectra of Figure 3.8. These bumps can be seen most clearly when the disk is absorptive across the soft X-ray band and up through the Fe K-edge, and when the underlying continuum is relatively hard so that there are plentiful photons above ~ 10 keV to scatter. Here neither is the case. The result is that the numerous photons with energy below the onset of absorption at the Fe K-edge can

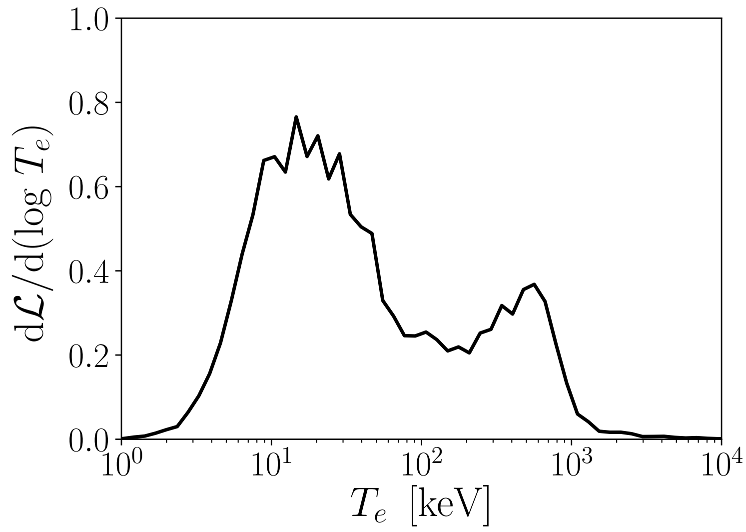

Figure 3.9: The distribution of IC power as a function of electron temperature in the corona for $\dot{m} = 0.03$. The data are normalized to the total cooling in the corona. Note both the broad range in temperature and the distinctly bimodal shape of the distribution.

be upscattered and smooth over the feature. We expect the reflection hump to be visible when we scale these same simulations to AGN masses and temperatures. At that scale, we expect elements other than Fe to produce important spectral features as well.

Figure 3.10 shows the photon index measured in the range 5–30 keV as a function of observer angle for each accretion rate. The power-law slope varies irregularly, but only slightly, with inclination; its range increases with increasing $\dot{m}$. The extent of the top-bottom asymmetry seen in Figure 3.10 (and also in Figure 3.13 below, showing Fe Kα equivalent width in the same fashion) provides a rough indication of the “cosmic variance” expected for these simulations.

It is important to emphasize again (see section 3.1.1) that each accretion rate case we consider is the same underlying simulation snapshot with the density and cooling rate scaled. The simulation used here is most physically realistic for $\dot{m} = 0.1$–0.3; it is not surprising that our results for this range of accretion rates most closely resemble observations. HARM3D is unable to relate disk vertical structure to accretion rate because it has an ad hoc procedure for radiative cooling and does not include radiation forces at all. However, techniques for

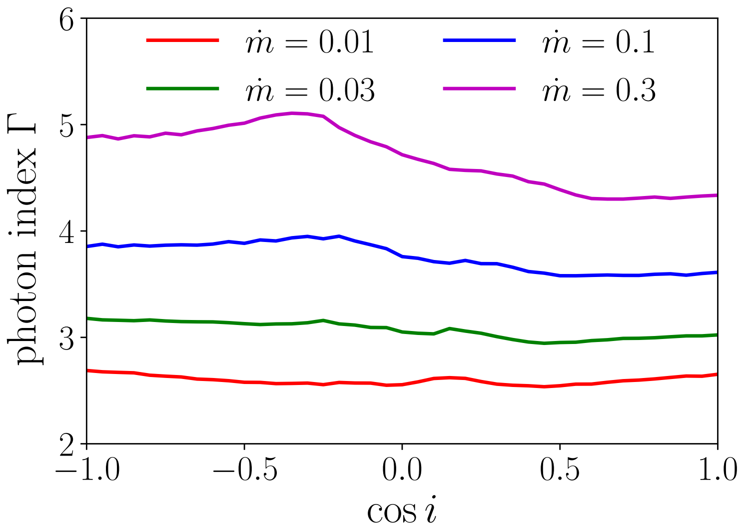

Figure 3.10: The photon index of the predicted spectrum, measured in the range 5–30 keV, as a function of observer angle at four accretion rates.

coupling radiation transport to MHD are rapidly improving (Jiang, Stone, and Davis, 2014; Sądowski et al., 2014). In the future, it will be possible to reapply our method to data from codes of that variety in order to work with a more realistic connection between accretion rate and disk structure.

3.2.2 Fe Kα

To illustrate our predictions of the Fe Kα line profile, we adopt a procedure mimicking a common approach to presenting observational data: we divide the data by a simple prescription for the continuum—in this case, a power-law fit to the region 3–30 keV. Figure 3.11 shows this procedure applied to the $\dot{m} = 0.01$ case at an observer inclination of 25°, for which the fitted power-law has photon index $\Gamma = 2.7$. We reproduce the features expected: a relativistically-broadened Kα emission line near 6.4 keV and a K-edge absorption trough centered roughly at 10 keV. However, the contrast of both features relative to the power-law fit is quite small, only 5–10%. In addition, above 15–20 keV there is a slight hardening of the continuum relative to $\Gamma = 2.7$, the single value that best fits the 3–30 keV continuum slope.

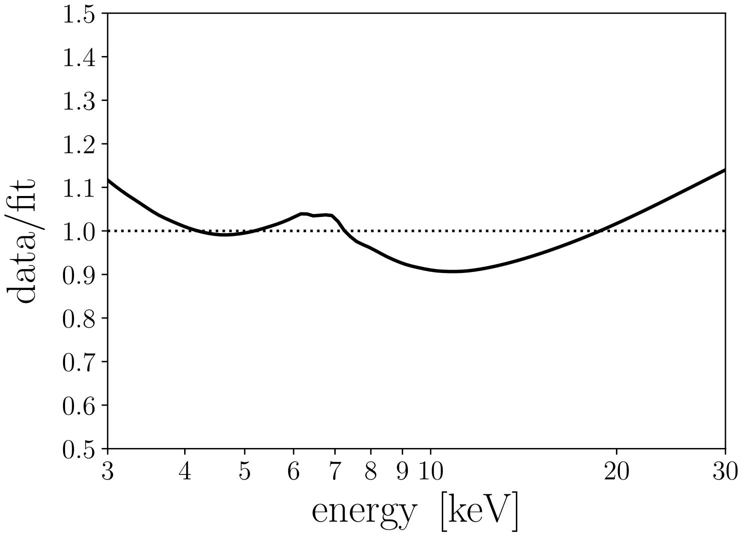

Figure 3.11: The predicted spectrum divided by a power-law fit to the range shown for $\dot{m} = 0.01$ and $i = 25°$.

In Figure 3.12, we show those photons which *originate* from the Kα transition as a fraction of continuum photons at the same energy, as seen by a distant observer, at several inclinations for each accretion rate. It is important to note that while this representation emulates model-fitting procedures, these are *not* themselves model fits divided by the total flux. We produce these plots by keeping track of Kα photons as they diffuse from their point of creation to the disk surface and are then ray-traced to infinity, with no continuum-fitting needed. We calculate the equivalent width (EW) directly as well, as shown in Figure 3.13 as a function of observer angle.

The Fe Kα line profiles strongly resemble actual spectral data in the sense that they are fairly broad and their EWs are in the range often measured ($\sim$ 100 eV, see below). On the other hand, they also differ in some respects. In particular, the "shelf" at high energies in Figure 3.12 is due to the upscattering of Fe Kα photons as they traverse the corona, taken relative to a steeply-declining continuum; compare to Figure 3.14 which shows the continuum-*subtracted* version of the line profiles. With the notable exception of composite models like those presented in Steiner et al. (2017), this "shelf" line flux is typically not

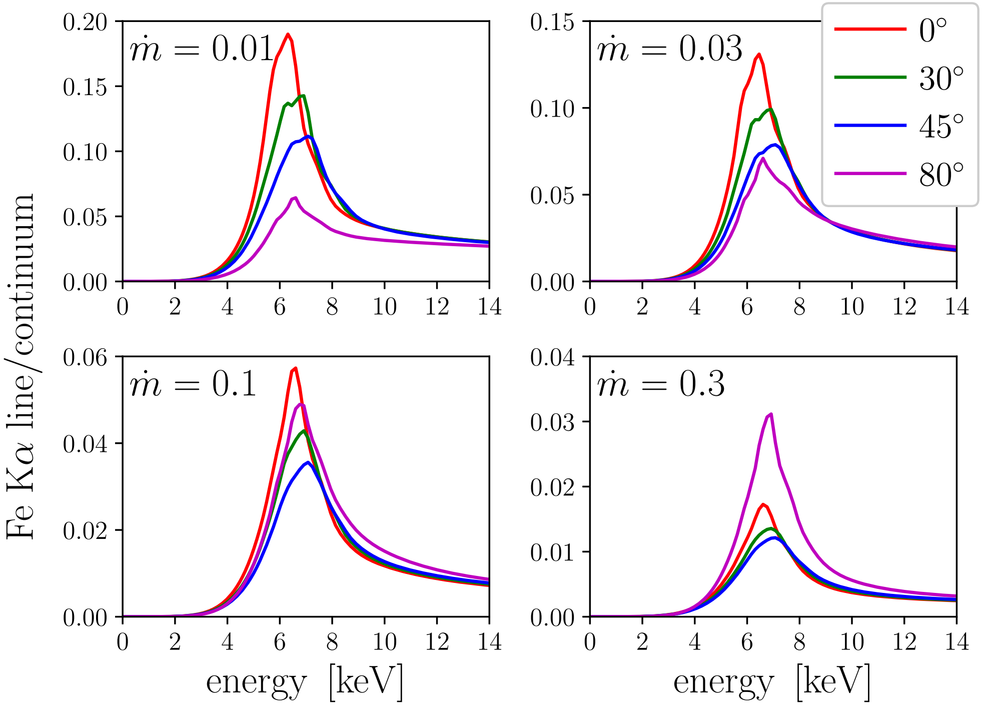

Figure 3.12: Photons whose origin is an Fe Kα transition, as a fraction of all continuum photons, once they have reached the distant observer; for four accretion rate cases at several inclinations each. The "shelf" at high energy is due to IC upscattering in the corona taken in ratio to a steeply-declining continuum. Note the difference in scale for each subplot.

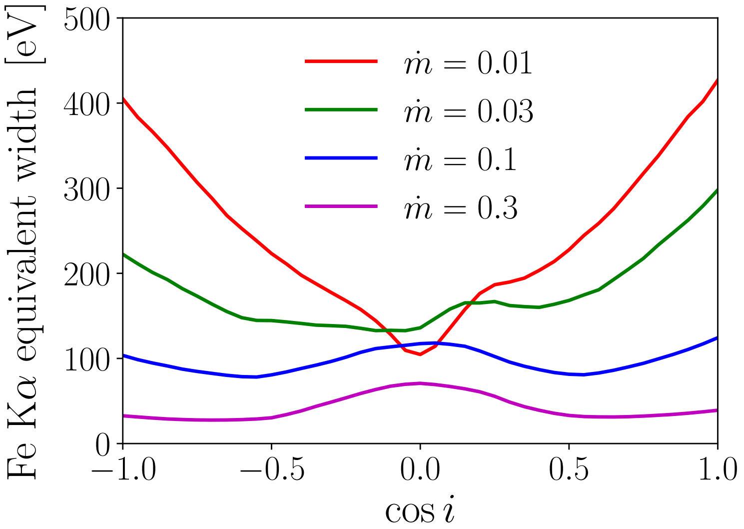

Figure 3.13: The Fe Kα equivalent width, as a function of observer angle, for each of the four accretion rate cases we consider. The EW is computed in the 2–8 keV range.

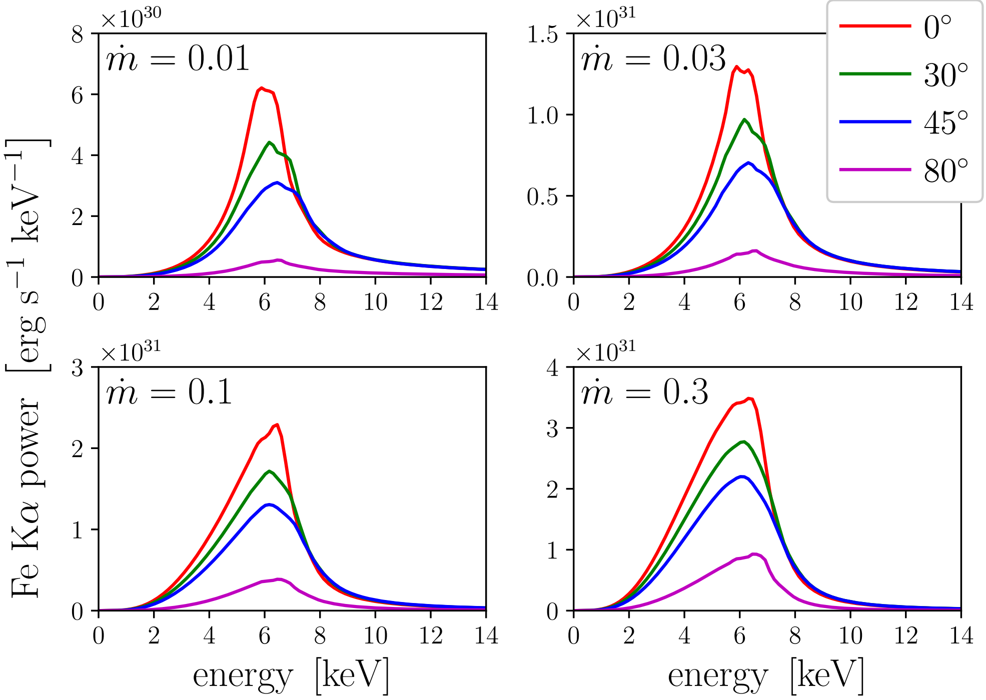

Figure 3.14: Fe Kα line spectral flux, excluding continuum photons. The "shelf" at high energy is less pronounced compared to Figure 3.12; this is due to *subtracting*, rather than *dividing by*, the steeply-declining continuum. Note again the difference in scale for each subplot.

accounted for by continuum-fitting models; rather, these upscattered Fe Kα photons would appear as continuum photons, potentially introducing a systematic bias in a continuum-subtraction procedure as the level of the perceived continuum at energies above the Kα feature is artificially elevated by a few percent. This coronal upscattering effect, in addition to our use of a non-spinning black hole, also explains the blueward asymmetry of the line profiles in Figure 3.12. The simple data/fit representation of Figure 3.11 is the closest approximation to actual observed line profiles: compared to, e.g., Cyg X-1 line profiles (Reynolds and Nowak, 2003; Walton et al., 2016), ours are nearly as broad, though with a slightly less extended red wing.

The Fe Kα feature becomes relatively weaker with respect to the continuum as the accretion rate increases—the peak contrast drops by a factor of six from $\dot{m} = 0.01$ to $\dot{m} = 0.3$

in Figure 3.12. This is consistent with the increasing ionization parameter (Tarter, Tucker, and Salpeter, 1969): $\log \xi$ varies with position (decreasing with radius), but is in the range 2.5–3.0 for $\dot{m} = 0.01$, increasing to 3.0–3.5, 3.5–4.0, and 4.0–4.5, for $\dot{m} = 0.03$, 0.1, and 0.3, respectively.

For the lower accretion rates, the line contrast drops monotonically with increasing inclination. However, as $\dot{m}$ increases, the near edge-on ($i = 80°$) view becomes stronger relative to the other viewing angles, and is twice the strength of the other three sample inclinations for $\dot{m} = 0.3$. The overall line flux for the near edge-on viewing angles is less than the face-on inclinations for all accretion rates (see Figure 3.14), but the strength of the line *relative* to the continuum is greater when viewed near edge-on because the disk itself obscures emission from outer radii (where the line flux is weak compared to the continuum) while, due to lensing, light from the inner disk region (where the line flux is strong compared to the continuum) still reaches the distant observer; this is only the case when there *is* any Kα emission at the innermost radii, i.e., for higher accretion rates (see Figure 3.15).

The line strengths we find are, overall, comparable to those typically observed, with EWs in the range 40–400 eV. Compare, for example, to the Walton et al. (2016) analysis of Cyg X-1 soft state spectra; they report an Fe Kα EW = 300–330 eV [see also the discussion in Reynolds and Nowak (2003)]. It is a well-known phenomenon that modeling-fitting of black hole X-ray spectra often results in inferred Fe abundances that are several-to-many times the solar value (Tomsick et al., 2018; García et al., 2018). Because we have not yet fit real data with our simulated spectra, nor do we analyze our theoretical spectra with the same techniques used by observers, it is not possible to make *direct* comparisons between our line strengths and those reported in, e.g., Walton et al. (2016). Nevertheless, that we use *only* solar Fe abundances yet still find strong Kα lines is encouraging. Our approach is fundamentally different from those often employed when fitting actual spectra, so it is difficult to pinpoint a single reason why we do not need supersolar Fe abundances to achieve strong lines. A major contributor, however, is likely our naturally extended corona (see Figure 3.3), which allows for Fe Kα production over a larger fraction of the disk surface. Figure 3.15 shows the radial dependence of the Fe Kα surface brightness for each accretion rate case, averaged over azimuth and the two surfaces of the disk. Like most phenomenological models, the variation with radius is roughly power-law—our power-laws, however, are approximately $\propto r^{-2}$ (steepening slightly with decreasing accretion rate), a shallower profile than is typically assumed from lamppost geometries [$\propto r^{-3}$ or steeper (Wilkins and Fabian, 2012; Dauser et al., 2013)]. Azimuthal variations superimposed on these radial gradients can be sizable: the relative standard deviation of the ϕ-variation of the Kα emission decreases with increasing $\dot{m}$, from $\sim 50\%$ for $\dot{m} = 0.01$ to $\lesssim 10\%$ for $\dot{m} = 0.3$.

The radius of peak Kα surface brightness moves inward with increasing accretion rate, from $\sim 10M$ for $\dot{m} = 0.01$ to $\sim 5M$ for $\dot{m} = 0.3$. The Kα surface brightness at radii interior to the peak increases with accretion rate as well; for $\dot{m} = 0.3$, there is significant Kα production even just outside the event horizon. While the strength of the Fe line relative to the continuum diminishes with increasing accretion rate (Figure 3.13), the *number* of Kα photons increases as the accretion rate, and therefore the total luminosity, increases. Though we do find that the peak in Kα surface brightness occurs somewhat *near* the ISCO, we do not find a sharp cutoff exactly *at* the ISCO. This should not be too surprising. If gas flows into the black hole, there must be some gas between the event horizon and the ISCO which might produce Fe Kα emission; conversely, if the accretion rate is low and the illuminating flux particularly powerful, there could be no available unstripped Fe to emit photons except for well outside the ISCO. In general, the interior Kα emission cutoff cannot just be a function of the spin alone—it depends also on the disk's surface density and ionization state, which themselves depend on the accretion rate, as we demonstrate in Figure 3.15 [see also the discussions in Reynolds and Begelman (1997), Krolik and Hawley (2002), and Beckwith, Hawley, and Krolik (2008)].

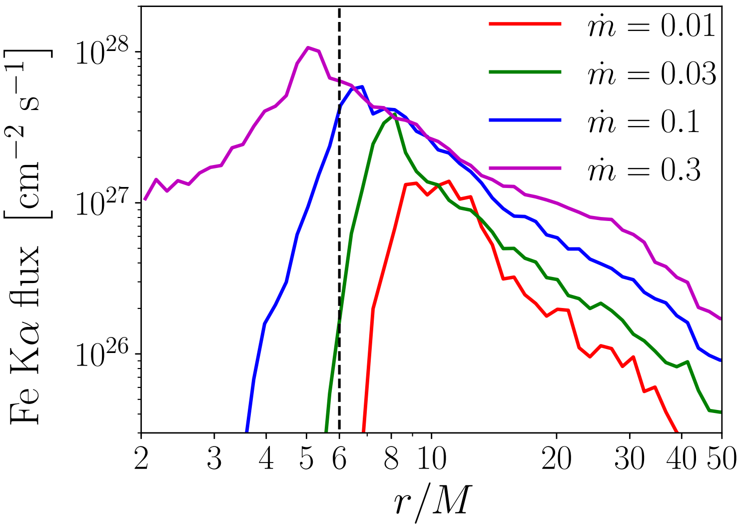

Figure 3.15: Fe Kα surface brightness, averaged over azimuth and both disk surfaces, for four accretion rates. Note the location of the peaks with respect to the ISCO at $r = 6M$.

3.3 Discussion

The most important result is simply that our machinery can manufacture *forward* predictions of the entire X-ray spectrum radiated by an accreting stellar-mass black hole—line *and* continuum features together—in a self-consistent, energy-conserving fashion, directly from the output of high-resolution 3D GRMHD simulations. It is worth repeating that we have required *no* assumptions about the accretion flow geometry at any point—no lamppost coronae, or disk inner edges fixed exactly at the ISCO. And yet, by specifying *only* the physically meaningful parameters of mass, spin, accretion rate, and elemental abundances, and then applying to the simulation data the relevant physical principles and carrying out detailed radiative transfer and photoionization calculations, we are able to produce spectra similar in shape and principal features to those actually observed from stellar-mass black holes. It also bears emphasizing that we employed standard techniques without preference for a desired outcome—a Monte Carlo radiation transport code which treats only Compton scattering is the natural choice in the hot, optically thin corona, while a plane-parallel Feautrier method which treats Compton scattering, free-free, and all atomic processes, is the natural choice in the cooler, optically thick disk. That the output of these methods when applied to simulation data resemble so well the familiar X-ray spectra of their real counterparts encourages us to attempt to understand these objects from the standpoint of direct application of well-understood physical principles, as opposed to phenomenological modeling. In this vein, we ultimately plan to use this method for the production of grids of spectra—allowing observers to attempt to fit real spectral data with an XSPEC package that requires only a relatively small set of physical parameters. Moreover, as simulation codes are improved (in particular with regard to the equation of state), our methods can be readily employed upon the data they produce.

References

Tanaka, Y., K. Nandra, A. C. Fabian, H. Inoue, C. Otani, T. Dotani, K. Hayashida, K. Iwasawa, T. Kii, H. Kunieda, F. Makino, and M. Matsuoka (1995). "Gravitationally redshifted emission implying an accretion disk and massive black hole in the active galaxy MCG-6-30-15". In: *Nature* 375, pp. 659–661. DOI: `10.1038/375659a0`.

Liang, E. P. T. (1979). "On the hard X-ray emission mechanism of active galactic nuclei sources". In: *ApJL* 231, pp. L111–L114. DOI: `10.1086/183015`.

Haardt, F. and L. Maraschi (1991). "A two-phase model for the X-ray emission from Seyfert galaxies". In: *ApJL* 380, pp. L51–L54. DOI: `10.1086/186171`.

Kinch, B. E., J. D. Schnittman, T. R. Kallman, and J. H. Krolik (2016). "Fe Kα Profiles from Simulations of Accreting Black Holes". In: *ApJ* 826, 52, p. 52. DOI: `10.3847/0004-637X/826/1/52`. arXiv: `1604.01126 [astro-ph.HE]`.

Mitsuda, K., H. Inoue, K. Koyama, K. Makishima, M. Matsuoka, Y. Ogawara, K. Suzuki, Y. Tanaka, N. Shibazaki, and T. Hirano (1984). "Energy spectra of low-mass binary X-ray sources observed from TENMA". In: *PASJ* 36, pp. 741–759.

Dauser, T., J. Garcia, J. Wilms, M. Böck, L. W. Brenneman, M. Falanga, K. Fukumura, and C. S. Reynolds (2013). "Irradiation of an accretion disc by a jet: general properties and implications for spin measurements of black holes". In: *MNRAS* 430, pp. 1694–1708. DOI: `10.1093/mnras/sts710`. arXiv: `1301.4922 [astro-ph.HE]`.

Reynolds, C. S. and M. A. Nowak (2003). "Fluorescent iron lines as a probe of astrophysical black hole systems". In: *Phys. Rep.* 377, pp. 389–466. DOI: `10.1016/S0370-1573(02)00584-7`. eprint: `astro-ph/0212065`.

Ross, R. R. and A. C. Fabian (2005). "A comprehensive range of X-ray ionized-reflection models". In: *MNRAS* 358, pp. 211–216. DOI: `10.1111/j.1365-2966.2005.08797.x`. eprint: `astro-ph/0501116`.

García, J. and T. R. Kallman (2010). "X-ray Reflected Spectra from Accretion Disk Models. I. Constant Density Atmospheres". In: *ApJ* 718, pp. 695–706. DOI: `10.1088/0004-637X/718/2/695`. arXiv: `1006.0485 [astro-ph.HE]`.

García, J., T. R. Kallman, and R. F. Mushotzky (2011). "X-ray Reflected Spectra from Accretion Disk Models. II. Diagnostic Tools for X-ray Observations". In: *ApJ* 731, 131, p. 131. DOI: `10.1088/0004-637X/731/2/131`. arXiv: `1101.1115 [astro-ph.HE]`.

García, J., T. Dauser, C. S. Reynolds, T. R. Kallman, J. E. McClintock, J. Wilms, and W. Eikmann (2013). "X-Ray Reflected Spectra from Accretion Disk Models. III. A Complete

Grid of Ionized Reflection Calculations". In: *ApJ* 768, 146, p. 146. DOI: `10.1088/0004-637X/768/2/146`. arXiv: `1303.2112 [astro-ph.HE]`.

García, J., T. Dauser, A. Lohfink, T. R. Kallman, J. F. Steiner, J. E. McClintock, L. Brenneman, J. Wilms, W. Eikmann, C. S. Reynolds, and F. Tombesi (2014). "Improved Reflection Models of Black Hole Accretion Disks: Treating the Angular Distribution of X-Rays". In: *ApJ* 782, 76, p. 76. DOI: `10.1088/0004-637X/782/2/76`. arXiv: `1312.3231 [astro-ph.HE]`.

Reynolds, C. S. (2013). "The spin of supermassive black holes". In: *Classical and Quantum Gravity* 30.24, 244004, p. 244004. DOI: `10.1088/0264-9381/30/24/244004`. arXiv: `1307.3246 [astro-ph.HE]`.

Miller, M. C. and J. M. Miller (2015). "The masses and spins of neutron stars and stellar-mass black holes". In: *Phys. Rep.* 548, pp. 1–34. DOI: `10.1016/j.physrep.2014.09.003`. arXiv: `1408.4145 [astro-ph.HE]`.

Noble, S. C., J. H. Krolik, and J. F. Hawley (2009). "Direct Calculation of the Radiative Efficiency of an Accretion Disk Around a Black Hole". In: *ApJ* 692, pp. 411–421. DOI: `10.1088/0004-637X/692/1/411`. arXiv: `0808.3140`.

Schnittman, J. D. and J. H. Krolik (2013). "A Monte Carlo Code for Relativistic Radiation Transport around Kerr Black Holes". In: *ApJ* 777, 11, p. 11. DOI: `10.1088/0004-637X/777/1/11`. arXiv: `1302.3214 [astro-ph.HE]`.

Schnittman, J. D., J. H. Krolik, and S. C. Noble (2013). "X-Ray Spectra from Magnetohydrodynamic Simulations of Accreting Black Holes". In: *ApJ* 769, 156, p. 156. DOI: `10.1088/0004-637X/769/2/156`. arXiv: `1207.2693 [astro-ph.HE]`.

Noble, S. C., J. H. Krolik, J. D. Schnittman, and J. F. Hawley (2011). "Radiative Efficiency and Thermal Spectrum of Accretion onto Schwarzschild Black Holes". In: *ApJ* 743, 115, p. 115. DOI: `10.1088/0004-637X/743/2/115`. arXiv: `1105.2825 [astro-ph.HE]`.

Hawley, J. F., S. A. Richers, X. Guan, and J. H. Krolik (2013). "Testing Convergence for Global Accretion Disks". In: *ApJ* 772, 102, p. 102. DOI: `10.1088/0004-637X/772/2/102`. arXiv: `1306.0243 [astro-ph.IM]`.

Novikov, I. D. and K. S. Thorne (1973). "Astrophysics of black holes." In: *Black Holes (Les Astres Occlus)*. Ed. by C. Dewitt and B. S. Dewitt, pp. 343–450.

Mihalas, D. (1978). *Stellar atmospheres, 2nd edition*. San Francisco, W. H. Freeman and Co.

Mihalas, D. (1985). "The computation of radiation transport using Feautrier variables. I - Static media". In: *Journal of Computational Physics* 57, pp. 1–25. DOI: `10.1016/0021-9991(85)90050-6`.

Kallman, T. and M. Bautista (2001). "Photoionization and High-Density Gas". In: *ApJS* 133, pp. 221–253. DOI: `10.1086/319184`.

Nayakshin, S., D. Kazanas, and T. R. Kallman (2000). "Thermal Instability and Photoionized X-Ray Reflection in Accretion Disks". In: *ApJ* 537, pp. 833–852. DOI: `10.1086/309054`. eprint: `astro-ph/9909359`.

Rybicki, G. B. and A. P. Lightman (1986). *Radiative Processes in Astrophysics*, p. 400.

Shakura, N. I. and R. A. Sunyaev (1973). "Black holes in binary systems. Observational appearance." In: *A&A* 24, pp. 337–355.

Chandrasekhar, S. (1960). *Radiative transfer.*

Grevesse, N., A. Noels, and A. J. Sauval (1996). "Standard Abundances". In: *Cosmic Abundances.* Ed. by S. S. Holt and G. Sonneborn. Vol. 99. Astronomical Society of the Pacific Conference Series, p. 117.

Remillard, R. A. and J. E. McClintock (2006). "X-Ray Properties of Black-Hole Binaries". In: *ARA&A* 44, pp. 49–92. DOI: `10.1146/annurev.astro.44.051905.092532`. eprint: `astro-ph/0606352`.

McClintock, J. E. and R. A. Remillard (2006). "Black hole binaries". In: *Compact stellar X-ray sources.* Ed. by W. H. G. Lewin and M. van der Klis, pp. 157–213.

Narayan, R., Y. Zhu, D. Psaltis, and A. Sądowski (2016). "HEROIC: 3D general relativistic radiative post-processor with comptonization for black hole accretion discs". In: *MNRAS* 457, pp. 608–628. DOI: `10.1093/mnras/stv2979`. arXiv: `1510.04208 [astro-ph.HE]`.

Jiang, Y.-F., J. M. Stone, and S. W. Davis (2014). "An Algorithm for Radiation Magnetohydrodynamics Based on Solving the Time-dependent Transfer Equation". In: *ApJS* 213, 7, p. 7. DOI: `10.1088/0067-0049/213/1/7`. arXiv: `1403.6126 [astro-ph.IM]`.

Sądowski, A., R. Narayan, J. C. McKinney, and A. Tchekhovskoy (2014). "Numerical simulations of super-critical black hole accretion flows in general relativity". In: *MNRAS* 439, pp. 503–520. DOI: `10.1093/mnras/stt2479`. arXiv: `1311.5900 [astro-ph.HE]`.

Steiner, J. F., J. A. García, W. Eikmann, J. E. McClintock, L. W. Brenneman, T. Dauser, and A. C. Fabian (2017). "Self-consistent Black Hole Accretion Spectral Models and the Forgotten Role of Coronal Comptonization of Reflection Emission". In: *ApJ* 836, 119, p. 119. DOI: `10.3847/1538-4357/836/1/119`. arXiv: `1701.03777 [astro-ph.HE]`.

Walton, D. J., J. A. Tomsick, K. K. Madsen, V. Grinberg, D. Barret, S. E. Boggs, F. E. Christensen, M. Clavel, W. W. Craig, A. C. Fabian, F. Fuerst, C. J. Hailey, F. A. Harrison, J. M. Miller, M. L. Parker, F. Rahoui, D. Stern, L. Tao, J. Wilms, and W. Zhang (2016). "The Soft State of Cygnus X-1 Observed with NuSTAR: A Variable Corona and a Stable Inner Disk". In: *ApJ* 826, 87, p. 87. DOI: `10.3847/0004-637X/826/1/87`. arXiv: `1605.03966 [astro-ph.HE]`.

Tarter, C. B., W. H. Tucker, and E. E. Salpeter (1969). "The Interaction of X-Ray Sources with Optically Thin Environments". In: *ApJ* 156, p. 943. DOI: `10.1086/150026`.

Tomsick, J. A., M. L. Parker, J. A. García, K. Yamaoka, D. Barret, J.-L. Chiu, M. Clavel, A. Fabian, F. Fürst, P. Gandhi, V. Grinberg, J. M. Miller, K. Pottschmidt, and D. J. Walton (2018). "Alternative Explanations for Extreme Supersolar Iron Abundances Inferred from the Energy Spectrum of Cygnus X-1". In: *ApJ* 855, 3, p. 3. DOI: `10.3847/1538-4357/aaaab1`. arXiv: `1801.07267 [astro-ph.HE]`.

García, J. A., T. R. Kallman, M. Bautista, C. Mendoza, J. Deprince, P. Palmeri, and P. Quinet (2018). "The Problem of the High Iron Abundance in Accretion Disks around Black Holes". In: *Astronomical Society of the Pacific Conference Series.* Vol. 515. Astronomical Society of the Pacific Conference Series, p. 282. arXiv: `1805.00581 [astro-ph.HE]`.

Wilkins, D. R. and A. C. Fabian (2012). "Understanding X-ray reflection emissivity profiles in AGN: locating the X-ray source". In: *MNRAS* 424, pp. 1284–1296. DOI: `10.1111/j.1365-2966.2012.21308.x`. arXiv: `1205.3179 [astro-ph.HE]`.

Reynolds, C. S. and M. C. Begelman (1997). “Iron Fluorescence from within the Innermost Stable Orbit of Black Hole Accretion Disks”. In: *ApJ* 488, pp. 109–118. eprint: `astro-ph/9705136`.

Krolik, J. H. and J. F. Hawley (2002). “Where Is the Inner Edge of an Accretion Disk around a Black Hole?” In: *ApJ* 573, pp. 754–763. DOI: `10.1086/340760`. eprint: `astro-ph/0203289`.

Beckwith, K., J. F. Hawley, and J. H. Krolik (2008). “Where is the radiation edge in magnetized black hole accretion discs?” In: *MNRAS* 390, pp. 21–38. DOI: `10.1111/j.1365-2966.2008.13710.x`. arXiv: `0801.2974`.

Chapter 4

Improved Corona Cooling Function

As discussed in the previous chapters, the cooling function employed by HARM3D uses a target temperature approach: gravitationally-bound gas above a specified target temperature is cooled to the target temperature over one orbital timescale; the target temperature is chosen so as to achieve a pre-specified small disk aspect ratio, i.e., to achieve a geometrically thin disk. An ideal cooling function would instead consider the relevant microphysics within each fluid element and from there calculate the rate at which the internal energy of the gas is converted to photons. Such a calculation requires knowledge of the energy-dependent radiation field in all cells. Simultaneously solving the magnetohydrodynamics equations *and* the global angle- and energy-dependent radiation transport equation, in full General Relativity, is both computationally expensive (typically prohibitively so) and technically challenging. Even so, significant progress has been made in the last decade, though the problem is generally made tractable by introducing at least one of the following simplifying assumptions: abandoning General Relativity in favor of a pseudo-Newtownian description of the gravitational potential, while performing realistic, multi-angle group radiation transport (Jiang, Stone, and Davis, 2014a; Jiang, Stone, and Davis, 2014b; Jiang, Stone, and Davis, 2017; Jiang et al., 2019); or, limiting the possible angular-dependence of the radiation field by invoking either flux-limited diffusion (Zanotti et al., 2011; Roedig, Zanotti, and Alic, 2012) or, more recently, the "M1 closure" relation, in either axisymmetric (2D) (Sądowski et al., 2014) or 3D simulations (Fragile et al., 2012; Fragile, Olejar, and Anninos, 2014; McKinney et al., 2014; Sądowski et al., 2016). All attempts have eschewed energy-dependent transfer in favor of a "grey" atmosphere—the radiation field is treated as monochromatic, coupled to the fluid only through the Rosseland mean (Rybicki and Lightman, 1986) of the combined Thomson scattering and free-free absorption opacities. The first of these approximations, the pseudo-Newtonian potential, is especially problematic in regions close to the black hole where General Relativistic effects play a critical role in determining both the structure of the accretion flow and photon trajectories. The others are essentially variants of a diffusion approximation, and are best suited to the cooler, denser, and optically thick body of the accretion disk, where the environment is similar to those found in stellar atmospheres—the field from which these methods, and grey transfer, originate. They are all especially poorly-suited to the diffuse, hot, optically thin corona, especially at small radii near the black hole.

In what follows, we describe a new cooling function specifically tailored to the corona regime. It is "switched on" at a time after the simulation has evolved long enough with the original, target-temperature cooling function that it has achieved a statistically steady-state, and applies only in the corona as defined in previous chapters, i.e., outside the upper and lower photosphere surfaces. Within the disk body (defined as the region between the photospheres), the original, target-temperature cooling function remains in place. Our new cooling function is a first effort to incorporate an approximate version of the physics treated so carefully by PANDURATA into a 3D GRMHD simulation. In this chapter, we explore the effect of a more realistic corona cooling function on the dynamical and thermodynamic properties of a sample, $a = 0$ simulation.

4.1 Improving on the Target-Temperature Cooling Function

The "original" cooling function—what we have referred to as the "target-temperature" cooling function—was introduced in Noble, Krolik, and Hawley (2009) and further developed in Noble, Krolik, and Hawley (2010) and Noble et al. (2011). A radius-dependent target temperature T_* (expressed in code units) is set according to

$$T_* = \frac{\pi}{2}\frac{R_z(r)}{r}\left[\frac{H(r)}{r}\right]^2, \tag{4.1}$$

where R_z is the relativistic correction to the vertical component of gravity at radius r (Abramowicz, Lanza, and Percival, 1997), and H is the density-weighted scale height of the disk. The desired disk aspect ratio, H/r, is chosen *a priori* to achieve a geometrically thin disk—for the ThinHR simulation series used throughout this dissertation, the desired disk aspect ratio is $H/r = 0.05$. When gas on a bound orbit exceeds the target temperature, it is cooled back to the target temperature by introducing a nonzero sink term on the right-hand side of the local stress-energy conservation equation solved by HARM3D:

$$\nabla_\nu T^\nu_\mu = -\mathcal{L} u_\mu, \tag{4.2}$$

here T^ν_μ is the stress-energy tensor and u_μ is the specific four-momentum; $\mathcal{L}$ is chosen so that the gas cools to the target temperature over one circular orbital period at its given radius. If the gas is at or below T_*, or is gravitationally unbound, $\mathcal{L} = 0$. As the gas is cooled, its pressure and therefore support against gravity decreases, settling back toward the midplane, thereby achieving a geometrically thin disk.

The target-temperature approach has several key benefits: as intended, it gives rise to a geometrically thin, optically thick, cool, dense disk, sandwiched between a hotter, diffuse corona—a configuration with considerable observational support; the implementation is independent of the central black hole mass scale M and the nominal accretion rate $\dot{m}$ (in Eddington units) and therefore, in principle, the results of a single simulation can be scaled to, for example, both stellar-mass X-ray binary systems and supermassive active galactic nuclei; and it is easy to evaluate as it depends only on local properties of a given fluid element.

On the other hand, of course, it is profoundly unphysical: the choice of target temperature is motivated not by the relevant microphysics, but by the desire to achieve a configuration-by-design that agrees well with observational evidence. There are other concerns as well. By virtue of its implementation as a local sink term, it is everywhere "optically thin"; that is, the dissipation rate is an entirely *intensive* quantity—even deep within the disk, energy lost (nominally to photons) simply vanishes, while in reality these photons would diffuse through the optically thick material, scattering and undergoing absorption/re-emission along the way. In the corona, large swaths of gravitationally unbound matter may not undergo cooling at all, while the gas that is cooled does so on a circular orbital timescale which may not be relevant to its actual dynamics.

An optically thin cooling function is, however, a good approximation in the truly optically thin corona. Thus we can seek a more physical cooling function there while still retaining the implementation of Equation 4.2. In addition, we understand the actual physical mechanism behind coronal cooling: the inverse Compton (IC) scattering of thermal seed photons from the disk surface off of very hot electrons—this is exactly the physics treated with great care by PANDURATA. Below we detail the development of a new cooling function $\mathcal{L}$ to replace the target-temperature cooling function in the corona; to emphasize the physical origin of the new cooling function—and to distinguish it from the target-temperature cooling function which will remain in use in the disk body—we refer to it simply as the IC cooling function.

4.2 One vs. Two Temperature Fluid

In this chapter, we require the ion and electron populations to be at the same temperature in each simulation cell, $T_e = T_i$, i.e., a one temperature fluid. In Chapter 6, we extend the method to treat the ion and electron temperatures separately, $T_e \neq T_i$, i.e., a two temperature fluid, with the assumption that electrons are heated only through Coulomb collisions with ions.

As we will discuss in more detail in Chapter 6, these two prescriptions represent, essentially, the limiting cases of maximally- and minimally-efficient radiative cooling, respectively.

The one temperature fluid assumption has two distinct advantages: it is less computationally taxing (and therefore the spin survey in the following chapter is less costly to perform using it), and it requires no special description of the ion-electron coupling mechanism—we simply assume that *some* such strong coupling mechanism exists, or that turbulent dissipation is shared nearly equally between ions and electrons, or some combination thereof. In Chapter 6 we must assume a specific coupling mechanism, namely Coulomb collisions, in addition to the assumption that all turbulent energy is initially injected into the ions only—though these are both a simplification of the more complex underlying plasma physics.

4.3 Method

4.3.1 Inverse Compton Power

As discussed in previous chapters, the dominant emission mechanism in the corona is the inverse Compton scattering of thermal seed photons originating from the disk surface. The classic expression for IC energy exchanged per scatter per unit time is [see Blumenthal and Gould (1970) for details on Compton scattering expressions used in this chapter]:

$$P_{\rm IC} = \frac{4}{3}\sigma_T c \gamma^2 \beta^2 u_{\rm rad}, \tag{4.3}$$

where σ_T is the Thomson scattering cross section, c is the speed of light, $\gamma = 1/\sqrt{1-\beta^2}$ with $\beta = v/c$—where v refers to the electron velocity—and $u_{\rm rad}$ is the radiation energy density. In the nonrelativistic limit, i.e., when the dimensionless electron temperature $\Theta_e \equiv kT_e/m_e c^2 \ll 1$, $\langle \gamma^2 \beta^2 \rangle \simeq 3\Theta_e$, and so

$$P_{\text{IC, non-relativistic}} = \frac{4}{3}\sigma_T c (3\Theta_e) u_{\rm rad}. \tag{4.4}$$

In the relativistic limit, i.e., $\Theta_e \gg 1$, $\langle \gamma^2 \beta^2 \rangle \simeq 12\Theta_e^2$, therefore

$$P_{\text{IC, relativistic}} = \frac{4}{3}\sigma_T c (12\Theta_e^2) u_{\rm rad}. \tag{4.5}$$

Because each expression is much larger than the other in their appropriate regimes, we can represent the IC power in both limits by their sum. In addition, we multiply by the electron density $n_e = \chi(\rho/m_i)$, where χ is the free electron fraction (number of free electrons per ion, equal to 1.21 for a fully-ionized plasma with solar elemental abundances; a variable χ might also be used to account for the presence of electron-positron pairs due to pair production) and m_i is the mean ion mass ($\simeq m_p$), to translate from energy exchanged per scatter per unit time to a volumetric cooling rate. The final expression is:

$$\mathcal{L}_{\rm IC} = \frac{4\sigma_T c\chi}{m_i}\rho u_{\rm rad}\Theta_e(1+4\Theta_e). \tag{4.6}$$

This is the expression for the IC cooling rate which enters into HARM3D's stress-energy equation 4.2 in place of the target-temperature cooling rate for those fluid elements in the corona. It requires as input: the density (which is of course already computed), the electron temperature, and the radiation energy density. As discussed, we will assume in this chapter that some strong coupling mechnanism forces $T_e = T_i$. From standard thermodynamics and the ideal gas law, the gas pressure $p_{\rm gas}$, the internal energy density u, and the electron and ion temperatures are related by

$$p_{\rm gas} = (c_P/c_V - 1)u = n_e k T_e + n_i k T_i, \tag{4.7}$$

where c_P/c_V is the specific heat ratio, i.e., the adiabatic index [equal to 5/3 for a monatomic gas; though we assume $c_P/c_V = 5/3$ for simplicity in this work, a more detailed consideration of relativistic plasma physics leads to slightly different, and variable, adiabatic indices (Mignone and McKinney, 2007)]. From this we derive an expression for the dimensionless electron temperature:

$$\Theta_e = \frac{m_i}{m_e}\frac{c_P/c_V - 1}{1+\chi}\frac{u}{\rho c^2}. \tag{4.8}$$

This expression depends only on the (mass) density and the internal energy density—which, like the density, is part of HARM3D's fluid solution. Again, this equation holds so long as there is some strong coupling mechanism forcing $T_e = T_i$. What remains, then, is to estimate $u_{\rm rad}$.

4.3.2 Radiation Energy Density

In order to estimate the radiation energy density $u_{\rm rad}$ at each point in the corona, we first make several key simplifications:

1. We ignore General and special relativistic effects. The thermal seed photons launched from the disk surface are assumed to travel in straight rays, undergoing neither red/blue-shifting nor beaming due to the bulk fluid flow of the rotating accretion disk, nor gravitational redshifting due to their origin in a deep gravitational potential.

2. We do not account for scattering or obscuration of the disk emission by intervening corona material between the disk surface and a given point in the corona.

3. We adopt the "fast light" approximation, i.e., we do not account for the light travel time between a point on the disk photosphere and a point in the corona; rather, the radiation energy density in the corona each timestep is computed from the thermal flux from the disk surface at the same timestep.

With these assumptions in place, we can derive an expression for $u_{\rm rad}$ by integrating the thermal seed photon flux over the disk surface with an appropriate geometric weight. Let $\mathbf{r}$ indicate the location of the coronal cell in question, and let $\mathbf{r}'$ locate a surface cell on the photosphere. Then:

$$du_{\rm rad}(\mathbf{r}) = \frac{1}{c}\frac{F_{\rm disk}(\mathbf{r}')\cos\vartheta dA'}{R^2}, \tag{4.9}$$

where the factor of $1/c$ translates flux into energy density, $\mathbf{R} = \mathbf{r} - \mathbf{r}'$, ϑ is the angle between $\mathbf{R}$ and the disk surface normal vector $\hat{\mathbf{n}}$, dA' is the (infinitesimal) element of the disk surface area, and $F_{\rm disk}$ is the assumed blackbody seed photon flux with effective temperature $T_{\rm eff}$ set in the same fashion as in PANDURATA, i.e., by integrating the cooling function within the disk at the specified (r', ϕ'):

$$\int_{\Theta_{\rm bot}}^{\Theta_{\rm top}} \mathcal{L} d\theta \sqrt{g_{\theta\theta}} = 2\sigma_{\rm SB} T_{\rm eff}^4. \tag{4.10}$$

We can re-express $\cos\vartheta$ in terms of the spherical coordinates of the coronal and photosphere cells:

$$\cos\vartheta = \pm \frac{r}{R}\left[\sin\theta\cos\theta'\left(\cos\phi\cos\phi' + \sin\phi\sin\phi'\right) - \cos\theta\sin\theta'\right] = \frac{r}{R} G_{\pm}(\mathbf{r}, \mathbf{r}'), \tag{4.11}$$

where + is used for the lower half of the corona and − for the upper half. In addition, it can be shown that the infinitesimal solid angle $d\Omega'$ subtended by the disk surface element at $\mathbf{r}'$ from the coronal cell at $\mathbf{r}$ is:

$$d\Omega' = 2\pi\left[1 - \left(1 + \frac{dA'}{\pi R^2}\right)^{-1/2}\right]. \tag{4.12}$$

Substituting equations 4.11 and 4.12 into equation 4.9, and integrating over the disk surface, we arrive at

$$u_{\rm rad}(\mathbf{r}) = 2\pi \int_{\partial A'} \frac{r}{R} F_{\rm disk}(\mathbf{r}') G_{\pm}(\mathbf{r}, \mathbf{r}') \left[1 - \left(1 + \frac{dA'}{\pi R^2}\right)^{-1/2}\right]. \tag{4.13}$$

This expression is computed in each coronal cell each timestep. To ease the computational burden of the numerical integration of the right-hand side of the above equation, a coarsened sampling of the photosphere grid (e.g., including only every eighth ϕ grid-point and every sixth r grid-point) can be used without significant loss in accuracy.

4.3.3 The Compton Temperature

It is also useful to estimate the Compton temperature, T_C, in each coronal cell. The Compton temperature—the temperature at which Compton heating is balanced by Compton cooling—is, in the non-relativistic limit:

$$kT_C = \frac{1}{4}\frac{\int_0^\infty h\nu J_\nu d\nu}{\int_0^\infty J_\nu d\nu} = \frac{1}{4}\langle\varepsilon\rangle. \tag{4.14}$$

In other words, the Compton temperature is equal to a quarter the mean photon energy. For a pure blackbody, it is easy to show that the mean photon energy is equal to $3.832kT_{\rm eff}$. Therefore, T_C in a given coronal cell can be found by averaging $T_{\rm eff}$ over the disk surface, weighted by the contribution of each particular photosphere surface element's flux to the total radiation energy density. That is:

$$T_C = \frac{3.832}{4}\frac{\sum_n u_{{\rm rad},n} T_{{\rm eff},n}}{\sum_n u_{{\rm rad},n}}, \tag{4.15}$$

where $T_{{\rm eff},n}$ is the effective temperature of the $n^{\rm th}$ disk surface element and $u_{{\rm rad},n}$ is the evaluation of the right-hand side of equation 4.13 for a particular photosphere element (performed in the course of numerical integration). The expression for IC power derived above, equation 4.6, is valid only if $T_e \gg T_C$; as we show below, under the assumption that $T_e = T_i$, this condition is always met, which indicates that Compton heating is negligible compared to Compton cooling. We revisit Compton heating in Chapter 6 when we explore consequences of relaxing the strong ion-electron coupling assumption.

4.3.4 The IC Cooling Time

Equation 4.6 for the IC cooling power is the time-rate change in the internal energy of the gas. That is, in the fluid rest frame:

$$\frac{du}{dt} = -\mathcal{L}_{\rm IC}. \tag{4.16}$$

If the expression for Θ_e in equation 4.8 (derived assuming $T_e = T_i$) is substituted into equation 4.6, the differential equation above can be solved for $u(t)$, setting $u(0) = u_0$, with the solution:

$$u(t) = \frac{u_0}{(1 + bu_0)e^{at} - bu_0}, \tag{4.17}$$

in which

$$a \equiv \frac{4\sigma_T}{m_e c} \frac{\chi}{1+\chi} \left(c_P/c_V - 1\right) u_{\rm rad}, \tag{4.18}$$

$$b \equiv 4 \frac{m_i}{m_e} \frac{(c_P/c_V - 1)}{1+\chi} \frac{1}{\rho c^2}. \tag{4.19}$$

From equation 4.17, we calculate the cooling time $t_{\rm cool}$, or the time over which—assuming $u_{\rm rad}$ and ρ are constant—the internal energy decreases from $u_0 \to u_0/e$:

$$t_{\rm cool} = \frac{1}{a} \ln \left(\frac{e + bu_0}{1 + bu_0} \right). \tag{4.20}$$

By inspection of the above equations, we see that the conditions for a short cooling time are either a high radiation energy density or a high initial electron temperature. These conditions make sense: for the former, plentiful photons make inverse Compton scattering more efficient; for the latter, compare to equation 4.8 to see that $bu_0 = 4\Theta_e$, and it is generally the case that hotter gas cools faster. Because of the quadratic term in the expression for the IC cooling rate, using the instantaneous rate of equation 4.6 in HARM3D can overestimate the timestep-to-timestep cooling in very hot cells. We instead set the cooling rate equal to appropriate time-averaged cooling rate over the timestep:

$$\bar{\mathcal{L}}_{\rm IC} = \frac{u_0 - u(\Delta\tau)}{\Delta\tau}, \tag{4.21}$$

where $\Delta\tau$ is the proper time interval in the given coronal cell corresponding to the *global* simulation (coordinate) timestep Δt. In addition, if $t_{\rm cool} > \Delta\tau$ in any cell, the global timestep is reset accordingly to match the shortest $t_{\rm cool}$. As mentioned above, the value of $\bar{\mathcal{L}_{\rm IC}}$ is set assuming $u_{\rm rad}$ and ρ are constant. While $u_{\rm rad}$ is a function of (an average over) the disk structure—and will therefore vary more slowly—a given coronal cell's density will of course rapidly change in response to a change in its internal energy. To maintain the integrity of the numerical fluid dynamics solution, then, we must be sure that no cells cool too substantially each timestep.

In practice, $\bar{\mathcal{L}_{\rm IC}}$ differs from $\mathcal{L}_{\rm IC}$ as given in equation 4.6, and $t_{\rm cool} < \Delta\tau$, only briefly right after the new corona cooling function is first "switched on." Because the target-temperature cooling function only cools bound gas (and does so less efficiently, as we see below), there are patches of unbound gas in the corona which may not have cooled for some time—these very hot patches rapidly cool under the new regime, and the usual HARM3D timestep-determination procedure is generally sufficient after several-to-ten M of simulation time have elapsed.

4.3.5 A Note on Units and Scaling

The derivations in the previous section were performed in physical, i.e., cgs units. To use these in HARM3D, however, we must translate them to code units. Using notation such that a quantity x is converted from code to cgs units by $x_{\rm cgs} = [x]x_{\rm code}$, we rewrite equation 4.6 as:

$$[\mathcal{L}]\mathcal{L}_{\rm IC,code} = \frac{4\sigma_T c\chi}{m_i}[\rho]\rho_{\rm code}[u_{\rm rad}]u_{\rm rad,code}\Theta_e(1+4\Theta_e). \tag{4.22}$$

Note that, in units for which $G = c = 1$, Θ_e (already a dimensionless quantity) is trivially re-expressed in code units by setting $c = 1$, $u \rightarrow u_{\rm code}$ and $\rho \rightarrow \rho_{\rm code}$ in equation 4.8. Consulting equations 3.1 and 3.2 from the previous chapter, we have:

$$[\mathcal{L}] = \frac{4\pi c^7}{\kappa G^2 M^2} \frac{\dot{m}/\eta}{\dot{M}_{\rm code}}, \tag{4.23}$$

$$[\rho] = \frac{4\pi c^2}{\kappa G M} \frac{\dot{m}/\eta}{\dot{M}_{\rm code}}, \tag{4.24}$$

$$[u_{\rm rad}] = [u] = c^2[\rho]. \tag{4.25}$$

Substituting these expressions into equation 4.22, we find:

$$\mathcal{L}_{\rm code} = \left(\frac{16\pi\sigma_T\chi}{m_i\kappa}\right) \frac{\dot{m}/\eta}{\dot{M}_{\rm code}} \rho_{\rm code} u_{\rm rad,code} \Theta_e (1 + 4\Theta_e). \tag{4.26}$$

The term in parentheses is dimensionless and, assuming a fixed free electron fraction (totally-ionized plasma is essentially guaranteed in the corona), constant.

The other dimensionless term, $(\dot{m}/\eta)\,/\dot{M}_{\rm code}$, does *not* appear in the "code units" form of the expression for the target-temperature cooling rate, but it does appear in the code units form of the IC cooling rate expression; it appears also in the expressions 4.23, 4.24 for translating the cooling rate and density from code to cgs units. This term serves to set the overall mass (and therefore dissipation) scale of the accretion flow. The radiative efficiency η is defined such that, in cgs units, the bolometric luminosity is related to the mass accretion rate by $L = \eta \dot{M} c^2$. The value of η used in the above expressions, however, must be chosen in advance—though in principle an effective radiative efficiency can be calculated *post hoc* using HARM3D coupled with PANDURATA+PTRANSX. For ease of comparison with analytic accretion disk theory, we choose the Novikov and Thorne (1973) values for the nominal radiative efficiency; for $a = 0$, $\eta_{\rm NT} = 0.0572$. The Novikov and Thorne (1973) radiative efficiencies are calculated assuming the fluid elements of an axisymmetric, time-steady disk radiate the entirety of their gravitational binding energy as measured from the ISCO radius. By definition, an accretion flow characterized by some radiative efficiency, say, $\eta_{\rm NT}$, accreting at $\dot{m} = 0.01$, has a luminosity equal to 0.01 $L_{\rm Edd}$. We describe these choices as "nominal" because their purpose is not to specify a resulting luminosity, but simply to set a scale—the actual luminosities should be on order of, but are not expected to be exactly equal to, 0.01 $L_{\rm Edd}$, as neither real nor simulated MHD accretion flows satisfy the assumptions of analytic accretion disk theory.

In previous chapters, we emphasized that a single HARM3D simulation required choosing only the dimensionless spin a/M, the output of which could then be scaled to a particular mass M and nominal accretion rate $\dot{m}$ for analysis and post-processing. This is no longer the case when using the IC corona cooling function, in part because $\dot{m}$ appears in the expression for $\mathcal{L}_{\rm code}$, as described above, but also because the very first step when using this new cooling function is to divide the disk and corona by calculating the location of the photosphere—because $\rho \propto \dot{m}$, the upper and lower photosphere surfaces move further from the midplane with increasing $\dot{m}$, decreasing the volume of the simulation space governed by the IC corona cooling function. The structure of the accretion geometry depends on the choice of $\dot{m}$.

For a chosen $\dot{m}$, however, the simulation results are still scalable with M. To see why this remains possible, consider how each term in equation 4.6 scales with M: $\rho \propto M^{-1}$ and $u_{\rm rad} \propto F_{\rm disk} \propto \mathcal{L}r \propto M^{-2}M$; therefore $\mathcal{L}_{\rm IC} \propto M^{-2}$. Thus the IC corona cooling function has the same scaling with M as does the target-temperature cooling function. The Compton temperature scales with M like so: $T_C \propto T_{\rm eff,disk} \propto (\mathcal{L}r)^{1/4} \propto M^{-1/4}$. The scaling is weak, and such that T_C *decreases* for more massive black holes. The condition for the validity of the IC cooling rate, equation 4.6, is $T_e = (m_e c^2/k)\Theta_e \gg T_C$. As discussed earlier, Θ_e is a dimensionless quantity that does not scale with M or $\dot{m}$ (it is proportional to the ratio of two quantities with identical scaling relationships, ρ and u). Therefore, because $T_e \gg T_C$ is satisfied for stellar-mass black holes (as we show below), it is necessarily satisifed for supermassive black holes.

4.3.6 Uncooled Material

The grids on which the original simulations (to which we now apply the IC cooling function) were performed are such that the polar coordinate θ is closely-spaced near the midplane—so as to better resolve the dynamics of a thin accretion disk—but is much more broadly spaced near the poles, i.e, near to the z-axis. As a consequence, the values for gas properties like density and internal energy for those cells near the poles are generally unreliable; a cooling rate calculated in the method we describe above for these cells is so influenced by invocation of the density and internal energy floors, and by poor spatial resolution, that it would be essentially meaningless. Ideally, we would use a grid for which the corona is more consistently spatially-resolved. At present, however, this is not feasible: re-running the simulations from the very start on a different grid would be prohibitively computationally expensive; in addition, interpolating the data as is onto a new grid while conserving key relationships (like $\nabla \cdot \mathbf{B} = 0$) is not a straightforward procedure. Instead, we have found through experimentation that by forcing the cooling rate to zero for those cells where the magnetic energy density is greater than the rest mass energy density [i.e., $(B^2/8\pi)/\rho c^2 > 1$; or, in code units, simply $B^2/\rho > 1$] we effectively exclude those extremely low density cells near the z-axis.

4.4 Comparison of Coronal Properties

Below we show some key results for the IC corona cooling function applied to the HARM3D $a = 0$ simulation which we post-processed in the previous chapters, for $\dot{m} = 0.01$. The new cooling function is "switched on" late enough into the simulation (after $t = 10^4 M$) that the general structure of the accretion flow is already established. This is necessary because: 1) the IC cooling rate calculation requires a well-defined disk to exist in order to locate photosphere surfaces, 2) this new corona cooling function is significantly more computationally expensive, and results in a roughly five times slower code, and 3) the target-temperature cooling function is independent of $\dot{m}$, but the IC cooling rate is not—this allows for one near steady-state "starter" simulation per spin value to be used for multiple, shorter runs with varying $\dot{m}$.

4.4.1 Cooling Rate Comparison

Figure 4.1 shows the volume-integrated cooling rate, including both disk and corona contributions, expressed in terms of the Eddington luminosity, as a function of time. The new cooling function is switched on at $t = 0$; we include for reference the prior $100M$ of the simulation, with the division between the disk and corona superimposed on the accretion flow structure, although for $t < 0$ the target-temperature cooling rate is used in all cells. Note that while such a volume integral does account for General Relativistic geometric effects, it does *not* account for either the capture of photons by the black hole nor for the difference between proper time intervals in the fluid rest frame (in which the cooling rate is defined) and the distant observer frame (for which L_{Edd} would be reasonably defined)—these effects *are* included in the PANDURATA+PTRANSX post-processing solution, however. Nevertheless, the volume-integrated cooling rate is an easy-to-evaluate estimate of the luminosity, and allows us to separate the share of total cooling in the disk and in the corona. At the instant the IC cooling function is switched on, the corona cooling rate increases sharply. After the "cooling off" period of $\approx 25M$, the simulation reaches a new near steady-state, but with a higher corona luminosity. Not surprisingly, the disk cooling—still governed by the target-temperature cooling function—hardly changes. After $100M$ of evolution with the IC cooling function in place, the total cooling increases by 65%; the share of total cooling in the corona increases from 40% to 64%.

Figure 4.2 shows the ϕ-averaged cooling rate for both the last snapshot of the simulation before the IC cooling function was switched on and after $100M$ of evolution with the new cooling function in place (with the uncooled regions masked in white), expressed in dimensionless code units. In both cases, the cooling rate generally decreases with distance from

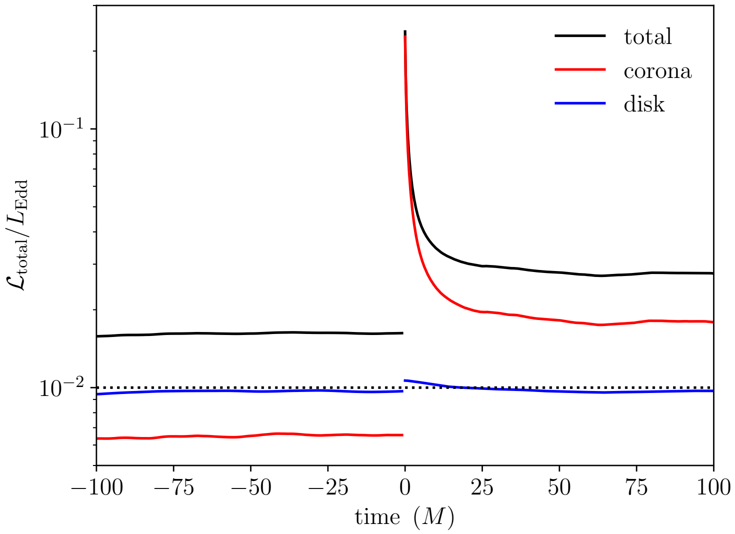

Figure 4.1: The volume-integrated corona cooling rate for the disk and corona, expressed as fractions of the Eddington luminosity, as a function of time. The target-temperature cooling function is used for both disk and corona for $t < 0$; the IC cooling function is used in the corona for $t \geq 0$. The dashed line indicates 0.01 $L_{\rm Edd}$ for reference.

the disk, and increases nearer to the black hole. Consider Figure 4.3, which shows the distribution of coronal cooling (integrated over azimuth and radius), as a function of polar angle measured from the midplane, and Figure 4.4, which shows the distribution of coronal cooling (integrated over polar angle and azimuth), as a function of radius. From these figures we see that the spatial distribution of the cooling gas for both the target-temperature cooling function and the IC cooling function is similar—for both, the cooling is mostly confined to within 40° of the midplane, but extends over a broad range in radius. With the IC cooling function, however, the coronal material cools at a higher rate everywhere.

4.4.2 T_e Comparison

As shown in Figure 4.5, however, the coronal volume within 40° of the midplane—where most of the cooling occurs—is at a lower electron temperature under the new IC corona cooling function, as compared to the old target-temperature cooling function. This shift in temperature is seen more clearly in Figure 4.6, which shows, for both cooling functions,

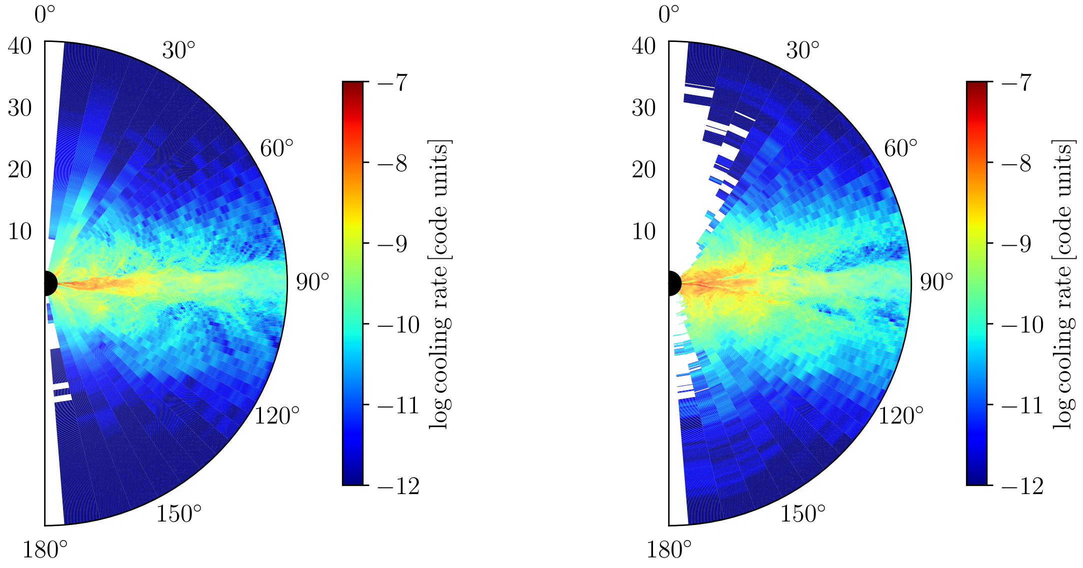

(a) target-temperature cooling function

(b) IC cooling function

Figure 4.2: Comparison of the ϕ-averaged target-temperature cooling function (left, masking uncooled regions) and IC cooling function (right) of the $a = 0$, $\dot{m} = 0.01$ simulation before switching on the IC cooling function, and at $t = +100M$, respectively.

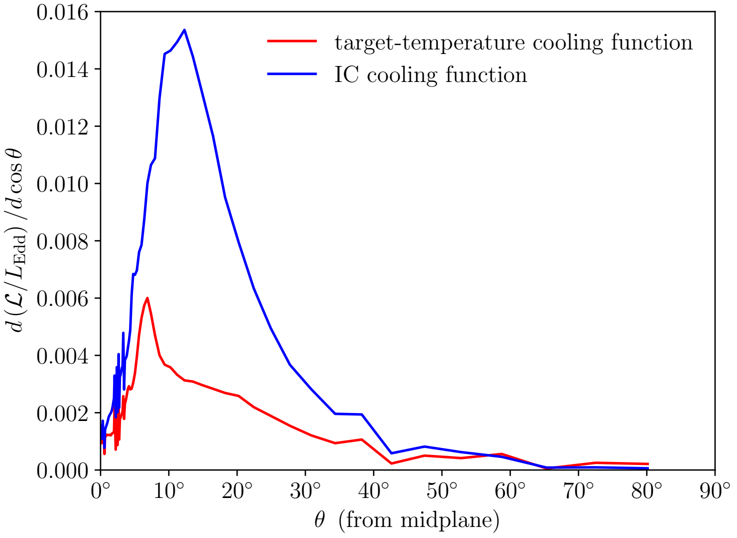

Figure 4.3: The distribution of coronal cooling (integrated over azimuth and radius) as a function of polar angle measured from the midplane, for the $a = 0$, $\dot{m} = 0.01$ simulation, both before switching on the IC cooling function and at $t = +100M$.

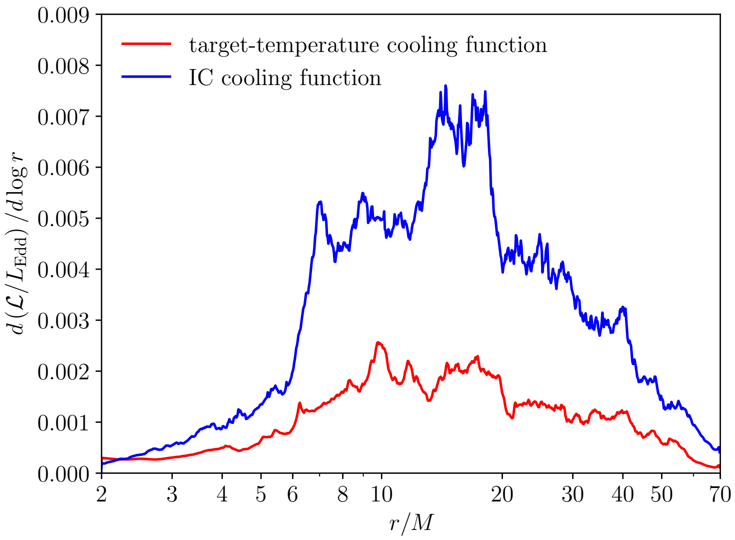

Figure 4.4: The distribution of coronal cooling (integrated over polar angle and azimuth) as a function of radius, for the $a = 0$, $\dot{m} = 0.01$ simulation, both before switching on the IC cooling function and at $t = +100M$.

how the cooling material (in the coronae only for both snapshots) is distributed in T_e: the peak of the target-temperature distribution is at ~ 200 keV, while for the IC cooling function the peak shifts down to ≈ 50 keV; while the high T_e tails are similar, the IC cooling function material does not radiate significantly at temperatures quite so high as does the target-temperature cooling function—conversely, essentially no gas radiates below 30 keV for the target-temperature snapshots, while there is some radiation from material as cool as 2–3 keV under the IC cooling function. The IC cooling function produces a corona which radiates over a broader, but generally cooler, range of T_e, but is more luminous. While being simultaneously cooler *and* brighter might at first seem counter-intuitive, recall that the target-temperature cooling function is simply a prescription designed to achieve a geometrically thin disk, and—unlike the IC cooling function—is not physically-motivated. Consider, for example, how the cooling times are set for each: in the target-temperature scheme, it is assumed that excess heat is radiated away on one orbital timescale—while this might be a more reasonable cooling timescale in the disk, the cooling time for the IC-cooled coronal material is set instead according to the local rate of electron-photon scattering

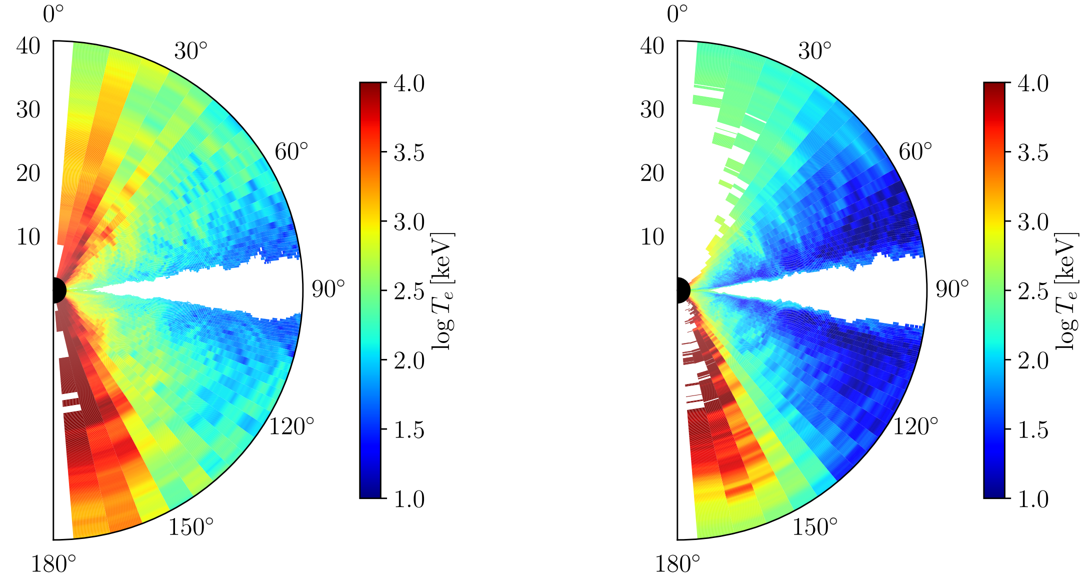

(a) target-temperature cooling function (b) IC cooling function

Figure 4.5: Comparison of the ϕ-averaged target-temperature cooling function values for T_e (left, masking uncooled regions) and IC cooling function (right) T_e values, for the $a = 0$, $\dot{m} = 0.01$ simulation before switching on the IC cooling function and at $t = +100M$.

which, of course, is the actual physical mechanism at work in real coronae. For the bulk of the coronal gas, the IC cooling time, $\lesssim$ few M, is much shorter than the orbital period, $\sim 100M$—thus the gas cools more efficiently, and thereby achieves a lower temperature in the near steady-state, with the IC cooling function in place.

4.5 Discussion

The IC corona cooling function is a significant improvement over the target-temperature cooling function. There remain, however, a few obvious possible improvements: 1) While the $B^2/\rho > 1$ criterion for not cooling the extremely low density gas near z-axis will not significantly affect the predicted X-ray spectrum (discussed in the next chapter but, in short, this gas accounts for too little of the total cooling, and is at such a high temperature that it impacts the spectrum at energies much higher than the X-ray band), the condition is necessary due to the poorly-resolved spatial grid there—it is exactly in this region, however, where

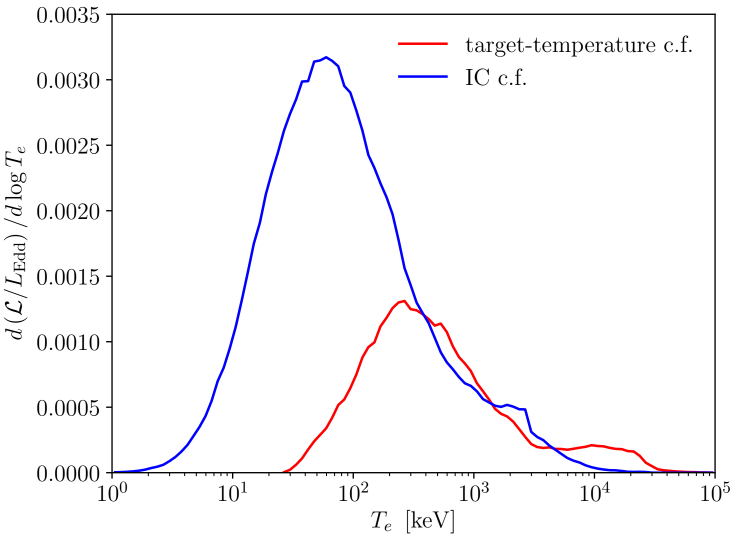

Figure 4.6: The distribution of cooling as a function of T_e, for the $a = 0$, $\dot{m} = 0.01$ simulation before switching on the IC cooling function and at $t = +100M$.

we expect jets to form, and therefore the grid as chosen is insufficiently sparse near the poles to properly resolve jet launching. In the next chapter, we apply the IC cooling function to simulations at nonzero spin—with a properly resolved jet launching region, we could make predictions about the correlation between jet strength and spin, and thereby make progress toward understanding quantitatively, through simulation, the widely-held theory that jets are powered through the extraction of black hole spin energy (Blandford and Znajek, 1977). 2) We have assumed "fast-light" in deriving the IC cooling function, i.e., we do not account for the light-travel time between the disk surface and a given corona cell when calculating the IC cooling rate. This is a reasonable approximation for simulations we will use to make predictions for the time-integrated X-ray spectrum; for predicting light curves, however, time lags between disk and corona can be important for the study of high-frequency quasi-periodic oscillations (QPOs) [see Motta (2016) for a recent, brief review] and in particular they underpin the field of reverberation mapping (Bentz, 2015). Introducing time-dependent calculation of the radiation energy density in the corona would allow us to use these simulations to uncover the physical mechanism behind QPOs [of which there is much debate

(Schnittman, 2005)], and to comment on the validity of the assumptions which underlie reverberation mapping techniques. And 3), we neglect special and General Relativistic corrections to the radiation energy density calculation—as we show in the next chapter, a more careful calculation with PANDURATA reveals that, with the $T_e = T_i$ assumption in place, the resulting error from ignoring these effects is small; in Chapter 6, however, we see that when the Compton temperature is of the same order of magnitude as T_e, failure to account for relativistic effects results in systematic underestimation of the electron temperature. Accounting for gravitational redshift and special relativistic boosting is a fairly straightforward fix, at least in principle—accounting for the bending of light in curved spacetime, however, will prove more difficult.

In addition to relaxing the assumptions behind our calculation of u_{rad}, there is another obvious target for improvement: just as we have replaced the target-temperature cooling function in the corona with one which treats the same physics as PANDURATA, we imagine replacing the cooling function in the disk (still target-temperature in the simulations shown in this and all chapters) with a PTRANSX-inspired cooling function. In the disk, an "optically thin" cooling function is not an accurate description—the effective net rate at which gas cools is a function of its (total optical) depth from the disk photospheres, and is therefore an *extensive* physical property; also, in the cooler, denser disk, radiative mechanisms beyond Compton scattering, such as bremsstrahlung and photoionization, are significant. Incorporating such physics into the disk cooling function, however difficult it may be, will finally enable us to remove the last remnants of the *ad hoc* equation of state from these simulations, leaving us with a realistic and physically-founded picture of black hole accretion dynamics.

References

Jiang, Y.-F., J. M. Stone, and S. W. Davis (2014a). "An Algorithm for Radiation Magnetohydrodynamics Based on Solving the Time-dependent Transfer Equation". In: *ApJS* 213, 7, p. 7. DOI: `10.1088/0067-0049/213/1/7`. arXiv: `1403.6126 [astro-ph.IM]`.

Jiang, Yan-Fei, James M. Stone, and Shane W. Davis (2014b). "A Global Three-dimensional Radiation Magneto-hydrodynamic Simulation of Super-Eddington Accretion Disks". In: *ApJ* 796.2, 106, p. 106. DOI: `10.1088/0004-637X/796/2/106`. arXiv: `1410.0678 [astro-ph.HE]`.

Jiang, Yan-Fei, James Stone, and Shane W. Davis (2017). "Super-Eddington Accretion Disks around Supermassive black Holes". In: *arXiv e-prints*, arXiv:1709.02845, arXiv:1709.02845. arXiv: `1709.02845 [astro-ph.HE]`.

Jiang, Yan-Fei, Omer Blaes, James Stone, and Shane W. Davis (2019). "Global Radiation Magneto-hydrodynamic Simulations of Sub-Eddington Accretion Disks around Supermassive Black Holes". In: *arXiv e-prints*, arXiv:1904.01674, arXiv:1904.01674. arXiv: `1904.01674 [astro-ph.HE]`.

Zanotti, O., C. Roedig, L. Rezzolla, and L. Del Zanna (2011). "General relativistic radiation hydrodynamics of accretion flows - I. Bondi-Hoyle accretion". In: *MNRAS* 417.4, pp. 2899–2915. DOI: `10.1111/j.1365-2966.2011.19451.x`. arXiv: `1105.5615 [astro-ph.HE]`.

Roedig, C., O. Zanotti, and D. Alic (2012). "General relativistic radiation hydrodynamics of accretion flows - II. Treating stiff source terms and exploring physical limitations". In: *MNRAS* 426.2, pp. 1613–1631. DOI: `10.1111/j.1365-2966.2012.21821.x`. arXiv: `1206.6662 [astro-ph.HE]`.

Sądowski, A., R. Narayan, J. C. McKinney, and A. Tchekhovskoy (2014). "Numerical simulations of super-critical black hole accretion flows in general relativity". In: *MNRAS* 439, pp. 503–520. DOI: `10.1093/mnras/stt2479`. arXiv: `1311.5900 [astro-ph.HE]`.

Fragile, P. Chris, Anna Gillespie, Timothy Monahan, Marco Rodriguez, and Peter Anninos (2012). "Numerical Simulations of Optically Thick Accretion onto a Black Hole. I. Spherical Case". In: *ApJS* 201.2, 9, p. 9. DOI: `10.1088/0067-0049/201/2/9`. arXiv: `1204.5538 [astro-ph.IM]`.

Fragile, P. Chris, Ally Olejar, and Peter Anninos (2014). "Numerical Simulations of Optically Thick Accretion onto a Black Hole. II. Rotating Flow". In: *ApJ* 796.1, 22, p. 22. DOI: `10.1088/0004-637X/796/1/22`. arXiv: `1408.4460 [astro-ph.IM]`.

McKinney, Jonathan C., Alexander Tchekhovskoy, Aleksander Sadowski, and Ramesh Narayan (2014). “Three-dimensional general relativistic radiation magnetohydrodynamical simulation of super-Eddington accretion, using a new code HARMRAD with M1 closure”. In: *MNRAS* 441.4, pp. 3177–3208. DOI: `10.1093/mnras/stu762`. arXiv: `1312.6127 [astro-ph.CO]`.

Sądowski, Aleksander, Emilio Tejeda, Emanuel Gafton, Stephan Rosswog, and David Abarca (2016). “Magnetohydrodynamical simulations of a deep tidal disruption in general relativity”. In: *MNRAS* 458.4, pp. 4250–4268. DOI: `10.1093/mnras/stw589`. arXiv: `1512.04865 [astro-ph.HE]`.

Rybicki, G. B. and A. P. Lightman (1986). *Radiative Processes in Astrophysics*, p. 400.

Noble, S. C., J. H. Krolik, and J. F. Hawley (2009). “Direct Calculation of the Radiative Efficiency of an Accretion Disk Around a Black Hole”. In: *ApJ* 692, pp. 411–421. DOI: `10.1088/0004-637X/692/1/411`. arXiv: `0808.3140`.

Noble, S. C., J. H. Krolik, and J. F. Hawley (2010). “Dependence of Inner Accretion Disk Stress on Parameters: The Schwarzschild Case”. In: *ApJ* 711, pp. 959–973. DOI: `10.1088/0004-637X/711/2/959`. arXiv: `1001.4809 [astro-ph.HE]`.

Noble, S. C., J. H. Krolik, J. D. Schnittman, and J. F. Hawley (2011). “Radiative Efficiency and Thermal Spectrum of Accretion onto Schwarzschild Black Holes”. In: *ApJ* 743, 115, p. 115. DOI: `10.1088/0004-637X/743/2/115`. arXiv: `1105.2825 [astro-ph.HE]`.

Abramowicz, M. A., A. Lanza, and M. J. Percival (1997). “Accretion Disks around Kerr Black Holes: Vertical Equilibrium Revisited”. In: *ApJ* 479.1, pp. 179–183. DOI: `10.1086/303869`.

Blumenthal, George R. and Robert J. Gould (1970). “Bremsstrahlung, Synchrotron Radiation, and Compton Scattering of High-Energy Electrons Traversing Dilute Gases”. In: *Reviews of Modern Physics* 42.2, pp. 237–271. DOI: `10.1103/RevModPhys.42.237`.

Mignone, A. and Jonathan C. McKinney (2007). “Equation of state in relativistic magnetohydrodynamics: variable versus constant adiabatic index”. In: *MNRAS* 378.3, pp. 1118–1130. DOI: `10.1111/j.1365-2966.2007.11849.x`. arXiv: `0704.1679 [astro-ph]`.

Novikov, I. D. and K. S. Thorne (1973). “Astrophysics of black holes.” In: *Black Holes (Les Astres Occlus)*. Ed. by C. Dewitt and B. S. Dewitt, pp. 343–450.

Blandford, R. D. and R. L. Znajek (1977). “Electromagnetic extraction of energy from Kerr black holes”. In: *MNRAS* 179, pp. 433–456.

Motta, S. E. (2016). “Quasi periodic oscillations in black hole binaries”. In: *Astronomische Nachrichten* 337.4-5, p. 398. DOI: `10.1002/asna.201612320`. arXiv: `1603.07885 [astro-ph.HE]`.

Bentz, Misty C. (2015). “AGN Reverberation Mapping”. In: *arXiv e-prints*, arXiv:1505.04805, arXiv:1505.04805. arXiv: `1505.04805 [astro-ph.GA]`.

Schnittman, Jeremy D (2005). “Interpreting the High-Frequency Quasi-periodic Oscillation Power Spectra of Accreting Black Holes”. In: *ApJ* 621.2, pp. 940–950. DOI: `10.1086/427646`. URL: `https://doi.org/10.1086{\%}2F427646`.

Chapter 5

Spin Survey

In this chapter, we apply the IC corona cooling function developed in the previous chapter to four simulations, each with the same $10M_\odot$ central black hole and scaled to $\dot{m} = 0.01$, but with increasing spin, from $a/M = 0$ to $a/M = 0.99$. As discussed in the Introduction and in Chapters 2 and 3, there have been attempts to infer the spin of black holes, both stellar-mass (like we consider here) and supermassive, for at least two decades. At their core, the various methods all require fitting model X-ray spectra to the observed X-ray spectral data, and these models rely on a (varyingly) idealized description of the black hole accretion flow geometry and a highly simplified model of the coronal illumination pattern. Here we examine, with the aid of our more realistic depiction of the accretion flow from HARM3D and the PANDURATA+PTRANSX post-processing apparatus, predictions for how we expect both the X-ray continuum and the Fe Kα emission line profile to vary with spin, holding other parameters (mass, accretion rate, and elemental abundances) constant. We will also verify the consistency of the simplified u_{urad} calculation in HARM3D against the special and General Relativistically correct PANDURATA calculation by showing that the equilibrium T_e values found by the latter agree with those from the former.

5.1 IC Cooling Rate

Below we show some key results for the IC corona cooling function applied to four HARM3D simulations, each with $\dot{m} = 0.01$ and for dimensionless spin values $a/M = 0$, 0.5, 0.9, and

0.99. (For what follows, we refer to the dimensionless spin $a_* = a/M$ as simply the "spin" a.) The starting point for these simulations are those described in Noble et al. (2011); the $a = 0$ version of which was the data post-processed in Chapters 2 and 3, and for which we studied the IC corona cooling function vs. the target-temperature cooling function in the last chapter. As in the last chapter, we use Novikov and Thorne (1973) values for the nominal radiative efficiency required when specifying a particular $\dot{m}$: for the spins we survey, these are $\eta_{\rm NT} = 0.0572$, 0.0821, 0.1558, and 0.2640, in order of increasing spin—the analytic radiative efficiencies increase with increasing spin simply because the radius of the ISCO moves nearer to the black hole. We switch on the IC cooling function after $t \geq 10^4 M$ (later for higher spin) so that the accretion flow is in a near steady-state.

As we did for the $a = 0$ case in the previous chapter, each simulation is run for $100M$ after switching on the IC cooling rate function. Figure 5.1 shows the volume-integrated cooling rate for each case, including both disk and corona contributions, expressed in terms of the Eddington luminosity. In order of increasing spin, the share of total cooling in the corona is 64%, 71%, 87%, and 85%. In general, the corona accounts for an increased share of the total cooling as spin increases, but not monotonically—the first instance of a trend we will observe repeatedly throughout this chapter. For the remaining analysis of the HARM3D simulation data, and for the post-processed results following, we examine snapshots of each simulation at $t = +100M$.

As can be seen from the curves of Figure 5.1, there is greater short-time variability with increasing spin. For the $a = 0.99$ simulation in particular, there is a high degree of temporal variability, making conclusions drawn from only a single snapshot suspect at best. Due to the large amplitude turbulence in the accretion flows, a single snapshot cannot tell the whole story. In addition, because the post-processing procedure is certainly a *nonlinear* function of the underlying simulation input, we cannot simply time-average the simulation data and then post-process that. To do this properly, we would extract snapshots from the original, target-temperature simulation at relatively widely-spaced points in time, switch on the IC cooling

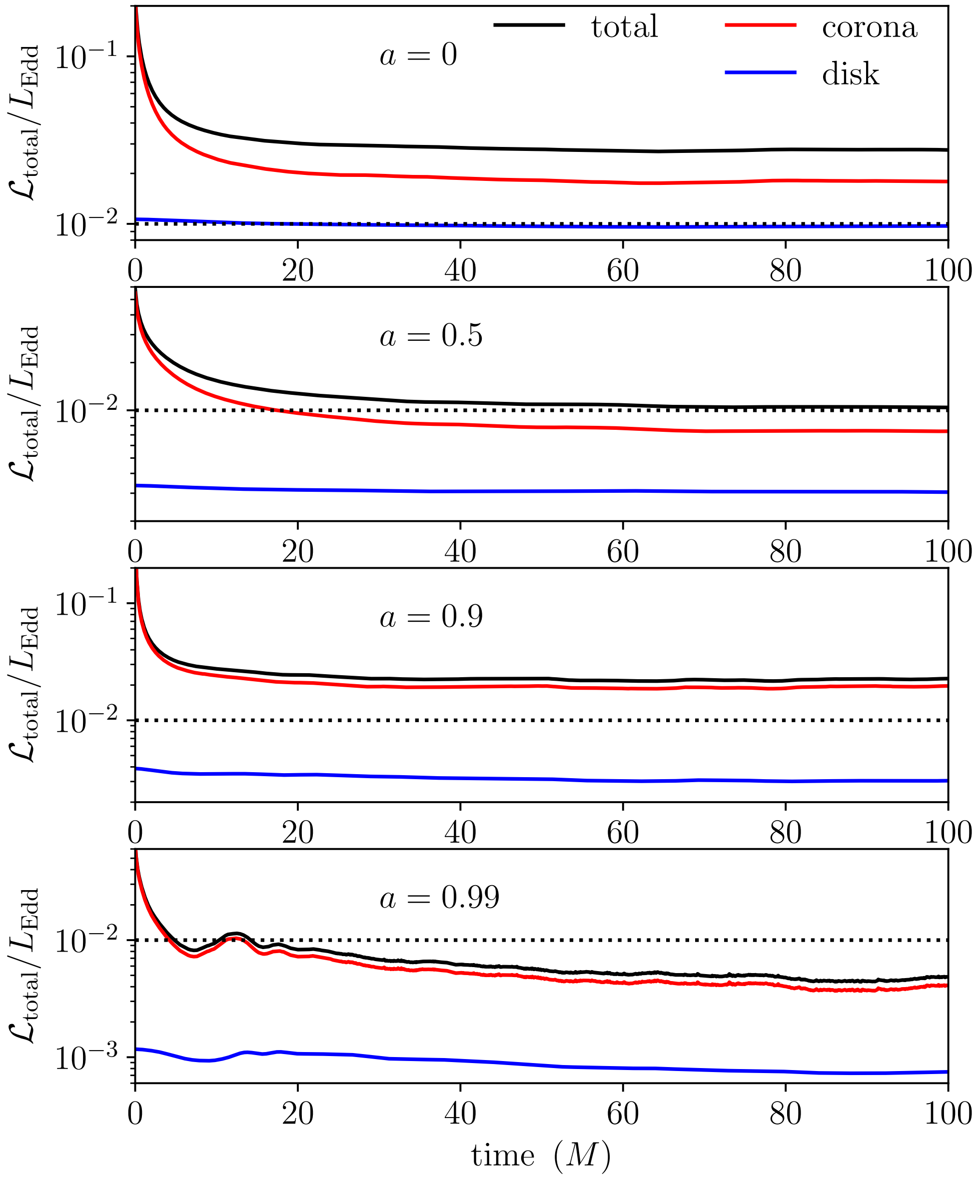

Figure 5.1: The volume-integrated coronal (IC) cooling rates, disk (target-temperature) cooling rates, and total cooling rates, expressed as fractions of the Eddington luminosity, as a function of time, for each of the four spins. The dashed lines indicate 0.01 $L_{\rm Edd}$ for reference.

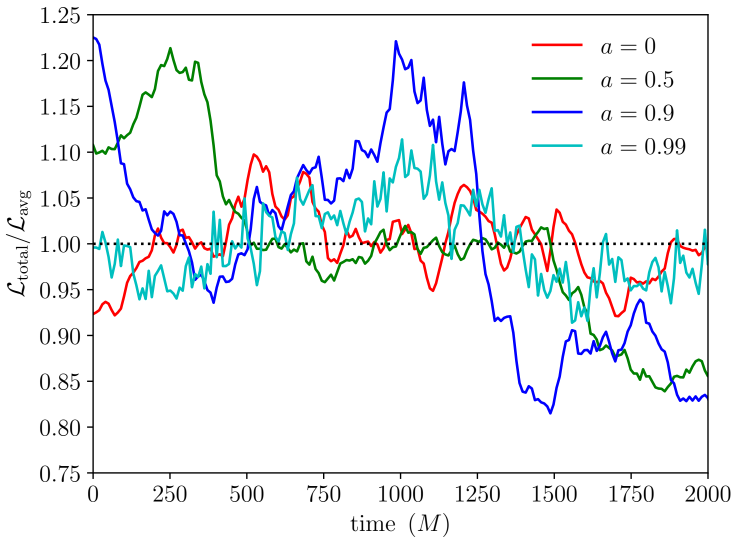

Figure 5.2: The volume-integrated total target-temperature cooling rates, expressed as ratios to their mean value for the time range shown, as a function of time, for each of the four spins.

function and run until it "settles down," post-process the simulation output from many such runs, and average *those* results. This is not computationally feasible at the present time, and so we are limited to our single snapshot analysis, keeping in mind that they might not be representative of the properly-averaged spectra. Figures 5.2 and 5.3 provide a sense for the time-variability: the former shows the total volume-integrated cooling rate as a function of time, and the latter shows the azimuthally- and polar angle-integrated mass accretion rate at $r = 10M$, both expressed in terms of ratios to the mean value over the range shown. The data for both figures are the $2000M$ of time evolution, with the target-temperature cooling function applied everwhere, starting from the same snapshot at which we first switch on the IC cooling function. Clearly there is significant time variability, with the more locally defined quantity ($\dot{M}(r = 10M)$) showing, not surprisingly, a larger degree of variation. From Figure 5.3 we see that the $a = 0.99$ simulation has both more rapid and higher amplitude variability than does the $a = 0$ simulation—the solid angle-integrated accretion rate even goes negative at times for the $a = 0.99$ simulation, indicating an occasional net outflow.

Figure 5.4 shows the ϕ-averaged cooling rate for each spin (for a snapshot at $t = +100M$),

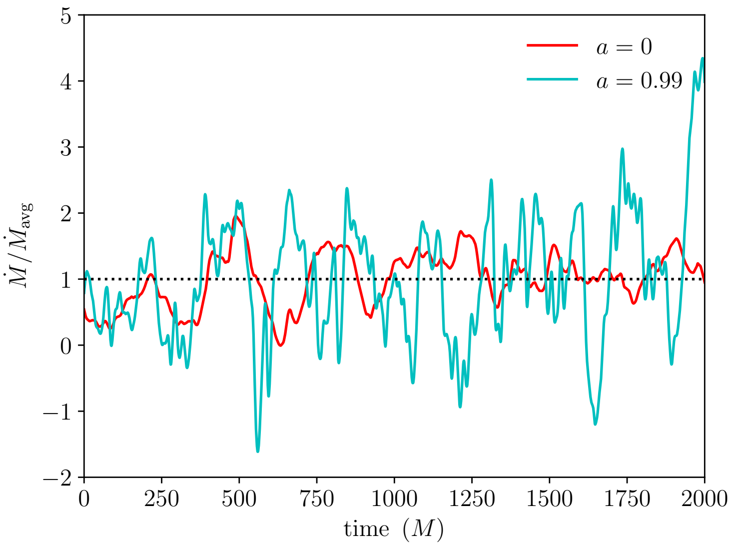

Figure 5.3: The ϕ- and θ-integrated mass accretion rate measured at $r = 10M$, expressed as ratios to their mean value for the time range shown, as a function of time, for $a = 0$ and $a = 0.99$. The other two spin cases are excluded to ease comparison between the two extreme cases.

for both corona and disk, expressed in dimensionless code units, with the uncooled gas regions (where $B^2/\rho > 1$) masked. As the spin increases, a larger swath of gas near the z-axis satisfies $B^2/\rho > 1$, and is therefore not cooled. Consider Figure 5.5, which shows the distribution of cooling (integrated over azimuth and radius) as a function of polar angle measured from the midplane. For each spin value, most of the cooling is contained within 40° of the midplane; this material rarely ever satisfies $B^2/\rho > 1$, and is therefore always properly cooled. Also evident in this figure, however, is that as the spin increases, the few broadly-spaced cells near the z-axis which do not satisfy $B^2/\rho > 1$ (but are typically close to it) take on a larger portion of the cooling. These cells, however, account for a very small portion of the total mass budget of the accretion flow, as shown in Figure 5.6. While the poorly-resolved spatial grid near the z-axis means that the simulation values for ρ there are likely dubious (due, for example, to numerical diffusion—the density drops by a factor of several-to-ten from to cell-to-cell for the last few θ cells approaching the poles), it can be confidently stated that they are *very* low. Physically, there is a large centrifugal barrier to overcome for any material with nonzero angular momentum. Cells in those regions, then, which just marginally fail to satisfy $B^2/\rho > 1$ and are in fact cooled, will do so at very high temperatures, $T_e \gtrsim 1$ MeV (see Figures 5.8–5.11 and the discussion below), and will therefore not affect our X-ray spectral predictions for considerably lower energy spectral bands (1–100 keV).

Consider also Figure 5.7, which shows the distribution of coronal cooling (integrated over polar angle and azimuth), as a function of radius, for each spin value. There is not much of a discernible trend with spin in the radial distribution of cooling: as has been evident from all figures presented so far in this chapter, the $a = 0$ and $a = 0.9$ snapshots are more luminous than the others; in addition, the $a = 0.9$ and $a = 0.99$ simulations have significant cooling even at large radii near the boundary of the simulation volume at $r = 70M$, with the $a = 0.99$ snapshot showing a (noisy) jump after $r = 50M$; overall, however, for all four spin values there is a broad radial distribution in coronal cooling.

5.2 Post-processing: Continuum

The application of PANDURATA+PTRANSX to HARM3D output of simulations run with the IC corona cooling function proceeds in the same fashion as described in Chapter 3.

First, we consider the equilibrium electron temperature in the corona as re-determined by PANDURATA. Figures 5.8–5.11 are side-by-side comparisons of T_e from HARM3D and T_e as found by PANDURATA for each spin value. They agree rather well, which indicates that the assumptions enumerated in section 4.3.2, made so that determining $u_{\rm rad}$ each timestep is computationally feasible for HARM3D, do not appreciably impact the validity of the IC corona cooling function as implemented—all but for the "fast light" approximation: PANDURATA makes this assumption as well. Recall from Chapter 3 that PANDURATA's T_e-finding scheme requires a relatively significant coarsening of the coronal volume—groups of ~ 100 cells on HARM3D's grid are combined into PANDURATA's "sectors," a procedure which makes it possible to achieve reliable Monte Carlo statistics in a reasonable amount of time; in

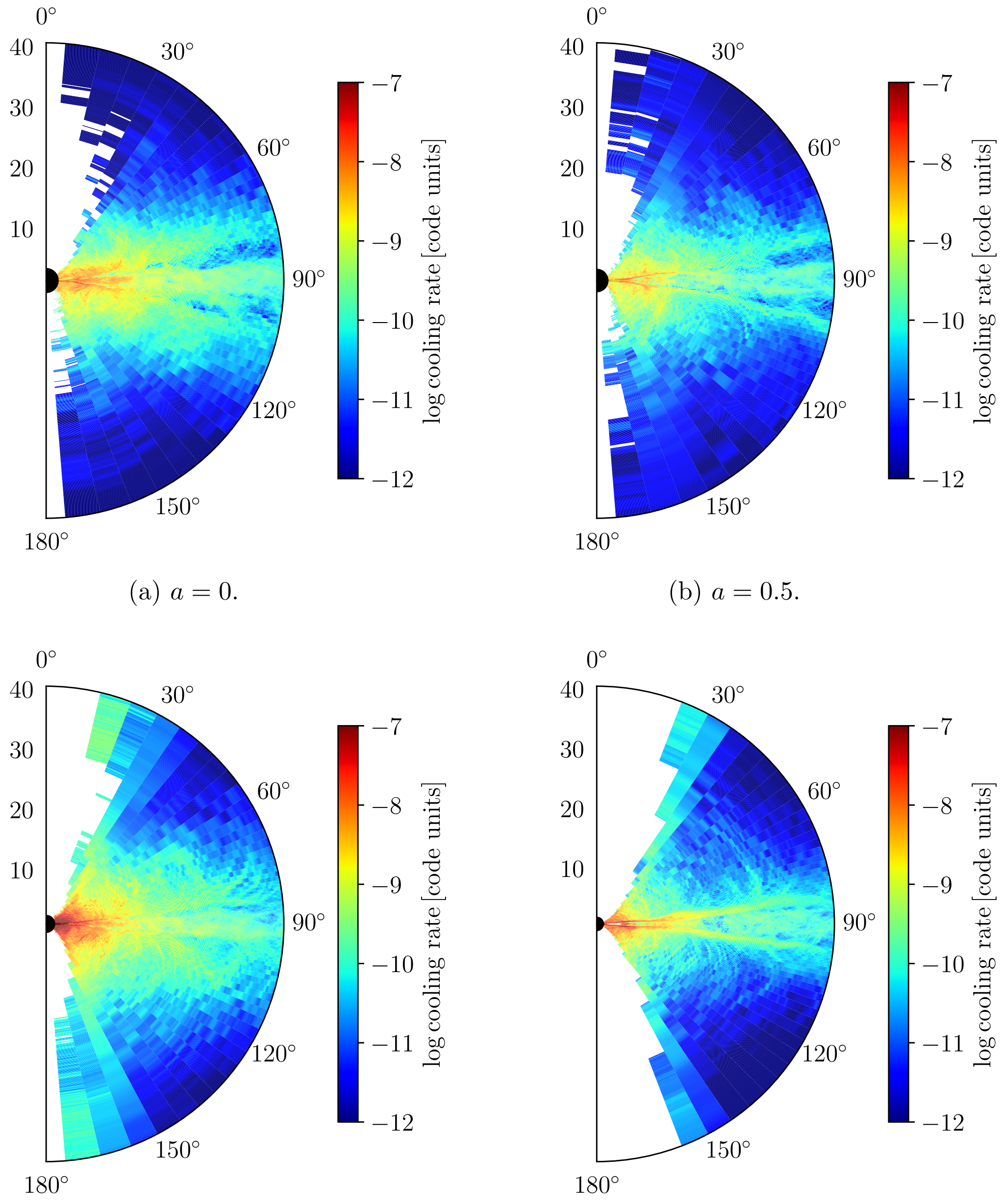

(a) $a = 0$.

(b) $a = 0.5$.

(c) $a = 0.9$.

(d) $a = 0.99$.

Figure 5.4: Snapshots of the ϕ-averaged cooling rate, in code units, for the $\dot{m} = 0.01$ simulations at $t = +100M$. The uncooled material is masked (in white).

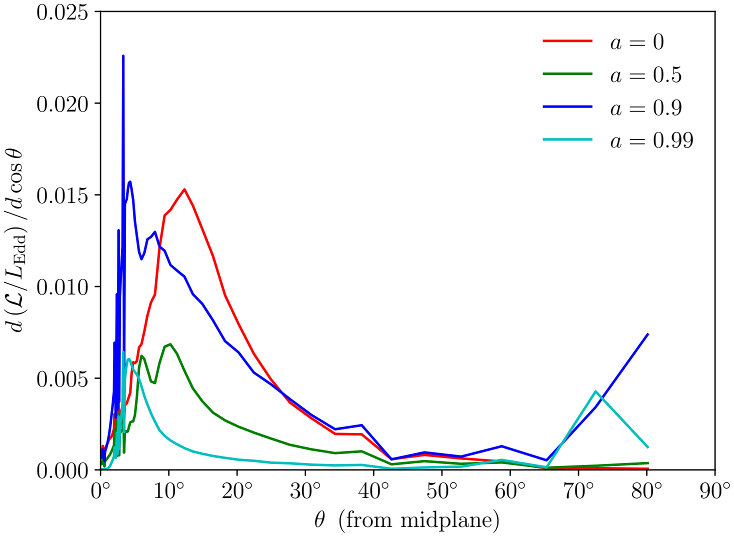

Figure 5.5: The distribution of cooling (integrated over azimuth and radius) as a function of polar angle measured from the midplane, for the $\dot{m} = 0.01$ simulations at $t = +100M$.

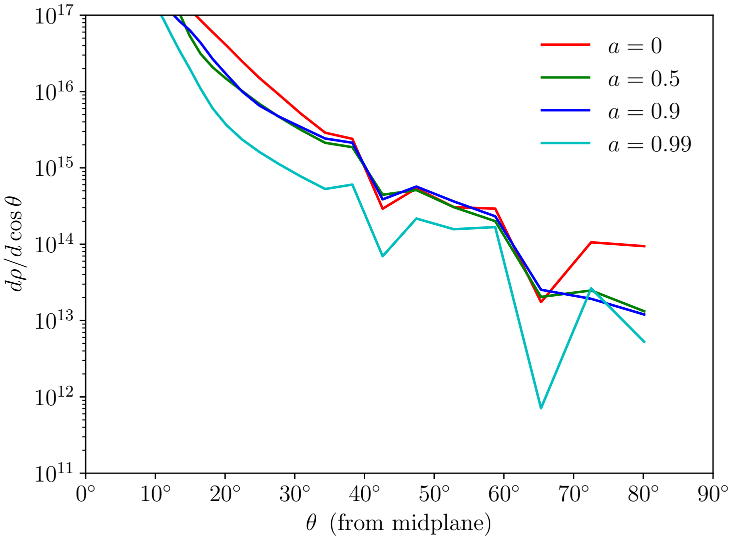

Figure 5.6: The distribution of accreting gas mass (integrated over azimuth and radius) as a function of polar angle measured from the midplane, for the $\dot{m} = 0.01$ simulations at $t = +100M$. Note that the y-axis scale is logarithmic, and that the vast majority of matter is in the disk at angles less than 10° from the midplane (not shown for the limits chosen).

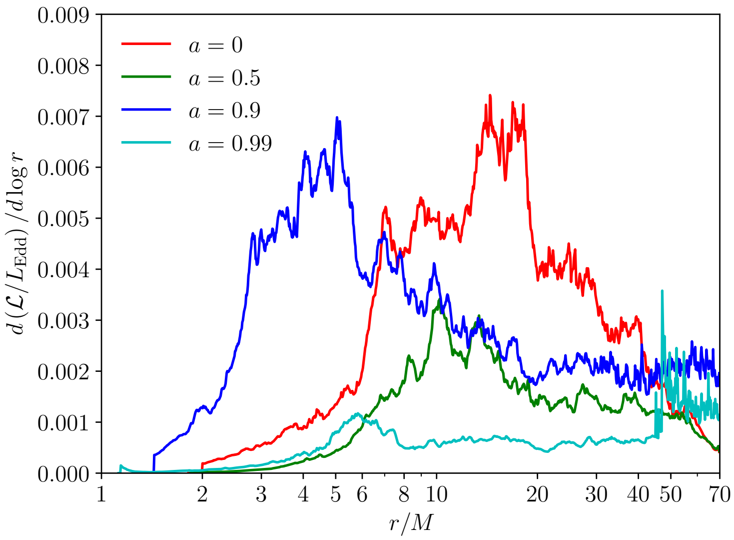

Figure 5.7: The distribution of coronal cooling (integrated over polar angle and azimuth) as a function of radius, for the $\dot{m} = 0.01$ simulations at $t = +100M$.

practice, this amounts to a smoothing procedure, which accounts for the lower point-to-point variation in the PANDURATA T_e plots compared to those from HARM3D. Beyond that, the greatest discrepancy between the HARM3D and PANDURATA T_e maps is in the thin layer immediately outside the photosphere: HARM3D finds a higher T_e for the same cooling rate, indicating that it therefore determines a lower $u_{\rm rad}$ than does PANDURATA; PANDURATA includes the effect of relativistic beaming and HARM3D does not, so PANDURATA's seed photons launch preferentially at smaller angles with respect to the (rapidly spinning) disk, while HARM3D assumes the disk radiates isotropically—thus HARM3D tends to underestimate $u_{\rm rad}$ in the immediate vicinity of the disk surface. In addition, PANDURATA *does* account for the increased intervening material for coronal cells further from the disk surface, as it directly simulates scattering—corona layers near to the disk, then, are expected to have a relatively higher $u_{\rm rad}$ compared to those further from the disk in PANDURATA's calculation. Note that regions where the HARM3D coronal cooling rate is zeroed-out because $B^2/\rho > 1$ will cause PANDURATA to find the equilibrium temperature which results in zero net cooling, i.e., the Compton temperature.

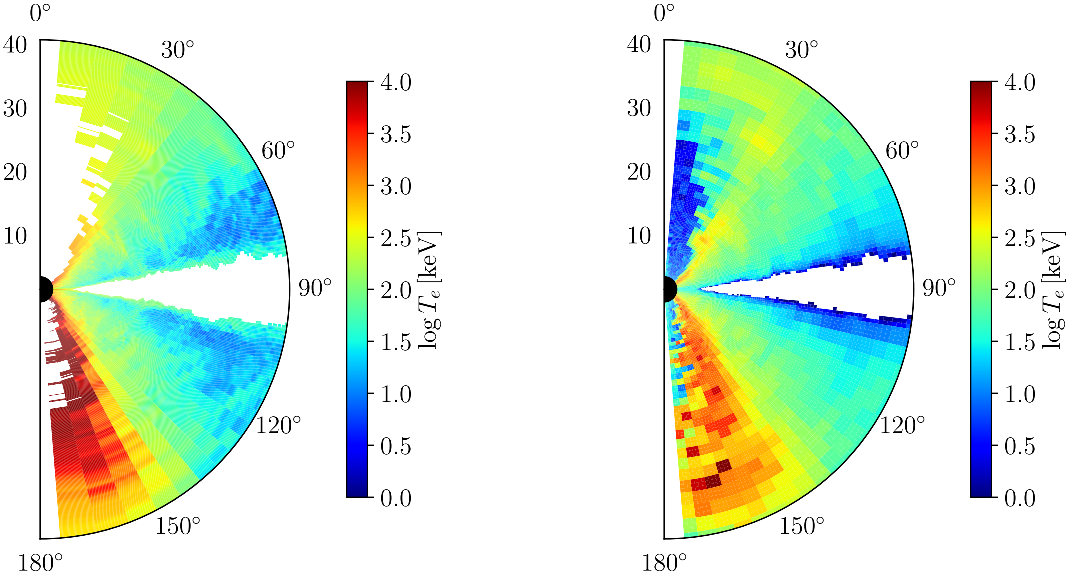

(a) HARM3D

(b) PANDURATA+PTRANSX

Figure 5.8: Comparison of the ϕ-averaged T_e, as found by HARM3D (left, masking uncooled regions) and PANDURATA+PTRANSX (right), for the post-processed snapshot of the $a = 0$, $\dot{m} = 0.01$ simulation at $t = +100M$.

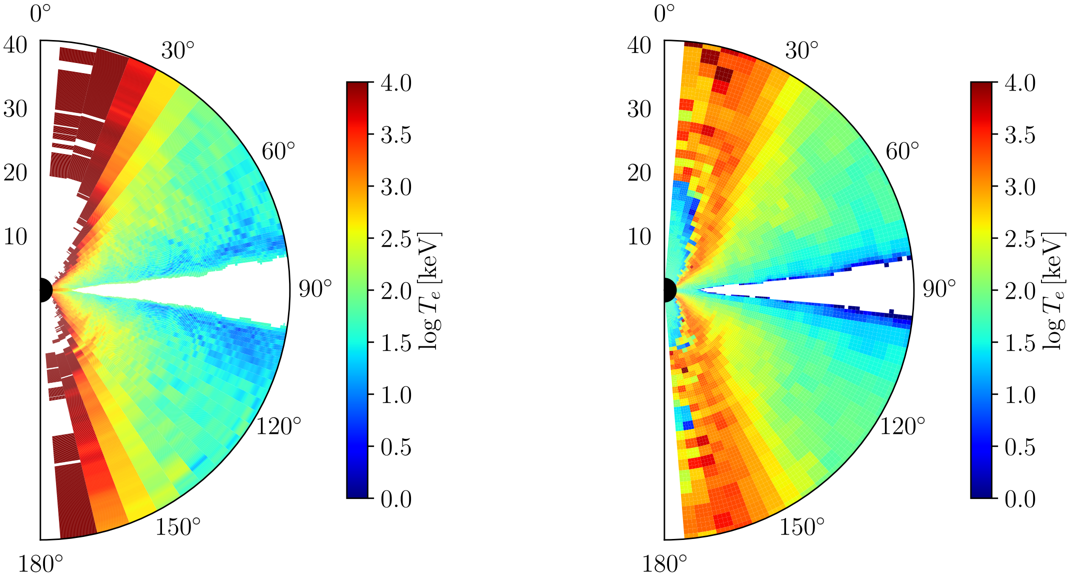

(a) HARM3D

(b) PANDURATA+PTRANSX

Figure 5.9: Like Figure 5.8, but for the $a = 0.5$, $\dot{m} = 0.01$ simulation at $t = +100M$.

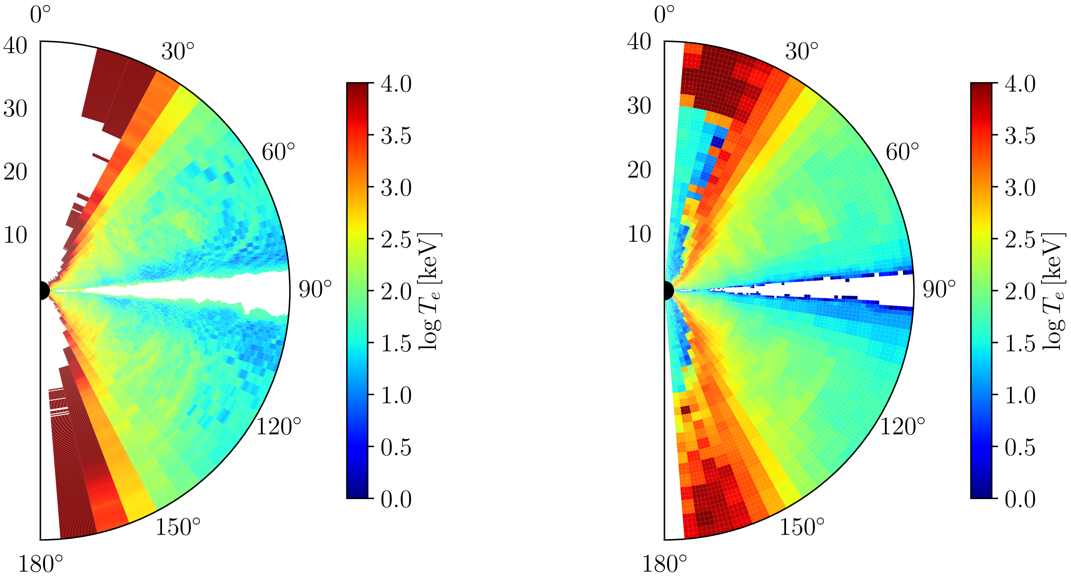

(a) HARM3D (b) PANDURATA+PTRANSX

Figure 5.10: Like Figure 5.8, but for the $a = 0.9$, $\dot{m} = 0.01$ simulation at $t = +100M$.

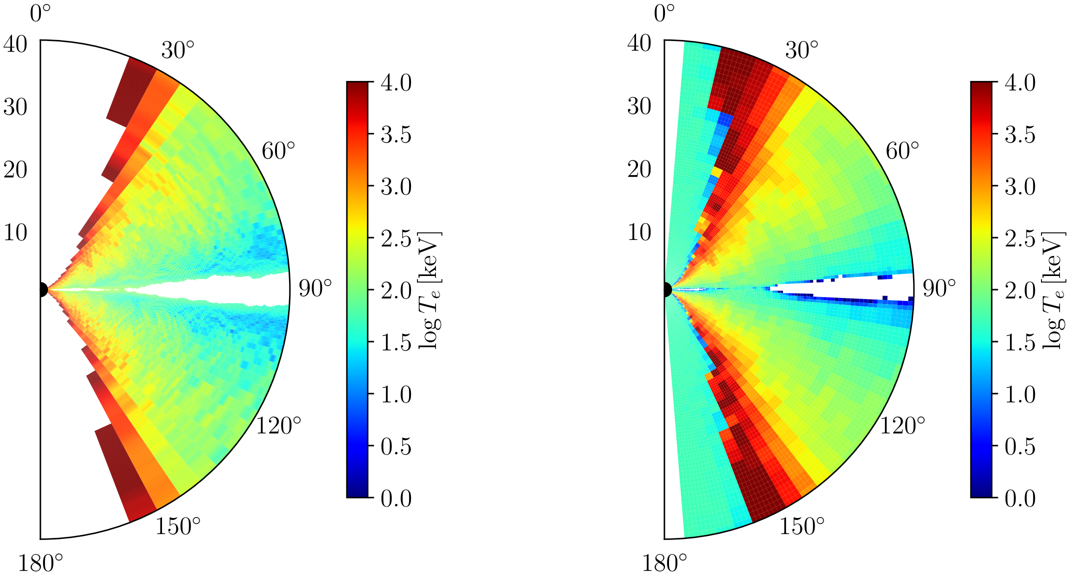

(a) HARM3D (b) PANDURATA+PTRANSX

Figure 5.11: Like Figure 5.8, but for the $a = 0.99$, $\dot{m} = 0.01$ simulation at $t = +100M$.

Figure 5.12 shows the broadband spectral luminosity (νL_ν) as predicted by PANDURATA+PTRANSX, for each spin. As shown in Figure 5.13, the photon index as measured over 2–80 keV generally decreases with spin, though it is actually higher for $a = 0.99$ (at most viewing angles) than for $a = 0.9$; nevertheless, there is a general trend of the X-ray continuum hardening with increasing spin. The shape of the X-ray continuum changes with spin as well: the hump at ~ 100 keV becomes larger. The rising hump is due to a larger portion of the cooling occurring at higher temperatures (see Figure 5.14 below), both because thermal seed photons are more likely to scatter to higher energies directly, and because the resulting harder spectrum impinging on the disk causes a more substantial Compton reflection effect. These changes in shape are most dramatic between $a = 0$ to $a = 0.5$, and from $a = 0.5$ to $a = 0.9$—the difference in shape between the $a = 0.9$ and $a = 0.99$ spectra is much smaller. Also note that the spectra appears harder when viewing the disk edge-on, due to two effects: those photons which reach the distant observer along a trajectory nearly parallel to the disk surface must pass through a larger optical depth of hot electrons (cf. Figures 5.5 and 5.8–5.11), providing more opportunities for scattering to high energies (and thus hardening the spectrum); and, relativistic beaming tends to direct more thermal seed photons, and boost them to higher energies, for lines of sight more nearly parallel to the plane of the disk surface.

$L/L_{\rm Edd}$, as computed by PANDURATA for the distant observer, is 2.5%, 1.0%, 1.5%, and 0.37%, for spin values of $a = 0$, 0.5, 0.9 and 0.99, respectively. These are near to the nominal 1% $L_{\rm Edd}$ we expect from our choice of $\dot{m} = 0.01$, but, as discussed in section 4.3.5, $\dot{m} = 0.01$ results in a luminosity of 0.01 $L_{\rm Edd}$ only if the actual radiative efficiency of the simulation matches the nominal radiative efficiency, $\eta_{\rm NT}$, assumed for scaling from dimensionless code units to cgs units. In our calculation—for these specific snapshots in time—we find that the $\eta_{\rm NT}$ values underestimate the radiative efficiency for spins $a = 0$ and $a = 0.9$, are a very good match for $a = 0.5$, and overestimate the efficiency for $a = 0.99$.

The shape of the broadband X-ray continuum is determined both by the distribution-in-space and the distribution-in-temperature of the hot electrons off which the thermal seed

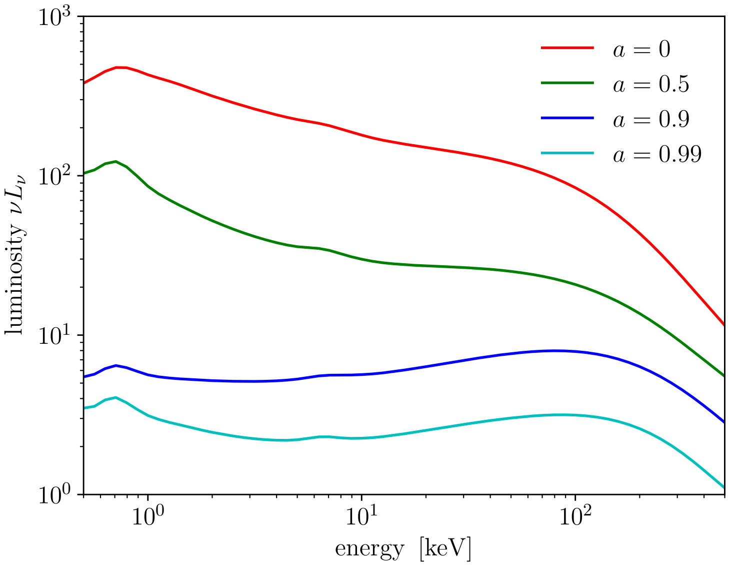

Figure 5.12: The spectral luminosity for the four spin values considered, each with $\dot{m} = 0.01$ at $t = +100M$. The y-axis scaling is arbitrary—the curves are adjusted vertically for ease of comparison.

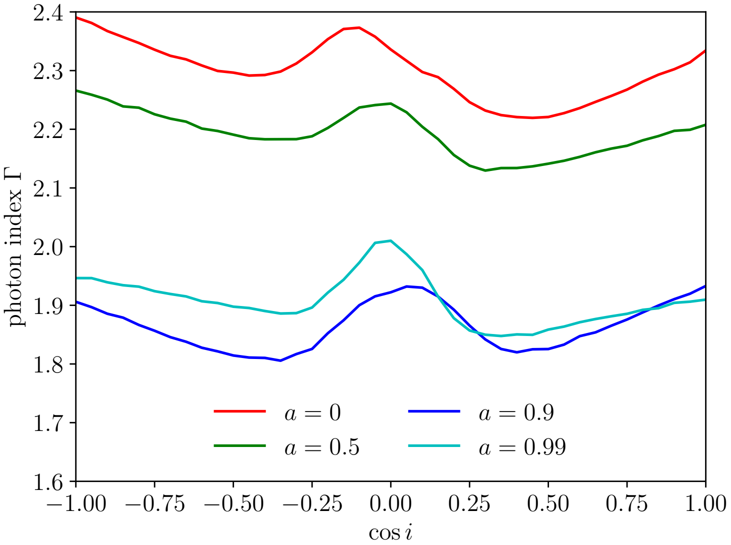

Figure 5.13: The photon index measured between 2–80 keV as a function of observer inclination angle (where $i = 0°$ is a face-on view of the disk) for the four spin values considered.

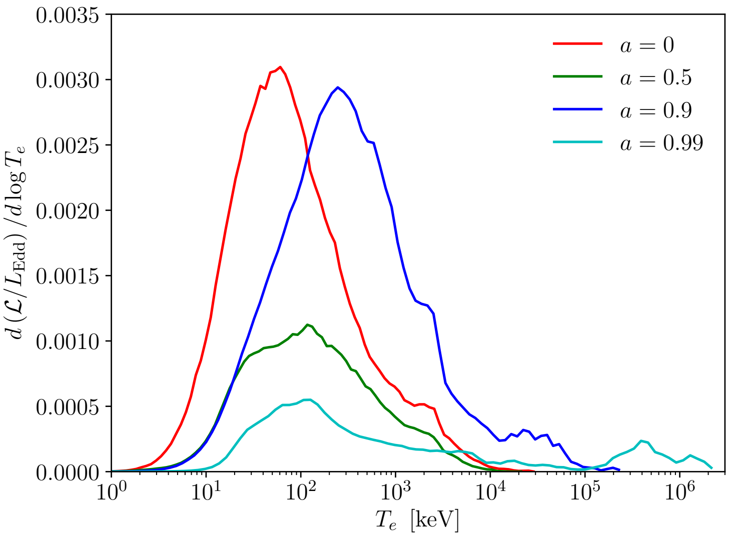

Figure 5.14: The distribution of IC power as a function of electron temperature in the corona for the four spin cases considered.

photons scatter before traveling to the distant observer. Figure 5.14 shows the latter: as the spin increases, the peak of the distribution moves to higher temperatures (except, curiously, for $a = 0.99$, where the peak is cooler than it is for $a = 0.9$); for all spin cases, the distribution is very broad, with significant cooling occuring for gas differing in temperature by 2–3 orders of magnitude. The extremely hot tail observed for the $a = 0.99$ case only is located near the boundary of the uncooled region—as discussed above, it is gas for which B^2/ρ is only marginally less than unity, and it does not contribute significantly to the predicted X-ray continuum spectrum below 100 keV.

5.3 Post-processing: Fe Kα

As discussed in Chapter 3, PANDURATA allows for the separate identification of line (primarily Fe Kα emission) photons from continuum photons, obviating the need for continuum-fitting techniques. While this is particularly useful for understanding the physical processes behind line photon production and transport, an actual continuum-fitting procedure is better suited for comparison with real data, as it more closely mirrors black hole spectral analysis as done

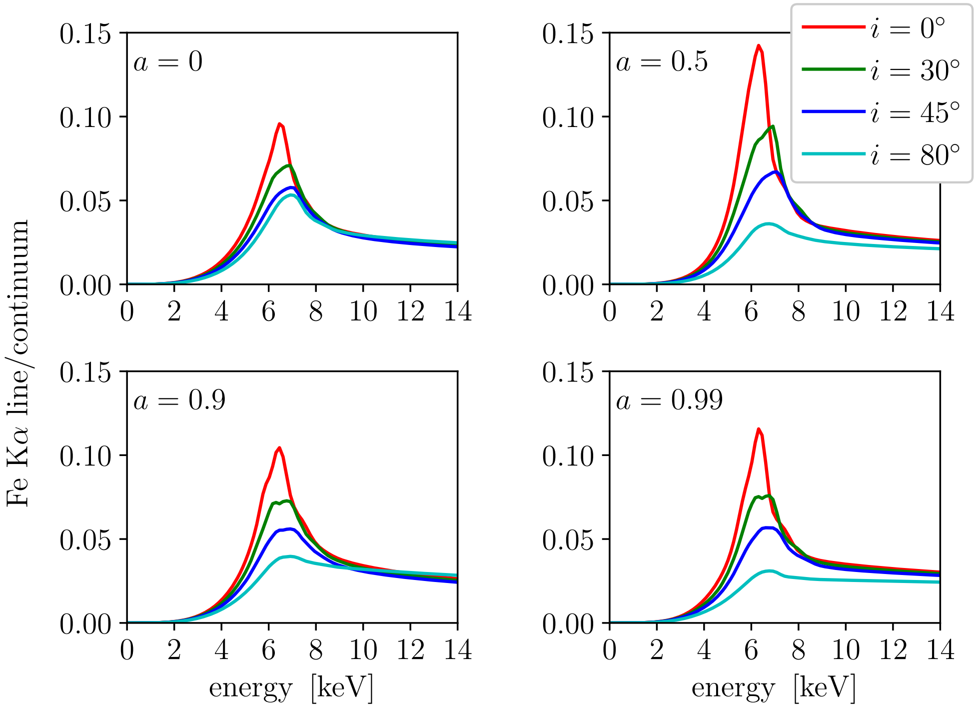

Figure 5.15: Photons whose origin is an Fe Kα transition, as a fraction of all continuum photons, once they have reached the distant observer; for several sample viewing angles, for each of the four spins considered.

in practice. Below we analyze the predicted Fe Kα emission with both methods.

Figures 5.15 shows the “true” Fe Kα emission, as seen by the distant observer at several sample inclination angles, divided by the underlying (“true”) continuum. At first glance, the Kα line profiles do not look all that dissimilar—except for the height of their peaks—for the different spins. In particular, there is not a substantial increase in the red wing (lower energy) line flux as the spin increases, as one might expect from the usual phenomenological models (Reynolds and Nowak, 2003). A closer look, however, reveals that the structure of the line profile near its peak changes with spin: as the spin increases, the “notch” near the line core becomes more pronounced. This is particularly noticeable for the $i = 30°$ profiles. This is due both to changes in ionization state (Fe Kα photons range from 6.41 keV to 6.97 keV, depending on ionization state), and to increased relativistic beaming as the emitting material orbits at smaller radii with increased spin (discussed further below).

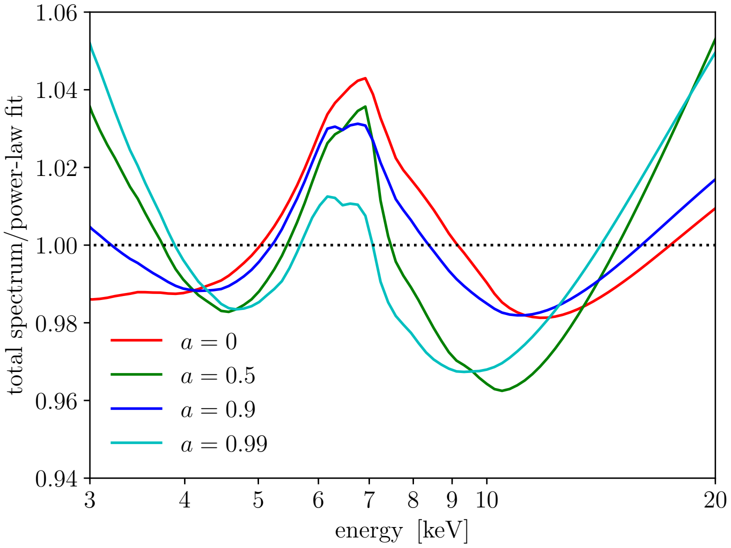

Figure 5.16: The predicted spectrum divided by a power-law fit to the range shown, at $i = 30°$, for each of the four spins. Note that the x-axis is logarithmic—as is the custom for showing real data in this way—as opposed to the linear scales of Figure 5.15.

The difference in the structure of the line core as a function of spin is more apparent in Figure 5.16, which shows the total spectrum divided by a power-law fit to the range shown for each of the four spin cases. In this view, the peak contrast of the line relative to the continuum appears to decline sharply with increasing spin: this effect is due to the increasingly poor fit of a single power-law to the underlying continuum—compare to the "true" continuum-divided plots of Figure 5.15. Interestingly, the width of the line feature, and the depth of the troughs on either side, does not appear to trend consistently with spin: the $a = 0$ and $a = 0.9$ profiles appear more similar in this regard, as do $a = 0.5$ and $a = 0.99$. This is another consequence of the poor fit: from Figure 5.12, we see that the $a = 0$ and $a = 0.5$ continua are straighter (i.e., more pure power-law) in the immediate vicinity of the Fe Kα emission feature than are the other two cases.

The equivalent width of the Fe Kα emission line, measured from 4–7 keV, is shown as a function of viewing angle and for each spin in Figure 5.17. While the peak contrast of the Kα feature as shown in Figure 5.16 decreases with increasing spin, the equivalent width of the feature generally increases—though, again, not in a monotonic fashion. The equivalent

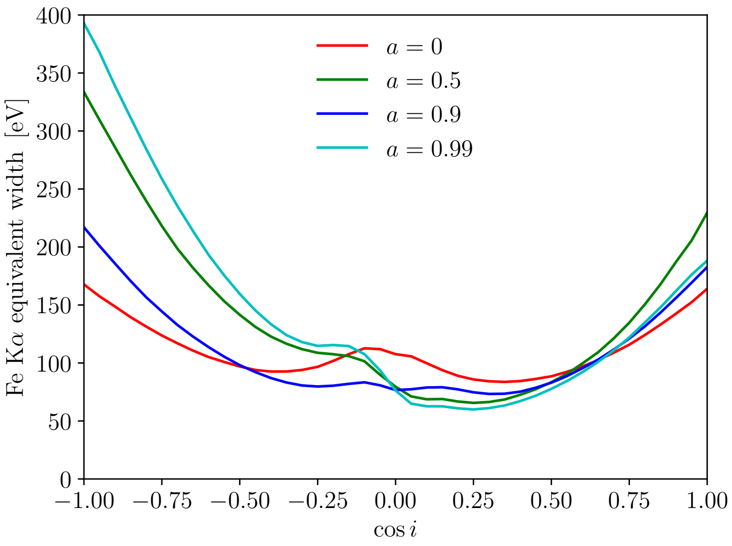

Figure 5.17: The equivalent width of the Fe Kα feature, measured over 4–7 keV, as a function of viewing angle, for each of the four spins.

width over a range from $\varepsilon_{\rm min}$ to $\varepsilon_{\rm max}$ is defined as the ratio of the line flux to the continuum flux integrated over the band, i.e.,

$$\mathrm{EW} = \int_{\varepsilon_{\rm min}}^{\varepsilon_{\rm max}} \frac{F_{\rm line}}{F_{\rm continuum}} d\varepsilon. \tag{5.1}$$

In other words, it is the integral under (a part of) the curves shown in Figure 5.16. It is also readily apparent from Figure 5.17 that there is significant asymmetry between the upper and lower disk surfaces—observers on either side would see lines of very different strength from the same object, especially for the $a = 0.5$ and $a = 0.99$ cases.

Figure 5.18 shows the Fe Kα surface brightness (emission from the disk surface), averaged over azimuth and both disk surfaces, as a function of the radial coordinate. The vertical dashed lines indicate the radius of the ISCO for each spin. The peak moves inward with increasing spin, as one might expect, though it is always one-to-several M exterior to the ISCO, consistent with the results shown in Chapters 2 and 3 for the $a = 0$, $\dot{m} = 0.01$ case computed using the target-temperature cooling function in the corona. In the $a = 0.9$ and $a = 0.99$ cases, however, there are large dips in the surface brightness, centered at $r = 8M$

and $r = 8$–$18M$, respectively. For the higher spin cases, the disk thins considerably, in part due to the choice of $\eta_{\rm NT}$ when scaling the density, which increases with increasing a and therefore lowers the density upon conversion to cgs units, moving the photosphere surfaces closer to the midplane; and in part due to the increased spatial and temporal variability of the accretion flow as discussed above. Figure 5.19 shows, for each spin, the Thomson scattering optical depth integrated from the positive z-axis to the midplane, as a function of radial and azimuthal coordinates. When the optical depth to the midplane is less than unity (shown in white in Figure 5.19), no photosphere surface exists, and PTRANSX cannot perform a reprocessing calculation. While for $a = 0$ and $a = 0.5$ there is a general trend of increasing disk thickness beyond the initial radius that reaches $\tau = 1$ (the "reflection edge"), the disk becomes "patchier" with increasing spin. For $a = 0.9$, there is an arc centered on $r = 8M$ where the photosphere surface is only barely present at most azimuths; for $a = 0.99$, the marginally extant disk region extends over roughly the range $r = 8$–$18M$; in both cases corresponding to the drop in Fe Kα surface brightness in these regions seen in Figure 5.18. For all four spin values, the reflection edge is located beyond the radius of the ISCO.

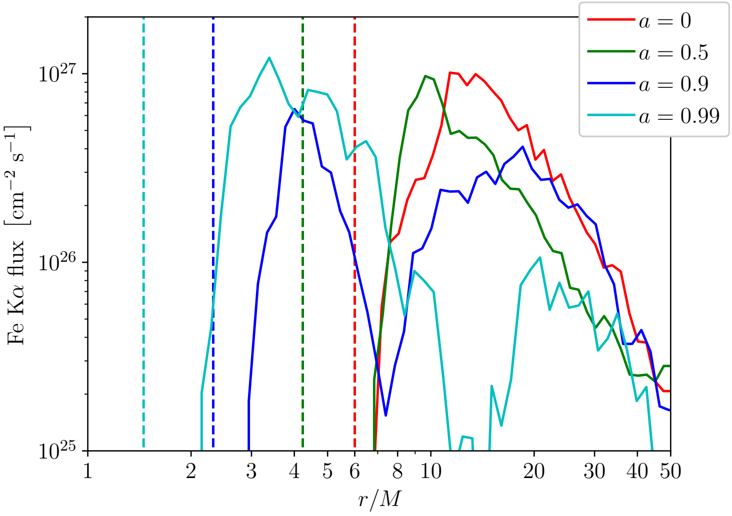

Figure 5.18: Fe Kα surface brightness, averaged over azimuth and both disk surfaces, for each of the four spins. The dashed lines indicate the radius of the ISCO for each spin, indicated by color.

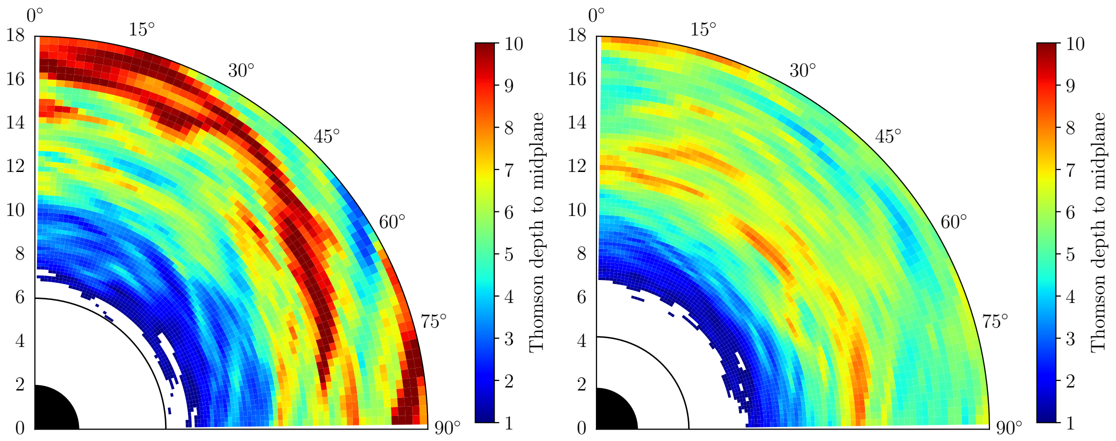

(a) $a = 0$.

(b) $a = 0.5$.

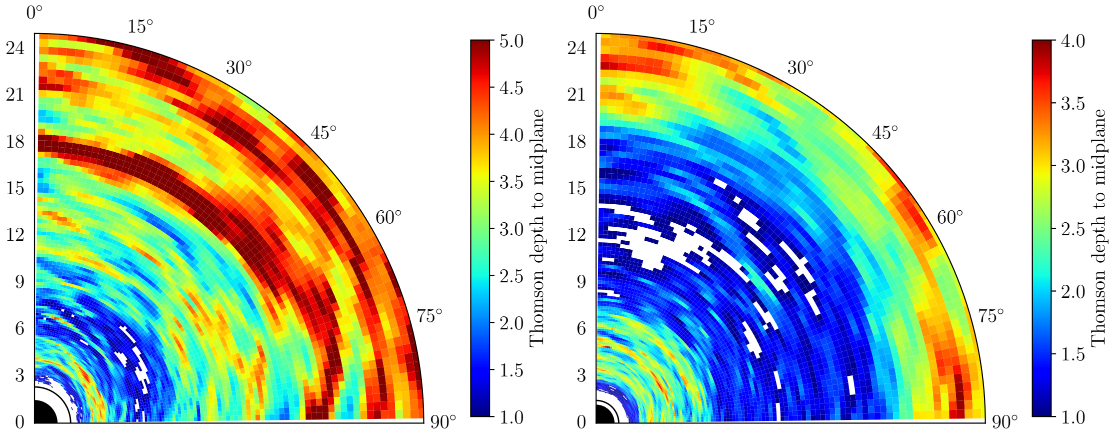

(c) $a = 0.9$.

(d) $a = 0.99$.

Figure 5.19: The Thomson depth, integrated to the midplane, for several spins. The masked regions (in white) do not reach unity, and therefore no photosphere exists. The solid black line indicates the radius of the ISCO. Note the differing scale among subplots.

5.4 Discussion

In the standard language of X-ray binary spectral classification (Remillard and McClintock, 2006), the spectra we predict for $a = 0.9$ and $a = 0.99$ are squarely in the "hard" (also referred to as "low/hard") state, characterized by a a photon index Γ in the range 1.4–2.1, and the majority of the luminosity due to the power-law (corona) component, rather than the thermal (disk) component of the spectrum; the $a = 0$ and $a = 0.5$ spectra do not fit as neatly—their Γ values are too soft to qualify for the "hard" state, but not quite so soft to qualify for the "steep power-law" (also known as "very high") state, for which the cutoff is $\Gamma > 2.4$; the presence of a power-law extending to high energies which carries the majority of the luminosity makes them a better fit for either the "hard" or "steep power-law" states, rather than the third category—the "thermal" (or "high/soft") state—in which the luminosity is dominated by the disk contribution. Regardless of exact classification, however, the very fact that our predicted spectra bear such resemblance to the real stellar-mass X-ray spectra upon which the classification scheme is based means that our method is indeed capable of simulating the relevant underlying physics and translating them into observable, comparison-ready spectra.

A driving force motivating the development of X-ray spectra modeling techniques is their application to the inference of black hole spin through comparison to real data. Because the radius of the ISCO is a one-to-one function of the black hole spin, and the ISCO radius has been with virtually no exceptions assumed exactly coincident with the inner edge of the accretion disk in all X-ray spectra modeling efforts to date, it has long been assumed in practice that whatever spectral feature or property one considers—photon index, Fe Kα profile or equivalent width, etc.—will vary in a monotonic fashion with spin, holding all else constant. In this context, it is rather surprising that, having varied *only* the spin, we do not find this to be the case. While the X-ray continuum calculated from the $a = 0$, 0.5, and 0.9 snapshots are easily distinguished by their increasing hardness, the $a = 0.9$ and $a = 0.99$ continua are not all that dissimilar except for the nearly five-fold difference in luminosity (which, of course, is much more difficult to measure than spectral shape, as it requires an independent distance measurement to compute). The Fe Kα lines are much less easily distinguished by spin: we find virtually no movement in the red wing; the shuffling of dominant emitting Fe ionization states is difficult to observe in practice due to limited detector energy resolution and integration times; and the equivalent width shows only a vague trend with spin, undermined by the near factor of two variation depending on which side of the disk is viewed.

Overall, then, we conclude from this analysis that continuum-fitting techniques are in general better suited to constraining spin in stellar-mass black holes than are methods which rely on fitting the Fe Kα line profile. We temper this conclusion, however, with one major caveat: a typical modern observation of a stellar-mass black hole—say, of Cyg X-1 using *NuSTAR* [there are many examples of exactly this observation, but a particularly thorough spectral analysis can be found in Walton et al. (2016)]—will have an integration time of $\sim 10^4$ seconds; Cyg X-1 is roughly $15 M_\odot$ by most estimates, so this is an integration time, in our units, of $\sim 10^8 M$. This is many, many times longer than we can feasibly run a simulation, and so even if we applied our post-processing to a large number of snapshots and averaged their results, we would still adequately sample only a small fraction of a typical integration time. It is possible that over $\sim 10^8 M$ of evolution, the time-averaged Fe Kα line profiles, or the $a \geq 0.9$ continua predictions, would become more distinct.

The timescales work in our favor for AGN. Consider the 210 ks *Suzaku* observation of the nearby Seyfert galaxy NGC 3783 reported in Brenneman et al. (2011). With a mass of $10^7 M_\odot$ measured via reverberation mapping (Onken and Peterson, 2002), this observation of NGC 3783 lasted only $\sim 5000 M$, a duration which could be feasibly sampled by a HARM3D simulation—even with the costlier IC corona cooling function—from which a representative series of snapshots could be taken for post-processing. Though the cooler, less-ionized accretion disks surrounding AGN will prove more challenging for PTRANSX's equilibrium-finding procedure (it is for this reason our initial test cases were the hotter, more thoroughly ionized stellar-mass black hole disks), and will almost certainly require more PTRANSX–PANDURATA passes due to the correspondingly higher disk absorptive opacity, the dramatic reduction in required simulation time—by far the more expensive input—make AGN the more attractive targets for real spin inference with our method.

We did not explore varying the nominal accretion rate $\dot{m}$. At higher accretion rates, the increased mass of the accretion flow will reduce the patchiness of the disk surface seen in Figure 5.19, perhaps providing greater distinction among the Fe Kα line profiles predicted for different spins, as there will be a more unbroken trend of increased emission at smaller radii. In addition, at higher accretion rates a greater share of the total cooling budget will be due to the thermal disk component—as we saw in Chapter 3, the photon index tends to increase with increasing accretion as the thermal component increases relative to the power-law component. It would be worthwhile to repeat such a survey with our now more physical corona cooling function.

Finally, while the choice of $\eta_{\rm NT}$ for the nominal radiative efficiency eases the comparison between our results and analytic accretion disk theory, a "bootstrapped" radiative efficiency—calculated from the simulation plus post-processing itself—would better facilitate comparison with observations. If the value for η used for the actual expression for $\mathcal{L}_{\rm code}$ (equation 4.26) as implemented in HARM3D is close to the value found by HARM3D plus post-processing, then the value for $\dot{m}$ inferred through eventual fitting of these model spectra to real data will better indicate the actual luminosity (in Eddington units) of the X-ray source in question.

References

Noble, S. C., J. H. Krolik, J. D. Schnittman, and J. F. Hawley (2011). "Radiative Efficiency and Thermal Spectrum of Accretion onto Schwarzschild Black Holes". In: *ApJ* 743, 115, p. 115. DOI: `10.1088/0004-637X/743/2/115`. arXiv: `1105.2825 [astro-ph.HE]`.

Novikov, I. D. and K. S. Thorne (1973). "Astrophysics of black holes." In: *Black Holes (Les Astres Occlus)*. Ed. by C. Dewitt and B. S. Dewitt, pp. 343–450.

Reynolds, C. S. and M. A. Nowak (2003). "Fluorescent iron lines as a probe of astrophysical black hole systems". In: *Phys. Rep.* 377, pp. 389–466. DOI: `10.1016/S0370-1573(02)00584-7`. eprint: `astro-ph/0212065`.

Remillard, R. A. and J. E. McClintock (2006). "X-Ray Properties of Black-Hole Binaries". In: *ARA&A* 44, pp. 49–92. DOI: `10.1146/annurev.astro.44.051905.092532`. eprint: `astro-ph/0606352`.

Walton, D. J., J. A. Tomsick, K. K. Madsen, V. Grinberg, D. Barret, S. E. Boggs, F. E. Christensen, M. Clavel, W. W. Craig, A. C. Fabian, F. Fuerst, C. J. Hailey, F. A. Harrison, J. M. Miller, M. L. Parker, F. Rahoui, D. Stern, L. Tao, J. Wilms, and W. Zhang (2016). "The Soft State of Cygnus X-1 Observed with NuSTAR: A Variable Corona and a Stable Inner Disk". In: *ApJ* 826, 87, p. 87. DOI: `10.3847/0004-637X/826/1/87`. arXiv: `1605.03966 [astro-ph.HE]`.

Brenneman, L. W., C. S. Reynolds, M. A. Nowak, R. C. Reis, M. Trippe, A. C. Fabian, K. Iwasawa, J. C. Lee, J. M. Miller, R. F. Mushotzky, K. Nand ra, and M. Volonteri (2011). "The Spin of the Supermassive Black Hole in NGC 3783". In: *ApJ* 736.2, 103, p. 103. DOI: `10.1088/0004-637X/736/2/103`. arXiv: `1104.1172 [astro-ph.HE]`.

Onken, C. A. and B. M. Peterson (2002). "The Mass of the Central Black Hole in the Seyfert Galaxy NGC 3783". In: *ApJ* 572, pp. 746–752. DOI: `10.1086/340351`. eprint: `astro-ph/0202382`.

Chapter 6

Ion-Electron Coupling

The IC corona cooling function developed in Chapter 4, with which we performed the spin survey in the previous chapter, was predicated on the assumption that $T_e = T_i$. This assumption has two parts: first, that the distribution of electron velocities and the distribution of ion velocities are thermal, i.e., they are well-described by a Maxwell-Jüttner distribution; and second, that through some mechanism the ion and electron populations are in thermal equilibrium with each other—either through an effective coupling mechanism allowing efficient and rapid energy exchange between the two populations, or because turbulent energy is dissipated as thermal energy shared equally between the ions and the electrons, or some combination thereof. In this final chapter, we explore the effects of relaxing the assumption that $T_e = T_i$ in a particular scenario:

1. The ion and electron populations are individually in thermal equilibrium locally, described by T_i and T_e at each point in the corona, respectively.
2. Turbulent energy is dissipated into the ions *only*.
3. Energy is exchanged between the ion and electron populations through Coulomb scattering.
4. T_e adjusts instantaneously so that the rate at which energy is *added* to the electron population—through either Coulomb collisions or Compton heating—is equal to the rate at which energy is *lost* due to inverse Compton cooling.

The problem, then, is to find T_e and T_i given the above assumptions.

6.1 Method

We begin with the relativistically correct ion-electron energy exchange rate derived in Stepney (1983) and Stepney and Guilbert (1983):

$$\begin{aligned}\frac{d}{dt}u_e \text{ (Coulomb heating)} &= \frac{3}{2}\frac{m_e}{m_i}\sigma_T c \ln \Lambda n_e n_i \left(kT_i - kT_e\right) \qquad (6.1)\\ &\times \left\{\frac{1}{K_2(1/\Theta_e)K_2(1/\Theta_i)}\left[\frac{2(\Theta_e+\Theta_i)^2+1}{\Theta_e+\Theta_i}K_1\left(\frac{\Theta_e+\Theta_i}{\Theta_e\Theta_i}\right)+2K_0\left(\frac{\Theta_e+\Theta_i}{\Theta_e\Theta_i}\right)\right]\right\}\\ &= \frac{3}{2}\frac{m_e}{m_i}\sigma_T c \ln \Lambda n_e n_i \left(kT_i - kT_e\right) f(\Theta_e, \Theta_i),\end{aligned}$$

where u_e is the internal energy per unit volume of the electron population, $\ln\Lambda$ is the Coulomb logarithm (the logarithm of the ratio of the maximum to minimum impact parameters; $\ln\Lambda \sim 20$), Θ_i is the dimensionless ion temperature, equal to $kT_i/m_i c^2$, and K_n is the n^{th} order modified Bessel function of the second kind. The term in braces—a complicated and typically difficult to evaluate collection of Bessel functions—constitutes $f(\Theta_e, \Theta_i)$.

The standard expression for Compton heating in the non-relativistic limit is

$$\frac{d}{dt}u_e \text{ (Compton heating)} = \frac{\sigma_T}{m_e c}n_e\int_0^\infty \varepsilon u_{\text{rad},\varepsilon} d\varepsilon = \frac{\sigma_T}{m_e c}n_e u_{\text{rad}}\langle\varepsilon\rangle; \qquad (6.2)$$

$\langle\varepsilon\rangle = 4kT_C$ (see equation 4.14). Finally, electrons give up their energy to photons via Inverse Compton scattering:

$$\frac{d}{dt}u_e \text{ (Compton cooling)} = -\frac{4\sigma_T c\chi}{m_i}\rho u_{\text{rad}}\Theta_e(1+4\Theta_e). \qquad (6.3)$$

The equilibrium T_e is that for which these processes balance, i.e., $du_e/dt = 0$. Summing equations 6.1, 6.2, and 6.3, we have:

$$\frac{3}{2}\frac{m_e}{m_i}\sigma_T c \ln\Lambda n_e n_i \left(kT_i - kT_e\right) f(\Theta_e, \Theta_i) + \frac{\sigma_T}{m_e c} n_e u_{\mathrm{rad}} \langle\varepsilon\rangle \tag{6.4}$$

$$- \frac{4\sigma_T c\chi}{m_i}\rho u_{\mathrm{rad}}\Theta_e(1 + 4\Theta_e) = 0.$$

With the identification that $n_e = \chi n_i$ and $n_i = \rho/m_i$, and some algebraic manipulation, we rewrite the above as:

$$\frac{3}{2}\frac{m_e}{m_i}\ln\Lambda\left(\Theta_i - \frac{m_e}{m_i}\Theta_e\right) f(\Theta_e, \Theta_i) + \frac{u_{\mathrm{rad}}}{\rho c^2}\frac{\langle\varepsilon\rangle}{m_e c^2} - 4\frac{u_{\mathrm{rad}}}{\rho c^2}\Theta_e(1 + 4\Theta_e) = 0. \tag{6.5}$$

We rearrange the ideal gas law, equation 4.7, to solve for Θ_i,

$$\Theta_i = (c_P/c_V - 1)\frac{u}{\rho c^2} - \chi\frac{m_e}{m_i}\Theta_e. \tag{6.6}$$

Substituting the above into equation 6.5:

$$\frac{3}{2}\frac{m_e}{m_i}\ln\Lambda\left[(c_P/c_V - 1)\frac{u}{\rho c^2} - \frac{m_e}{m_i}(1+\chi)\Theta_e\right] f\left(\Theta_e, (c_P/c_V - 1)\frac{u}{\rho c^2} - \chi\frac{m_e}{m_i}\Theta_e\right) \tag{6.7}$$

$$+ \frac{u_{\mathrm{rad}}}{\rho c^2}\frac{\langle\varepsilon\rangle}{m_e c^2} - 4\frac{u_{\mathrm{rad}}}{\rho c^2}\Theta_e(1 + 4\Theta_e) = 0.$$

We define three dimensionless quantities,

$$A \equiv \frac{u}{\rho c^2},\ B \equiv \frac{u_{\mathrm{rad}}}{\rho c^2},\ \text{and}\ C \equiv \frac{\langle\varepsilon\rangle}{m_e c^2}, \tag{6.8}$$

which we substitute into equation 6.7:

$$\frac{3}{2}\frac{m_e}{m_i}\ln\Lambda\left[(c_P/c_V - 1)A - \frac{m_e}{m_i}(1+\chi)\Theta_e\right] f\left(\Theta_e, (c_P/c_V - 1)A - \chi\frac{m_e}{m_i}\Theta_e\right) \tag{6.9}$$

$$+BC - 4B\Theta_e(1 + 4\Theta_e) = 0.$$

Thus, we arrive at an equation for Θ_e, in terms of only dimensionless quantities, which depends on three parameters which can be read off directly from already-computed values in HARM3D. Equation 6.9 is not amenable to real-time solution in each coronal cell each timestep; rather, we tabulate its solution on a grid covering all possible, reasonable values of A, B, and C, and use trilinear interpolation to calculate the appropriate equilibrium value of Θ_e from said lookup-table in the course of the simulation run. From Θ_e we calculate Θ_i from equation 6.6 and $\mathcal{L}_{\mathrm{IC}}$ from equation 4.6.

6.2 Simulation Results

We apply the cooling function as described above to the same $a = 0$ starter simulation used in Chapter 4, and evolve for $100M$. Figures 6.1 and 6.2 compare the cooling rate and electron temperature between the $T_e = T_i$ simulation described in Chapters 4 and 5 and the $T_e \neq T_i$ method described here. The cooling rate is lower in the latter, and significant cooling is confined to a region within 30° of the midplane, as opposed to more extended cooling in the $T_e = T_i$ scenario. As in previous chapters, these trends are easier to discern as ϕ-integrated, r- or θ-integrated distributions, Figures 6.3 and 6.4 respectively. From these figures we see that while the IC corona cooling rate is everywhere depressed for the $T_e \neq T_i$ simulation relative to the $T_e = T_i$ case, this depression is less pronounced nearer to the midplane and at larger radii. The share of total cooling in the corona for the $T_e \neq T_i$ simulation is 48%, compared to 64% for the $T_e = T_i$ simulation.

Likewise, T_e as found by HARM3D is both much lower in the $T_e \neq T_i$ scenario, but different in its spatial variation: whereas for the $T_e = T_i$ simulation, T_e generally increases away from the disk, for the $T_e \neq T_i$ simulation it *decreases*, nearly monotonically, with distance from the disk, achieving its hottest values in a thin layer just outside the disk surface.

Figure 6.9 compares the distribution-in-temperature of the IC cooling rate between both scenarios. As is evident enough from Figure 6.2, the $T_e \neq T_i$ cooling occurs in gas that is both cooler, and with a smaller overall range in T_e, as compared to the $T_e = T_i$ simulation.

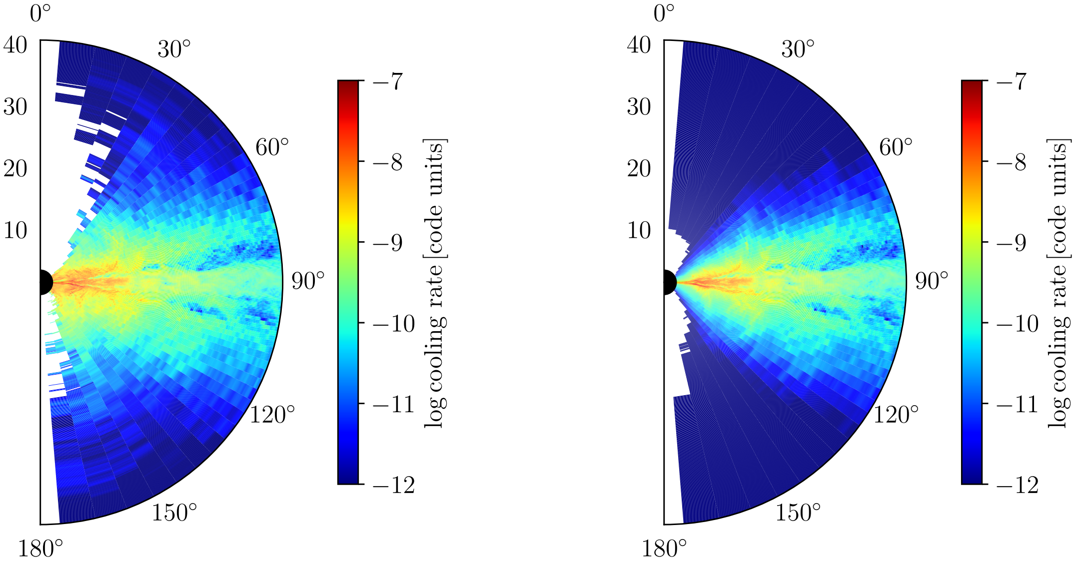

(a) $T_e = T_i$

(b) $T_e \neq T_i$

Figure 6.1: Snapshots of the ϕ-averaged cooling rate, in code units, for the $a = 0$ simulations at $t = +100M$. The uncooled material is masked (in white). Left panel: T_e and T_i required to be equal. Right panel: T_e and T_i determined as described in this chapter.

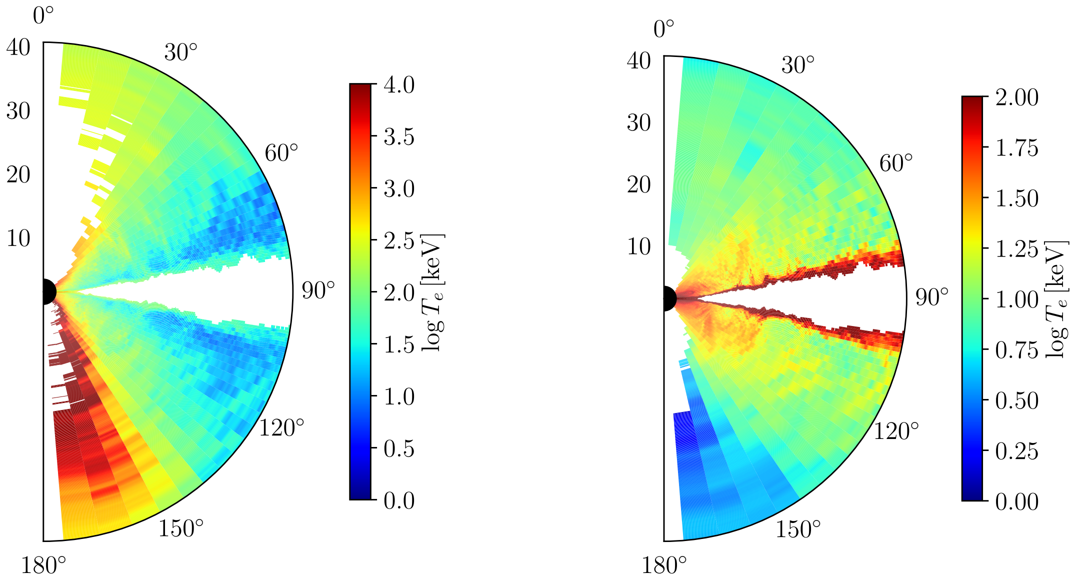

(a) $T_e = T_i$

(b) $T_e \neq T_i$

Figure 6.2: Comparison of the ϕ-averaged T_e, as found by HARM3D, for the $a = 0$ simulations at $t = +100M$. The uncooled material is masked (in white). Left panel: T_e and T_i required to be equal. Right panel: T_e and T_i determined as described in this chapter. Note a drastic difference in scale between the two subplots.

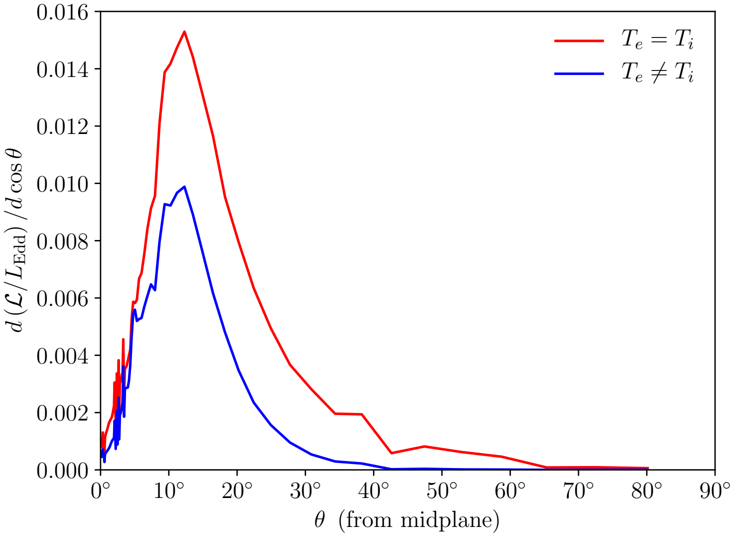

Figure 6.3: The distribution of coronal cooling (integrated over azimuth and radius) as a function of polar angle measured from the midplane, for the $a = 0$, $\dot{m} = 0.01$ simulations at $t = +100M$, for $T_e = T_i$ and $T_e \neq T_i$ conditions.

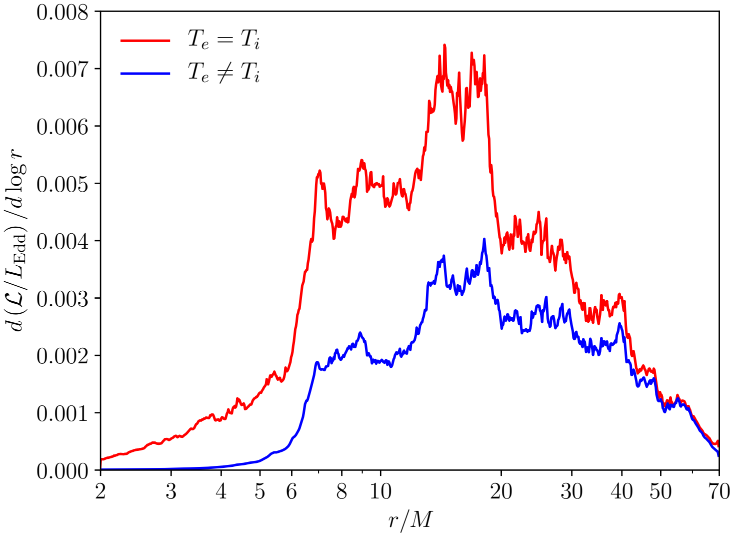

Figure 6.4: The distribution of coronal cooling (integrated over polar angle and azimuth) as a function of radius, for the $a = 0$, $\dot{m} = 0.01$ simulations at $t = +100M$, for $T_e = T_i$ and $T_e \neq T_i$ conditions.

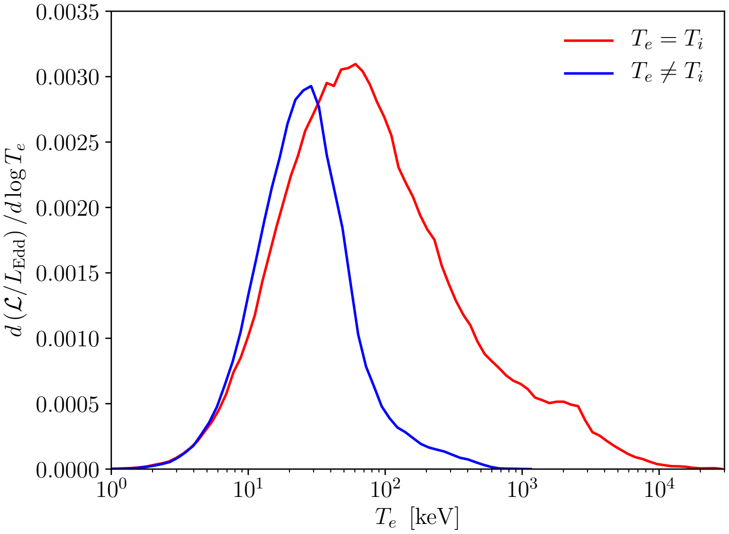

Figure 6.5: The distribution of IC power as a function of electron temperature in the corona, for the $a = 0$ simulations at $t = +100M$, for $T_e = T_i$ and $T_e \neq T_i$ conditions.

The explanation for both the generally depressed equilibrium T_e and the radically different spatial variation lies in the difference in efficiency between ion-electron energy transfer and electron-photon energy transfer. Ion-electron energy transfer, i.e., Coulomb heating, is proportional to ρ^2 (equation 6.1), and therefore decreases in efficiency as the density thins out by several orders of magnitude from the midplane to the poles—see Figure 6.6. Electron-photon energy transfer, i.e., net Compton cooling, on the other hand, is proportional to $\rho u_{\rm rad}$, and because the corona is by definition optically thin, $u_{\rm rad}$ is, by comparison to the density, constant throughout the corona—see Figure 6.7. Therefore electron-photon energy transfer remains efficient relative to ion-electron energy transfer, even far from the disk: the result is that electrons are able to quickly transfer whatever energy they receive from ions to photons, keeping their temperature low, while the ions remain hot. In Figure 6.8, we show the ratio T_e/T_i: though $T_e/T_i \sim 0.1$–1 near the disk surface, this ratio rapidly drops off further into the corona.

In Figure 6.9, we compare the HARM3D T_e values to the PANDURATA+PTRANSX values found by post-processing this simulation snapshot. For the bulk of the coronal volume,

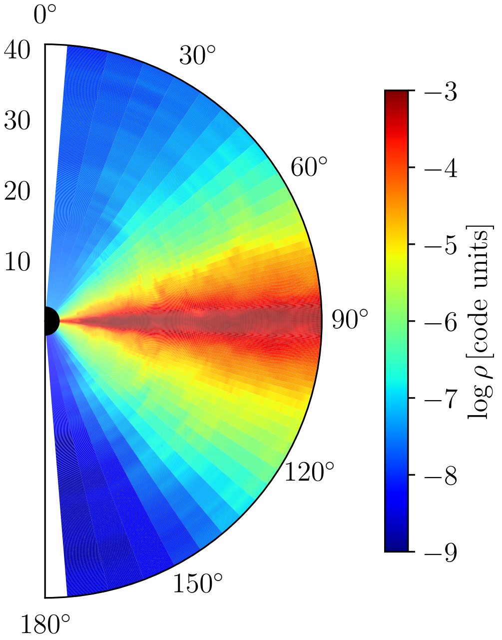

Figure 6.6: The ϕ-averaged density, in code units, for the $a = 0$, $\dot{m} = 0.01$ simulation, $T_e \neq T_i$, at $t = +100M$.

PANDURATA finds T_e values which are approximately twice as high as HARM3D's values. This disagreement is due to HARM3D's poor estimation of the Compton temperature, T_C. In general, the IC cooling rate in the non-relativistic regime is proportional to $(T_e - T_C)u_{\rm rad}$. When $T_e \gg T_C$, as is the case when $T_e = T_i$, the proper estimation of T_C is not of much importance. In this case, however, $T_e \sim$ 20–30 keV, while $T_C \sim 10$ keV. If $u_{\rm rad}$ as determined by HARM3D is sufficiently accurate to achieve good agreement with PANDURATA in the $T_e = T_i$ simulations, then the higher equilibrium T_e found by PANDURATA for these simulations must indicate that HARM3D is consistently *underestimating* T_C, by roughy a factor of 2. Calculating T_C in HARM3D requires calculating the mean photon energy—ignoring special and General Relativistic effects like Doppler boosting and gravitational redshift as well as IC scattering has, apparently, a greater effect on the estimation of the first moment of the spectral energy distribution than it does on the estimation of simply the bolometric photon energy density.

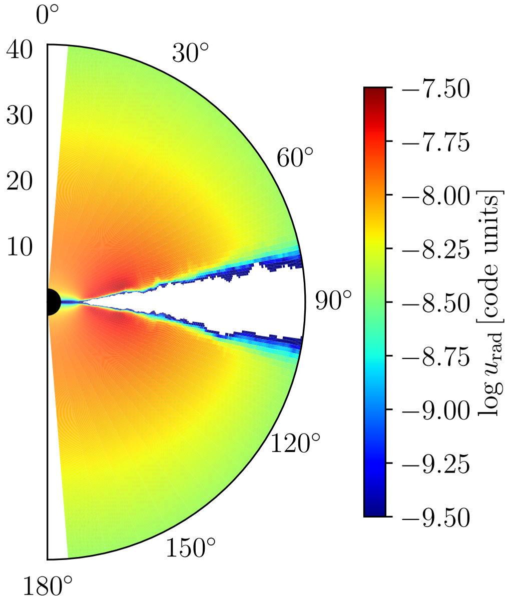

Figure 6.7: The ϕ-averaged radiation energy density, in code units, for the $a = 0$, $\dot{m} = 0.01$ simulation, $T_e \neq T_i$, at $t = +100M$.

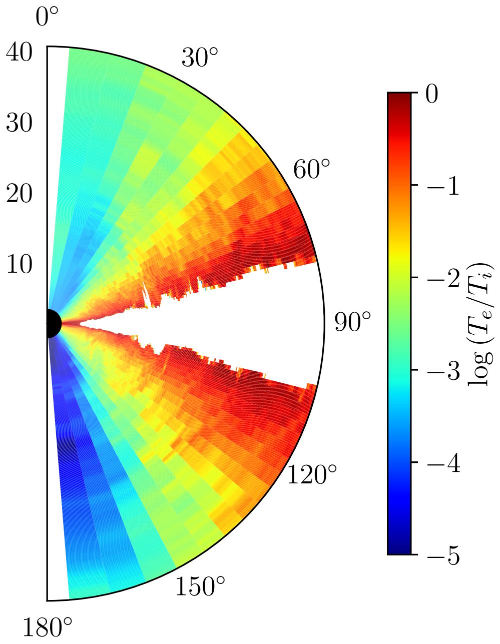

Figure 6.8: The ϕ-averaged T_e/T_i ratio for the $a = 0$, $\dot{m} = 0.01$ simulation, $T_e \neq T_i$, at $t = +100M$.

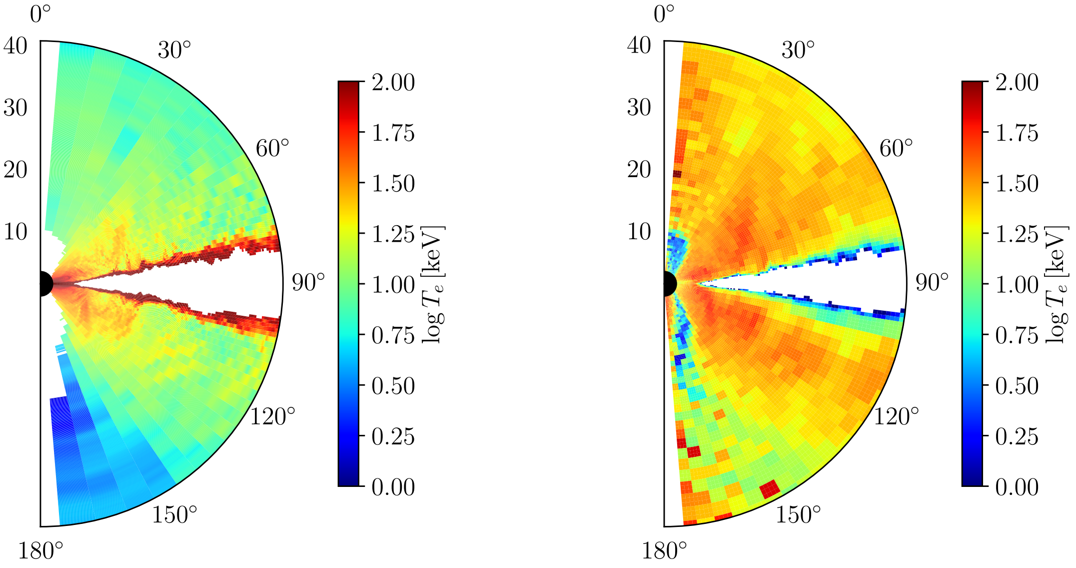

(a) HARM3D (b) PANDURATA+PTRANSX

Figure 6.9: Comparison of the ϕ-averaged T_e, as found by HARM3D (left, masking uncooled regions) and PANDURATA+PTRANSX (right), for the post-processed snapshot of the $a = 0$ simulation at $t = +100M$, for which $T_e \neq T_i$.

6.3 Post-Processing

We can apply PANDURATA+PTRANSX to the $T_e \neq T_i$ simulation to predict the resulting spectra. Figure 6.10 shows the spectral luminosity for each case: not surprisingly, the $T_e \neq T_i$ spectrum is softer, with $\Gamma = 2.6$ compared to $\Gamma = 2.3$ for the $T_e = T_i$ spectrum; the power-law also falls off both more sharply and at a lower energy than does its counterpart. The $T_e \neq T_i$ predicted total luminosity is 2.0% L_{Edd}, lower than the the predicted 2.5% L_{Edd} for $T_e = T_i$. The Fe Kα line profiles shown in Figure 6.11, are, however, remarkably similar, with the $T_e \neq T_i$ lines actually slightly stronger. This is not too surprising either, though: the K-edge transition is the most absorptive in the range 7–30 keV (recall Figures 3.6 and 3.7), and the $T_e \neq T_i$ corona does a larger share of its cooling through electrons within this temperature range than does the $T_e = T_i$ corona.

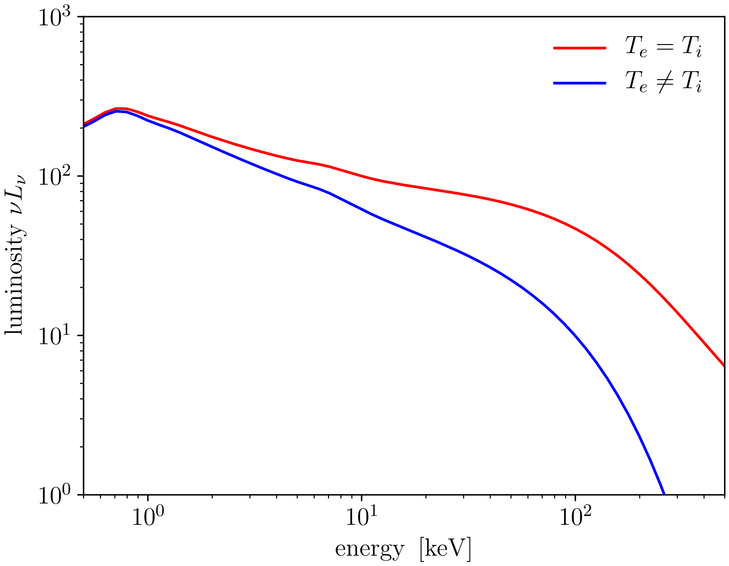

Figure 6.10: The spectral luminosity for the post-processed snapshots of the $a = 0$ simulations at $t = +100M$.

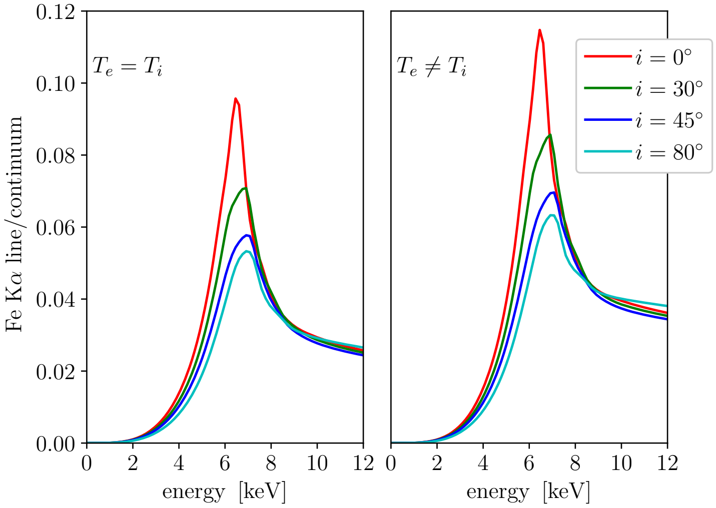

Figure 6.11: Photons whose origin is an Fe Kα transition, as a fraction of all continuum photons, once they have reached the distant observer; for several sample viewing angles, for the two $a = 0$ simulations.

6.4 Discussion

We have compared the two most limiting cases—excluding the possibility of non-thermal electron populations—of coupling between the ion and electron populations. The actual physical reality is likely somewhere in between. As we have shown, the choice makes a significant difference for the predicted X-ray continuum shape and the predicted luminosity, though not a significant difference for the Fe Kα line profile or strength. Comparing to the general trends of stellar-mass X-ray spectra (Remillard and McClintock, 2006), the harder spectra predicted for $T_e = T_i$ for a roughly similar ratio of thermal to power-law component flux (that is, neither are in the "thermal" state) lends more observational support to the stronger coupling hypothesis. Also, because we observe hard spectra from AGN as well, for which the coronal density is much lower (recall $\rho \propto M^{-1}$, equation 4.24), and ion-electron energy exchange through Coulomb collisions only is proportional to ρ^2, we would expect this bare minimum coupling to fail to predict sufficiently hard spectra at AGN scales—though we have yet to explore this scale quantitatively with our spectral prediction apparatus. Using observational data to more precisely discriminate between $T_e = T_i$ and $T_e \neq T_i$ might be difficult due to degeneracies with other physical parameters: for example, both stronger ion-electron coupling and increased spin result in harder spectra, and both weaker coupling and higher accretion rate result in softer specta. However, with a collection of simulations and predicted spectra fully spanning the possible parameter space—mass, spin, and accretion rate—it will be possible to characterize any such degeneracy and find more support for one extreme over the other, especially for those objects with independent distance measurements which allow for the accurate estimation of the X-ray luminosity.

References

Stepney, S. (1983). “Two-body relaxation in relativistic thermal plasmas”. In: *MNRAS* 202, pp. 467–481. DOI: `10.1093/mnras/202.2.467`.

Stepney, S. and P. W. Guilbert (1983). “Numerical fits to important rates in high temperature astrophysical plasmas.” In: *MNRAS* 204, pp. 1269–1277. DOI: `10.1093/mnras/204.4.1269`.

Remillard, R. A. and J. E. McClintock (2006). “X-Ray Properties of Black-Hole Binaries”. In: *ARA&A* 44, pp. 49–92. DOI: `10.1146/annurev.astro.44.051905.092532`. eprint: `astro-ph/0606352`.

Chapter 7

Conclusion

The most important result of the work so far is that we have developed a first-principles approach to the prediction of X-ray spectra from simulations of accreting black holes. The spectra so generated are comparable to the real X-ray observations of stellar-mass black hole systems. Critically, we *do not* require supersolar Fe abundances, or unreasonably dense disks, in order to achieve strong Fe Kα emission lines. We believe this contrast between our method and the usual techniques is due primarily to our more realistic treatment of the corona. As it stands now, our post-processing machinery PANDURATA+PTRANSX is relatively cheap to run (compared to 3D GRMHD simulations), and—from a software development point of view—can be used as a "black box," translating simulation data into spectra without any human intervention (except for checking, of course, that the results always make physical sense!). With its long development cycle behind us, we imagine applying our powerful new tool to a host of problems. Some of these are:

1. Applying the IC corona cooling function plus PANDURATA+PTRANSX to a broader time-sampling of snapshots from the HARM3D simulations. This will give us not only a sense of the time-variability of the luminosity and individual spectral features, but also—as discussed in Chapter 5—will also yield results more directly comparable to the time-integrated spectra which are actually observed.
2. Perform an exploration of the parameter space, chiefly over *both* the accretion rate $\dot{m}$

and the dimensionless spin a. We reported the effects of changing only one of these at a time in Chapters 3 and 5, respectively, but a two-dimensional parameter study will allow us to comment on how degenerate one might be with the other in real spectral fits. Recall, for example, that both *increasing* $\dot{m}$ and *decreasing* a lead to softer spectra: might these effects be distinguished by, perhaps, the shape and strength of the Fe Kα line, the energy of the thermal peak, or the Compton reflection hump?

3. Extend to AGN. In principle, the only required change to PANDURATA+PTRANSX is to set a different value for M in a parameter file. In practice, however, the cooler AGN disks are more absorptive, and their lower overall degree of ionization means that more atomic species are not fully-stripped. This slows down the convergence of both the internal PTRANSX photoionization equilibrium calculation, and the global cycling between PANDURATA and PTRANSX. Nevertheless, this should be simply a question of spending additional CPU-hours and perhaps some optimization. As we discussed in Chapter 5, the difference in time scales between stellar-mass and super-massive black holes make AGN a more favorable first target for our ultimate goal, fitting a real spectrum.

4. Fit a real spectrum. Achieving a good fit to real data would be the greatest test of our method—and an excellent test for the theory of MHD accretion flows more broadly. This requires spanning the relevant parameter space: mass, spin, accretion rate, Fe abundance, and viewer inclination angle. The most efficient way to do so is to take a well-studied target, like MCG-6-30-15, and use the best estimates in the literature to place starting bounds and initial guesses, and refine from there. We intend to release the results of a broader sampling as an XSPEC model to be used by observers working in the field, as a more physically-founded competitor to those models in wide use at present (discussed in Chapters 1–3).

We clearly have much work to do. But the results so far are encouraging, and compel us to continue to attempt to understand black hole observations from the standpoint of genuine physical principles.

Brooks E. Kinch

Department of Physics and Astronomy,
Johns Hopkins University,
Baltimore, MD 21218

kinch@jhu.edu
US Citizen
Born: December 30, 1991 in New Jersey

Education

Johns Hopkins University, PhD, Astrophysics, expected December 2019.
Johns Hopkins University, MA, Physics and Astronomy, May 2015.
Rensselaer Polytechnic Institute, BS, Physics and Economics, *summa cum laude*, May 2013.

Publications

Kinch, B. E., Schnittman, J. D., Noble, S. C., Kallman, T. R., and Krolik, J. H., "X-ray Spectra from Simulations of Spinning Black Holes", in preparation.

Kinch, B. E., Schnittman, J. D., Kallman, T. R., and Krolik, J. H., "Predicting the X-Ray Spectra of Stellar-mass Black Holes from Simulations", *Astrophysical Journal*, 873, 71 (2019). arXiv:1810.13099. Citations: 4 (via SAO/NASA ADS)

Kinch, B. E., Schnittman, J. D., Kallman, T. R., and Krolik, J. H., "Fe Kα Profiles from Simulations of Accreting Black Holes", *Astrophysical Journal*, 826, 52 (2016). arXiv:1604.01126. Citations: 8 (via SAO/NASA ADS).

Conferences and Seminars

Accretion in Stellar Systems, *Chandra* X-ray Center, Harvard-Smithsonian Center for Astrophysics. August 2018. Contributed talk.

The Power of X-ray Spectroscopy, Nicolaus Copernicus Astronomical Center of the Polish Academy of Sciences. September 2017. Contributed talk.

Goddard-JHU Interaction Day, Johns Hopkins University. October 2014. Contributed talk.

221st Meeting of the American Astronomical Society, Long Beach, CA. January 2013. Poster.

Experience

Research Assistantship 9/14-ongoing
Graduate research assistantship with Professor Julian Krolik at the Department of Physics and Astronomy at Johns Hopkins University. Ongoing thesis work to use data from general relativistic magnetohydrodynamic simulations of accreting black hole systems to predict their X-ray spectra.

Assistant Researcher at NASA GSFC 5/14-8/14
Part of ongoing research at the Department of Physics and Astronomy, Johns Hopkins University, described above.

SARA REU program 5/12-8/12
Analyzed the time-varying brightness of cataclysmic variable stars with lightcurves from the Kepler spacecraft. Received training in photometry at the 0.9 meter SARA telescope at Kitt Peak, AZ.

Teaching Assistantships 9/11-5/12, 9/13-5/14
Undergraduate teaching assistant at Rensselaer Polytechnic Institute for Physics II. Graduate teaching assistant at Johns Hopkins University for Physics I and II, and their respective laboratory components.

Honors

Edward J. Holstein Memorial Award for Excellence in Economic Science. May 2013.
Janet Manning Memorial Scholarship. May 2010.